Advanced numerical and semi-analytical scattering matrix calculations for modern nano-optics

Vorgelegt von

Thomas Weiss

aus Amberg

Physikalisches Institut der Universität Stuttgart

2011

Contents

Contents

Abbreviations

Technical abbreviations:

FMM	Fourier modal method
FFT	fast Fourier transform
ASR	adaptive spatial resolution
S-matrix	scattering matrix
TE	transverse electric
TM	transverse magnetic
s	from German *senkrecht* = perpendicular
p	parallel
FP	Fabry-Perot
SEM	scanning electron microscopy

General definitions:

$\alpha, \beta, \gamma, \delta$	variable integers for components $1, 2, 3$ of three-dimensional vectors
m, n, p, q	variable integers or placeholders for integers
M, N	fixed positive integers
$\epsilon^{\alpha\beta\gamma}$	Levi-civita symbol, see equation (2.5)
$\delta^{\alpha\beta}, \delta_{\alpha\beta}, \delta^{\alpha}_{\beta}$	Kronecker delta
$\mathbf{A}$	three-dimensional vector
$\mathbf{e}^{\alpha}$	contravariant basis vectors
$\mathbf{e}_{\alpha}$	covariant basis vectors
A^{α}	contravariant vector components
A_{α}	covariant vector components
$\hat{A}, \mathcal{A}, \mathbb{A}$	operators

Physical quantities:

c	speed of light in vacuum
$\underline{\underline{\varepsilon}}, \underline{\underline{\mu}}$	permittivity and permeability tensors with components $\varepsilon^{\alpha\beta}$ and $\mu^{\alpha\beta}$, respectively
ε, μ	permittivity and permeability scalars
ϱ	charge term
ω	angular frequency
k_0	vacuum wave number $k_0 = \frac{\omega}{c}$
$\mathbf{k}, k_\alpha$	incident wave vector and its covariant components
$\mathbf{E}, E_\alpha$	electric field and its covariant components
$\mathbf{H}, H_\alpha$	magnetic field and its covariant components
$\mathbf{D}, D^\alpha$	electric displacement and its contravariant components
$\mathbf{B}, B^\alpha$	magnetic induction and its contravariant components
$\mathbf{j}, j^\alpha$	current vector and its contravariant components
$\mathbf{S}, S^\alpha$	Poynting vector and its contravariant components
$\mathbf{G}_{mn}, G_{\alpha m}$	lattice vector and components
$K_{\alpha m}$	$K_{\alpha m} = k_\alpha + G_{\alpha m}$

Coordinate systems:

$\mathbf{r}$	three-dimensional vector with spatial components
$x, y, z, \overline{x}^\alpha$	Cartesian coordinates
$\check{x}^\alpha$	coordinates of uniform skewed coordinate system
u, v, w, x^α	general non-uniform coordinates
$\grave{x}^\alpha$	dummy coordinates
$\partial_\alpha, \frac{\partial}{\partial x^\alpha}$	derivative with respect to x^α
$g_{\alpha\beta}, g$	metric components and their determinant, see equation (2.7)
$g^{\alpha\beta}$	conjugate metric components, see equation (2.10)
ζ	angle between y axis and x^2 axis
χ	angle between z axis and x^3 axis
ξ	angle between x axis and projection of x^3 axis on xy plane
θ	polar incidence angle as angle between incident wave vector and z axis
ϕ	azimuth incidence angle as angle between x axis and projection of incident wave vector on xy plane

Special quantities:

$F_{\alpha mn}$	Fourier coefficient of order mn for vector component F_α
$f_{mn,pq}$	matrix elements for inner product $\sum_{p,q} f_{mn,pq}\, g_{pq} = h_{mn}$ in Fourier space
$\hat{l}_\alpha^-$	Li operator, see equation (2.20)
$\hat{\varepsilon}, \hat{\mu}$	Fourier transform of permittivity and permeability tensors
$\tilde{\varepsilon}, \tilde{\mu}$	$\hat{l}_3^-(\hat{\varepsilon})$ and $\hat{l}_3^-(\hat{\mu})$, respectively
$\hat{\mathcal{N}}, \hat{\mathcal{L}}$	special operators, see equations (2.23) and (2.24)
$\mathcal{K}_\alpha$	derivative operator in direction α, see equation (2.25)
$\vec{\mathcal{E}}_\alpha, \vec{\mathcal{H}}_\alpha$	vectors composed of components $E_{\alpha mn}, H_{\alpha mn}$
$\vec{\mathcal{E}}_{||}, \vec{\mathcal{H}}_{||}, \vec{\mathcal{F}}_{||}$	reciprocal representation of lateral field components, see equations (2.22) and (2.26)
$\lambda_n, \lambda_n^\pm, \Lambda^\pm$	eigenvalues of equation (2.27) and eigenvalue matrix, with $+/-$ indicating the subsets of forward/backward propagating or decaying solutions in direction x^3
$\mathcal{E}_{||}^\pm, \mathcal{H}_{||}^\pm, \mathcal{F}_{||}$	eigenvector matrices and material matrix, see equation (2.29)
$K_{3mn}^\pm, \lambda_{mn}^\pm$	covariant third wave vector components of plane waves with order mn
K_{mn}^3	contravariant third wave vector component corresponding to K_{3mn}^+
$E_\alpha^{(\beta,m,n,\pm)}$	plane wave of polarization β and order mn
$e_{\alpha mn}^{\beta\pm}$	polarization state of plane wave with polarization β and order mn
$\vec{\mathbb{A}}_n^\pm$	vector of expansion coefficients for forward or backward propagation or decay in layer n
$\mathbb{S}_{NM}$	scattering matrix between layer M (top) and layer N (bottom)
$|O\rangle, |I\rangle$	output and input vector of scattering matrix
$\mathbb{P}_n(L)$	matrix for propagation over distance L in layer n
$\mathbb{T}_{n(n-1)}$	matrix describing boundary conditions at an interface between adjacent layers $n, n-1$

Abstract

The optical properties of nanostructures such as photonic crystals and meta-materials have drawn a lot of attention in recent years [1–9]. The numerical derivation of these properties, however, turned out to be quite complicated, especially in the case of metallo-dielectric structures with plasmonic resonances. Hence, advanced numerical methods as well as semi-analytical models are required. In this work, we will show that the scattering matrix formalism can provide both.

The scattering matrix approach is a very general concept in physics. In the case of periodic grating structures, the scattering matrix can be derived by the Fourier modal method [10]. For an accurate description of non-trivial planar geometries, we have extended the Fourier modal method by the concept of matched coordinates [11], in which we introduce a new coordinate system that contains the material interfaces as surfaces of constant coordinates. In combination with adaptive spatial resolution [12, 13], we can achieve a tremendously improved convergence behavior which allows us to calculate complex metallic shapes efficiently.

Using the scattering matrix, it is not only possible to obtain the optical properties for far field incidence, such as transmission, reflection, absorption, and near field distributions, but also to solve the emission from objects inside a structure and to calculate the optical resonances of a system. In this work, we provide an efficient method for the ab initio derivation of three-dimensional optical resonances from the scattering matrix [14].

Knowing the resonances in a single system, it is in addition possible to obtain approximated resonance positions for stacked systems using our method of the resonant mode coupling [15, 16]. The method allows describing both near field and far field regime for stacked two-layer systems, including the strong coupling to Fabry-Perot resonances. Thus, we can study the mutual coupling in such systems efficiently.

The work will provide the reader with a basic understanding of the scattering matrix formalism and the Fourier modal method. Furthermore, we will describe in detail our extensions to these methods and show their validity for several examples.

Zusammenfassung

Die optischen Eigenschaften von Nanostrukturen wie zum Beispiel photonischen Kristallen und Metamaterialien haben in letzter Zeit große Aufmerksamkeit erfahren [1–9]. Dabei hat sich die numerische Berechnung dieser Eigenschaften als relativ kompliziert erwiesen, besonders im Falle von metallodielektrischen Strukturen, welche plasmonische Resonanzen aufweisen. Deshalb sind sowohl fortschrittliche numerische Methoden als auch semianalytische Modelle wünschenswert. In dieser Arbeit zeigen wir, dass der Streumatrixformalismus beides bieten kann.

Der Streumatrixansatz ist in der Physik ein weitverbreitetes Konzept. Im Falle von periodischen Strukturen kann man die Streumatrix über die Fouriermodale Methode bestimmen [10]. Um komplexere ebene Geometrien exakt beschreiben zu können, haben wir die Fourier-modale Methode um das Konzept der angepassten Koordinaten erweitert [11], in welchem neue Koordinaten eingeführt werden, die die Grenzflächen zwischen verschiedenen Materialien als Flächen konstanter Koordinaten beinhalten. In Kombination mit der adaptiven Ortsauflösung [12, 13] konnten wir enorme Verbesserungen des Konvergenzverhaltens erzielen, so dass es nun auch möglich ist, komplexere metallische Strukturen effizient zu berechnen.

Aus der Streumatrix können wir nicht nur die optischen Eigenschaften wie Transmission, Reflektion, Absorption und Nahfelder unter Fernfeldeinfall bestimmen, sondern auch die Emission von Objekten aus dem Inneren einer Struktur sowie die optischen Resonanzen eines Systems berechnen. In dieser Arbeit zeigen wir eine effiziente Methode, mit der man dreidimensionale optische Resonanzen direkt aus der Streumatrix ableiten kann [14].

Ausgehend von den Resonanzen eines einzelnen Systems ist es außerdem möglich, mit Hilfe unserer Methode der resonanten Modenkopplung Approximationen für die Resonanzen gestapelter Systeme zu erhalten [15, 16]. Die Methode erlaubt sowohl die Beschreibung des Nahfeld- als auch des Fernfeldregimes für gestapelte Zweischichtsysteme, wobei sogar die starke Kopplung zu Fabry-Perot Moden enthalten ist. Damit sind wir in der Lage, die gegenseitigen Wechselwirkungen solcher Systeme effizient zu untersuchen.

Diese Arbeit ist so angelegt, dass sie dem Leser einen fundamentalen Einblick in den Streumatrixformalismus und die Fourier-modale Methode gewährt. Darüber hinaus beschreiben wir im Detail, wie unsere Erweiterungen zu diesen Methoden funktionieren, und zeigen deren Gültigkeit an verschiedenen Beispielen auf.

Résumé

Les propriétés optiques des nanomatériaux, tels que les cristaux photoniques ou les métamatériaux, ont reçu beaucoup d'attention dans les dernières années [1–9]. La dérivation numérique de ces propriétés se révèle pourtant très compliquée, en particulier dans le cas des structures métallo-diélectriques, qui comportent des résonances plasmoniques. C'est pourquoi des méthodes numériques avancées et des modèles semi-analytiques sont nécessaires. Dans cette thèse, nous montrerons que le formalisme de la matrice de diffraction peut satisfaire ces deux aspects.

La méthode de la matrice de diffraction est un concept très général en physique. Dans le cas des structures périodiques, on peut dériver la matrice de diffraction à l'aide de la méthode modale de Fourier [10]. Pour la description exacte des géométries planes, nous avons développé la méthode des coordonnées adaptées [11], qui nous donne un nouveau système de coordonnées, dans lequel les interfaces des matériaux sont des surfaces de coordonnées constantes. En combinaison avec la méthode de la résolution spatiale adaptative, la méthode des coordonnées adaptées permet d'améliorer considérablement la convergence de la méthode modale de Fourier, de telle sorte qu'on peut calculer des structures métalliques compliquées très efficacement.

Si on utilise la matrice de diffraction, il est non seulement possible de dériver les propriétés optiques en illumination de champ lointain, comme la transmission, la réflexion, l'absorption, et le champ proche, mais aussi de décrire l'émission d'un objet à l'intérieur d'une structure et d'obtenir les résonances optiques d'un sytème. Dans cette thèse, nous présenterons une méthode efficace pour la dérivation des résonances optiques tridimensionnelles, utilisant directement la matrice de diffraction [14].

Si on connaît les résonances d'un système isolé, il est aussi possible d'obtenir une approximation des résonances dans le cas d'un système combiné à l'aide de notre méthode du couplage des résonances [15, 16]. Cette méthode permet de décrire le régime de couplage des champs lointain et proche, y compris le couplage fort avec les résonances Fabry-Perot, pour des systèmes qui se composent d'un empilement de deux structures planes et périodiques. Pour cette raison, on peut étudier efficacement le couplage de ces systèmes.

Cette thèse est écrite de manière à donner une idée d'ensemble du formalisme de la matrice de diffraction et de la méthode modale de Fourier. En outre, nous décrivons notre généralisation de ces méthodes et nous montrons la validité de nos approches pour différents exemples.

Publications

Parts of this work have already been published:

- T. Weiss, G. Granet, N. A. Gippius, S. G. Tikhodeev, and H. Giessen, "Matched coordinates and adaptive spatial resolution in the Fourier modal method," Opt. Express **17**, 8051–8061 (2009).

- T. Weiss, N. A. Gippius, S. G. Tikhodeev, G. Granet, and H. Giessen, "Efficient calculation of the optical properties of stacked metamaterials with a Fourier modal method," J. Opt. A: Pure Appl. Opt. **11**, 114019–1–5 (2009).

- T. Weiss, G. Granet, N. A. Gippius, S. G. Tikhodeev, and H. Giessen, "Calculation of complex shapes in the Fourier modal method through the concept of coordinate transformations," AIP Conf. Proc. **1176**, 163–165 (2009).

- N. A. Gippius, T. Weiss, S. G. Tikhodeev, and H. Giessen, "Resonant mode coupling of optical resonances in stacked nanostructures," Opt. Express **18**, 7569–7574 (2010).

- T. Weiss, N. A. Gippius, R. Taubert, G. Granet, S. G. Tikhodeev, and H. Giessen, "Resonant mode coupling for deriving optical resonances in stacked grating structures," AIP Conf. Proc. **1291**, 97–99 (2010).

- N. Liu, M. Mesch, T. Weiss, M. Hentschel, and H. Giessen, "Infrared perfect absorber and its application as plasmonic sensor," Nano Lett. **10**, 2342–2348 (2010).

- T. Weiss, N. A. Gippius, S. G. Tikhodeev, G. Granet, and H. Giessen, "Derivation of 3D plasmonic resonances in the Fourier modal method with adaptive spatial resolution and matched coordinates," J. Opt. Soc. Am. A **28**, 238–244 (2011).

- B. Gompf, J. Braun, T. Weiss, H. Giessen, M. Dressel, and U. Hübner, "Periodic nanostructures: Spatial dispersion mimics chirality," Phys. Rev. Lett. **106**, 1885501–1–4 (2011).

- N. Liu, A. P. Alivisatos, M. Hentschel, T. Weiss, and H. Giessen, "Towards 3d plasmon rulers," Science **337**, 1407–1410 (2011).

- T. Weiss, N. A. Gippius, G. Granet, S. G. Tikhodeev, R. Taubert, L. Fu, H. Schweizer, and H. Giessen, "Strong resonant mode coupling of Fabry-Perot and grating resonances in stacked two-layer systems," Photonics and Nanostructures, **published online** (2011).

Publications that are not presented in detail:

- N. Liu, L. Langguth, T. Weiss, J. Kästel, M. Fleischhauer, T. Pfau, and H. Giessen, "Plasmonic electromagnetically induced transparency at the Drude damping limit," Nature Materials **8**, 758–762 (2009).

- A. B. Akimov, A. S. Vengurlekar, T. Weiss, N. A. Gippius, and S. G. Tikhodeev, "Surface plasmon polaritons in metallo-dielectric meander-type gratings," Pisma ZhETF **90**, 398–401 (2009).

- L. Fu, H. Schweizer, T. Weiss, and H. Giessen, "Optical properties of metallic meanders," J. Opt. Soc. Am. B **26**, 111–119 (2009).

- N. Liu, T. Weiss, M. Mesch, L. Langguth, U. Eigenthaler, M. Hirscher, C. Sönnichsen, and H. Giessen, "Planar metamaterial analogue of electromagnetically induced transparency for plasmonic sensing," Nano Lett. **10**, 1103–1107 (2010).

- S. V. Lobanov, T. Weiss, N. A. Gippius, and S. G. Tikhodeev, "Emission of oscillating dipoles from a photonic crystal slab of nanopillars," Pisma ZhETF, **in press** (2011).

- T. Weiss, N. A. Gippius, S. G. Tikhodeev, G. Granet, and H. Giessen, "Acceleration of parameter studies in the Fourier modal method by introducing lateral shift matrices," CTN Journal, **in press** (2011).

Publications in preparation:

- R. Taubert, R. Ameling, T. Weiss, A. Christ, and H.Giessen, "From near-field to far-field coupling in three dimensions: Retarded interaction of particle plasmons," **submitted** (2011).

- J. Braun, B. Gompf, T. Weiss, H. Giessen, M. Dressel, and U. Hübner, "Transmission through subwavelength hole arrays in ultrathin metal films," **submitted** (2011).

- D. D. Solnyshkov, T. Weiss, G. Malpuech, N. A. Gippius, "Polariton laser based on a ZnO photonic crystal slab," **submitted** (2011).

1 Introduction

It had been around the end of the 19th century, when people believed that the fundamentals of physics were in principle understood, and new discoveries would be made only for very specialized problems. Most notably, the formulation of the Maxwell's equations [17] turned out to be one of the milestones in physics which led to this assumption. Today, we know that even such a classical field as electrodynamics can still provide a multitude of discoveries that are so fundamental that they open up new paths in science.

Especially, the field of nano-optics has drawn a lot of attention in recent years. Fabrication techniques such as electron beam lithography and focused ion beam etching provide means to fabricate particles of feature sizes in the range of the optical wavelengths with optical properties that have not been achieved so far.

A remarkable type of materials are the so-called photonic crystals [18–21], which consist of periodically arranged structures with a period in the order of the wavelength of light and provide band gaps for the propagation of photons similar to the band gaps for electrons in standard crystals [22]. This allows a confinement of light, either in one or two dimensions for new types of waveguides (see, e.g., [23]) and fibers (also known as photonic crystal fibers [24]), or in all three spatial directions for a strong localized field enhancement [25].

When the particle size is decreased below the wavelength of light, we enter the region of so-called metamaterials [26–29]. Owing to the small feature size, the light interacts with the metamaterial as a kind of effective material because several metamaterial particles (so-called meta-atoms [30]) are excited over one wavelength. Depending on the meta-atoms and their spatial arrangement, the metamaterial can be designed such that it provides specific optical properties that are not available in nature, which allows the construction of optimized optical devices for various applications.

A very prominent example of metamaterials is that of a material with a negative refractive index [31–34], which allows – at least theoretically – the construction of a perfect lens [26]. Another application of metamaterials is a cloaking device that bends the light around an object, so that this object seems to be invisible [27]. For a single wavelength and a single incident polarization, it has been demonstrated in the microwave regime that such a device can in principle be fabricated [28]. Similarly, it has been shown in the optical regime that an object can be hidden under a carpet cloak on a reflecting surface [35].

Many ideas for new metamaterials evolve from the field of transformation optics [36], which uses the fact that Maxwell's equations can be formulated

invariantly under coordinate transformations, when we redefine the permittivity and permeability tensors [37]. Thus, non-uniform coordinate systems and non-trivial permittivity and permeability distributions provide the same result. Hence, we can construct a deformed space, in which the light propagates in an unusual way. The equivalence principle then provides us permittivity and permeability distributions that lead to the same physical behavior. The remaining problem is to construct a metamaterial that exhibits such artificial material properties.

Owing to the challenging task of constructing appropriate metamaterials, it is essential to analyze the role of the individual meta-atoms in detail. A lot of work has been devoted to this subject, especially by Liu et al. [9, 38–41]. Thus, it has been possible to construct new optically active and polarization sensitive materials [42, 43], as well as structures mimicking quantum-mechanical effects such as electromagnetically induced transparency [9, 44]. Possible applications would be sensor devices [45], perfect absorbers [46], and measurements of the spatial arrangement of molecules with so-called plasmon rulers [47].

Many metamaterials and photonic crystals contain metallic particles which exhibit so-called plasmonic resonances. Plasmon resonances occur due to collective oscillations of free electrons in metallic structures and can be either delocalized surface plasmon polaritons that propagate along a metallo-dielectric interface [2, 3, 6, 21, 48], or localized particle resonances [49, 50]. A well-known example of localized plasmon resonances is the bright color of windows in medieval churches, which is caused by metallic nanoparticles inside the glass.

The advantage of plasmonic resonances is a strong light-matter interaction, which has been applied for constructing nanoantennas [51], for instance, in order to enhance the emission of light from quantum dots [52]. Furthermore, plasmonic resonances are often used for constructing metamaterials with a negative refractive index, because the resonant phenomenon can provide a negative permeability, which leads in combination with the negative real part of the metallic permittivity to a negative refractive index [32–34]. Other work has been devoted to the interaction of localized and delocalized plasmonic resonances with different kinds of optical resonances such as slab waveguide modes [53, 54].

Unfortunately, nanoparticles are too small for a simplified description of their optical properties in standard ray optics and – in most cases – yet too large for a quasi-static approximation of Maxwell's equations. Hence, Maxwell's equations have to be solved either analytically or numerically. As there are only a few systems such as spheres [55] and infinite cylinders [56] with a known analytical solution, most problems have to be solved numerically. This is especially challenging in the case of metallo-dielectric structures, which usually require an accurate description of the interfaces between metallic

and dielectric materials.

There are plenty of methods available for solving Maxwell's equations numerically. In general, they can be distinguished as time domain and frequency domain solvers. In the case of the former, the time dependence of Maxwell's equations is discretized, leading to a system of equations that can be solved usually rather quickly. The downside of most time domain solvers is on the one hand a reduced accuracy in calculations with non-rectangular structures; on the other hand it is difficult to describe dispersive material parameters correctly. A common commercial time domain solver is the finite integral method of CST microwave studio [57]. Other approaches use the finite difference time domain method or the discontinuous Galerkin time domain method [58].

In the case of frequency domain solvers, only one frequency is considered in each calculation, and the time-harmonic Maxwell's equations are solved. Typical frequency solvers use the finite element method [59, 60], which has the advantage that one can include adaptive meshes for an appropriate description of arbitrary shapes. The disadvantages of all frequency domain solvers are a restriction to linear material response as well as an increased calculation time compared to time domain solvers. In this work, we focus on the Fourier modal method as a special frequency solver, which is well-suited and fast for stacks of periodic layers. Nevertheless, within this approach, it is – in contrast to the finite element method – difficult to describe arbitrary shapes correctly.

2 Fourier modal method and scattering matrix

2.1 Introduction

The Fourier modal method (FMM), also known as rigorous coupled wave approach or scattering matrix method,[1] is one of the most popular numerical methods for deriving the optical properties of stacked grating structures. Its history started more than 40 years ago with volume gratings consisting of simple sinusoidal permittivity variations [61]. Nowadays, the method is widely used in the fields of photonic crystals [53, 62], metamaterials [63–67], and plasmonics [68]. An interested reader will get a short overview of the development of the Fourier modal method in reference [69]. In this chapter, we present the state of the art techniques in the Fourier modal method, which are commonly used and provided the basis for the extensions developed in this work.

One of the most remarkable features of the Fourier modal method is the fact that its formulation remains very simple. Assuming an invariance under translation in one spatial direction, it is straight-forward to derive from Maxwell's equations an eigenvalue problem for field distributions that can propagate or decay forward or backward in the direction of invariance with only a change in the global phase and amplitude [10]. Whenever the system of interest is periodic in two other spatial directions, which do not coincide with the direction of translation invariance, it is possible to solve the eigenvalue problem effectively by an expansion in truncated Fourier series. The solutions are so-called Fourier-Bloch modes, which span the subspace of general solutions within such a layer of translation invariance and explain the origin of the name Fourier modal method. For constructing the optical properties of several stacked layers with identical directions of invariance, the solutions of neighboring layers can be combined by considering the correct boundary conditions [62, 70, 71].

The required periodicity is both an advantage and a disadvantage, as it restricts the Fourier modal method to specific geometries, but simultaneously includes a correct formulation of periodic boundary conditions intrinsically. A clear downside of the method is the required translation invariance. Hence,

---

[1]In fact, the name scattering matrix method refers to a special form of the Fourier modal method using the scattering matrix formalism for the description of stacked layers.

the Fourier modal method can be applied only to systems that can be separated into several planar layers effectively (see figure 2.1). Still, the method is applicable to most of the standard problems in modern grating systems, because these structures are usually fabricated by techniques such as electron beam lithography or focused ion beam etching, which are also limited to planar structures.
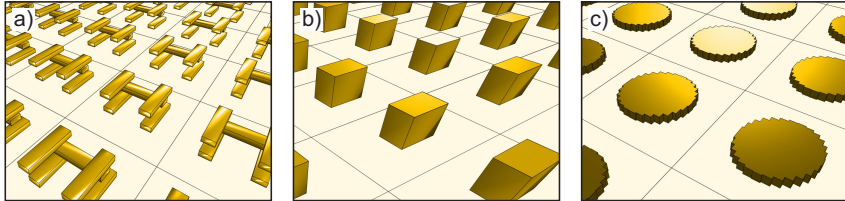

Figure 2.1: Typical structures for calculations with the Fourier modal method: (a) Periodic multilayer structure with rectangular geometry; (b) Skewed structure with non-orthogonal directions of periodicity and translation invariance; (c) Cylinders approximated by zig-zag lines.

In its original formulation, a poor convergence behavior was noticed for the transverse magnetic (TM) polarization in one-dimensional gratings, whereas calculations of two-dimensional gratings seemed to be practically impossible. Some attempts have been made in order to improve the convergence behavior by a reformulation of the involved eigenvalue problem [72, 73]. Then, in 1996, Lifeng Li provided a detailed analysis as regards the convergence behavior of the involved products in Fourier space and formulated the so-called factorization rules [74], which finally led to a systemically optimized eigenvalue problem of the Fourier modal method [10, 75].

Still, the convergence behavior of the Fourier modal method was not very convincing in the case of metallo-dielectric structures. The reason is that the permittivity distribution of such structures exhibits a jump in the real part from positive to negative values, so that the truncated Fourier expansion of the real part passes through zero at the interface, leading to a singularity in cases where the imaginary part equals zero. In addition, the contrast between the permittivity of the metallic and the dielectric area is rather large. Hence, the description of the discontinuous permittivity distribution is hampered by the over- and undershoots due to the Gibbs phenomenon. In order to improve the convergence behavior beyond the limits of the factorization rules, it has been suggested to introduce a coordinate transformation such that the spatial resolution is increased close to the jump discontinuities [12, 13]. This so-called adaptive spatial resolution allows an efficient calculation of metallo-

dielectric structures, because the jump discontinuities are much smaller in the transformed coordinates than in the original physical space [76].

However, the application of the correct Fourier factorization in combination with adaptive spatial resolution is only straight-forward in cases where the lateral interfaces coincide with the directions of periodicity (see examples in figure 2.1). Therefore, it is possible to calculate the optical properties of skewed geometries [10], whereas even simple shapes such as cylinders have to be approximated by zig-zag lines. Several extensions have been made to the concept of factorization rules [77] and its application to arbitrary interface geometries [78–80]. In this work, we present the scheme of matched coordinates as an alternative approach for the description of more or less arbitrary interface geometries that allows us to also include the concept of adaptive spatial resolution efficiently [11, 81].

Although the Fourier modal method is designed for linear phenomena and periodic structures, it is worth mentioning that it is possible to extend the method to aperiodic structures [82–84] as well as to nonlinear material response [85, 86].

2.2 Conventions

If not stated otherwise, we use a covariant notation with sum convention in this work, as it turned out to be most efficient for the description of the occurring equations, because it allows a simple application of coordinate transformations. The components of three-dimensional vectors will be denoted by Greek subscripts or superscripts, whereas Latin letters usually indicate elements of the infinite or truncated Fourier expansions. The underlying unit system is centimeter, gram, second (cgs).

Let us define a coordinate system $Ox^1x^2x^3$ with the x^3 axis as the direction of translation invariance and the x^1 and the x^2 axes as the two lateral directions of periodicity. Note that the structures of interest can be also invariant under translations in the directions x^1 and x^2. In this case, we can attribute a pseudo-period of arbitrary length along such directions. If the complete structure is periodic in only one of the two lateral directions but translation invariant in the other direction, we define x^1 as the direction of periodicity and refer to the structure as *one-dimensional*. If the structure has two directions of periodicity,[2] we call it *two-dimensional*.

The physical coordinate system $Oxyz = O\overline{x}^1\overline{x}^2\overline{x}^3$ is related to the coordinate system $Ox^1x^2x^3$ such that the x^1 axis coincides with the $\overline{x}^1$ axis (see

---

[2]Strictly speaking, we can attribute infinitely many lateral directions of periodicity to a two-dimensional periodic structure. For the sake of simplicity, we count in this case only the directions of periodicity with the smallest periods.

figure 2.2), the x^2 axis is located in the $\overline{x}^1\overline{x}^2$ plane and inclined by an angle ζ with respect to the $\overline{x}^2$ axis; the orientation of the x^3 axis is defined by the angles χ and ξ as polar and azimuth, respectively. The coordinates in the skewed coordinate system $Ox^1x^2x^3$ are related to the physical coordinates as follows [10]:

$$x = \overline{x}^1 = x^1 + x^2 \sin\zeta + x^3 \sin\chi\cos\xi \,, \tag{2.1a}$$

$$y = \overline{x}^2 = x^2 \cos\zeta + x^3 \sin\chi\sin\xi \tag{2.1b}$$

$$z = \overline{x}^3 = x^3 \cos\chi \,. \tag{2.1c}$$

For most of the practical applications, $\chi = \xi = 0$. However, we decided to keep the description of the Fourier modal method as general as possible regarding the inclination, because the concept of inclined coordinate systems discussed by Li [10] is very similar to what we introduce as the concept of matched coordinates in the following chapter 3.
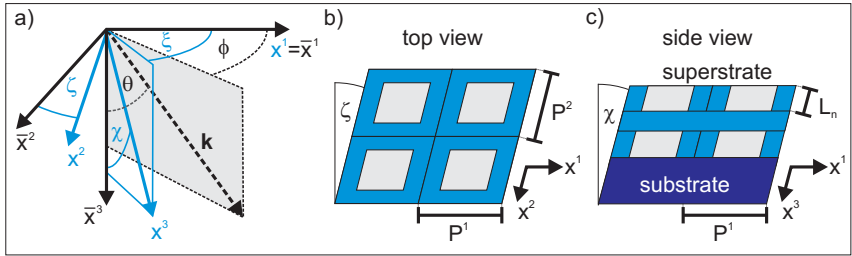
Figure 2.2: Definition of an orthonormal coordinate system $O\overline{x}^1\overline{x}^2\overline{x}^3$ and a skewed coordinate system $Ox^1x^2x^3$ as well as the orientation of the incidence wave vector. Panel (b) and (c) depict the schematic of a typical multilayer structure used in the Fourier modal method in top and side view, respectively.

In general, the structure of interest is illuminated from the top via far field incidence with an incident wave vector $\mathbf{k}$. The orientation of the $\overline{x}^3$ axis is chosen such that the projection of the incident wave vector on the $\overline{x}^3$ axis results in a positive value. The wave vector itself can be defined in the system $O\overline{x}^1\overline{x}^2\overline{x}^3$ by the angles θ and ϕ (see figure 2.2a) as well as its absolute value $k_0 n_0$, where n_0 denotes the refractive index of the homogeneous superstrate layer on top of the structure of interest (see figure 2.2c), and $k_0 = \omega/c$. In the coordinate system $Ox^1x^2x^3$, the covariant in-plane components k_1 and k_2 obey:

$$k_1 = k_0 n_0 \sin\theta\cos\phi \,, \qquad k_2 = k_0 n_0 \sin\theta\sin(\phi + \zeta) \,. \tag{2.2}$$

In this work, the occurring materials are described by anisotropic permittivity and permeability tensors $\underline{\underline{\varepsilon}}$ and $\underline{\underline{\mu}}$, neglecting bi-anisotropy as well as any higher order contributions. Thus, Maxwell's equations remain linear and we can assume a time dependence $\exp(-i\omega t)$, which we omit throughout this work for the sake of simplicity.

2.3 Solution for Maxwell's equations in one layer

Let us now focus on the solution of Maxwell's equations inside a layer with translation invariance. Note that we keep the formulation as general as possible and follow more or less the descriptions in reference [10], with some extensions towards the concept of matched coordinates [11, 81].

2.3.1 Covariant formulation of Maxwell's equations

Owing to the general description in skewed coordinates, it is appropriate to formulate Maxwell's equations in a covariant form that is invariant under well-behaved coordinate transformations [36, 37]. For instance, the curl equations read in the covariant form as follows:

$$
\boxed{
\begin{aligned}
\nabla \times \mathbf{E} = ik_0\underline{\underline{\mu}}\mathbf{H} \quad &\Rightarrow \quad \epsilon^{\alpha\beta\gamma}\partial_\beta E_\gamma = ik_0\mu^{\alpha\beta}H_\beta\,, \\
\nabla \times \mathbf{H} = -ik_0\underline{\underline{\varepsilon}}\mathbf{E} + \frac{4\pi}{c}\mathbf{j} \quad &\Rightarrow \quad \epsilon^{\alpha\beta\gamma}\partial_\beta H_\gamma = -ik_0\varepsilon^{\alpha\beta}E_\beta + \frac{4\pi}{c}j^\alpha\,.
\end{aligned}
}
\tag{2.3}
$$

The bold letters $\mathbf{E}$ and $\mathbf{H}$ indicate the electric and magnetic field vectors, the corresponding covariant components are E_α and H_α, respectively. They are related with the orthonormal components $\overline{E}_\alpha$ and $\overline{H}_\alpha$ by the standard transformation of covariant tensors with rank one and weight zero:

$$
E_\alpha = \frac{\partial \overline{x}^\beta}{\partial x^\alpha}\overline{E}_\beta\,, \qquad H_\alpha = \frac{\partial \overline{x}^\beta}{\partial x^\alpha}\overline{H}_\beta\,.
\tag{2.4}
$$

The expression $\epsilon^{\alpha\beta\gamma}$ in equation (2.3) denotes the Levi-Civita symbol, with

$$
\epsilon^{\alpha\beta\gamma} = \begin{cases} 1 & \text{for } \alpha\beta\gamma = 123, 231, 312\,; \\ -1 & \text{for } \alpha\beta\gamma = 321, 213, 132\,; \\ 0 & \text{otherwise}\,. \end{cases}
\tag{2.5}
$$

The contravariant components of the permittivity and permeability tensors $\varepsilon^{\alpha\beta}$ and $\mu^{\alpha\beta}$ transform as relative contravariant tensors of rank two and weight one:

$$
\boxed{
\varepsilon^{\alpha\beta} = \sqrt{g}\frac{\partial x^\alpha}{\partial \overline{x}^\gamma}\frac{\partial x^\beta}{\partial \overline{x}^\delta}\overline{\varepsilon}^{\gamma\delta}\,, \qquad \mu^{\alpha\beta} = \sqrt{g}\frac{\partial x^\alpha}{\partial \overline{x}^\gamma}\frac{\partial x^\beta}{\partial \overline{x}^\delta}\overline{\mu}^{\gamma\delta}\,.
}
\tag{2.6}
$$

Here, g denotes the determinant of the metric components $g_{\alpha\beta}$, which are defined as

$$g_{\alpha\beta} = \sum_{\gamma=1}^{3} \frac{\partial \overline{x}^\gamma}{\partial x^\alpha} \frac{\partial \overline{x}^\gamma}{\partial x^\beta} \,. \tag{2.7}$$

Thus, the square root of g equals the following Jacobian determinant:

$$\sqrt{g} = \det \left[\frac{\partial(\overline{x}^1, \overline{x}^2, \overline{x}^3)}{\partial(x^1, x^2, x^3)} \right] = \det \begin{pmatrix} \frac{\partial \overline{x}^1}{\partial x^1} & \frac{\partial \overline{x}^1}{\partial x^2} & \frac{\partial \overline{x}^1}{\partial x^3} \\ \frac{\partial \overline{x}^2}{\partial x^1} & \frac{\partial \overline{x}^2}{\partial x^2} & \frac{\partial \overline{x}^2}{\partial x^3} \\ \frac{\partial \overline{x}^3}{\partial x^1} & \frac{\partial \overline{x}^3}{\partial x^2} & \frac{\partial \overline{x}^3}{\partial x^3} \end{pmatrix} . \tag{2.8}$$

In the case of isotropic tensors with scalar permittivity and permeability values ε and μ, equation (2.6) simplifies to

$$\varepsilon^{\alpha\beta} = \sqrt{g}g^{\alpha\beta}\varepsilon \,, \qquad \mu^{\alpha\beta} = \sqrt{g}g^{\alpha\beta}\mu \,, \tag{2.9}$$

with $g^{\alpha\beta}$ as the conjugate metric components. They obey the relation $\delta_\beta^\alpha = g^{\alpha\gamma}g_{\gamma\beta}$, where δ_β^α stands for the Kronecker delta. In particular,

$$g^{\alpha\beta} = \sum_{\gamma=1}^{3} \frac{\partial x^\alpha}{\partial \overline{x}^\gamma} \frac{\partial x^\beta}{\partial \overline{x}^\gamma} \,. \tag{2.10}$$

The general source terms in Maxwell's equations transform also as relative tensors of weight one:

$$j^\alpha = \sqrt{g} \, \frac{\partial x^\alpha}{\partial \overline{x}^\beta} \overline{j}^\beta \,, \qquad \varrho = \sqrt{g} \, \overline{\varrho} \,. \tag{2.11}$$

With the general charge term ϱ, we find for the covariant form of Maxwell's divergence equations [36]:

$$\boxed{\begin{aligned} \nabla \cdot \mathbf{D} = 4\pi\varrho &\quad \Rightarrow \quad \partial_\alpha D^\alpha = 4\pi\varrho \,, \\ \nabla \cdot \mathbf{B} = 0 &\quad \Rightarrow \quad \partial_\alpha B^\alpha = 0 \,. \end{aligned}} \tag{2.12}$$

Here, D^α and B^α denote the contravariant components of the generalized electric displacement and magnetic induction, respectively. Note that D^α and B^α transform as relative contravariant tensors of weight one in order to keep the form of equation (2.12) invariant. For instance, we find for the electric displacement:

$$D^\alpha = \varepsilon^{\alpha\beta} E_\beta = \sqrt{g} \frac{\partial x^\alpha}{\partial \overline{x}^\gamma} \frac{\partial x^\beta}{\partial \overline{x}^\delta} \overline{\varepsilon}^{\gamma\delta} E_\beta = \sqrt{g} \frac{\partial x^\alpha}{\partial \overline{x}^\gamma} \overline{\varepsilon}^{\gamma\delta} \overline{E}_\delta = \sqrt{g} \frac{\partial x^\alpha}{\partial \overline{x}^\gamma} \overline{D}^\gamma \,. \tag{2.13}$$

2.3.2 Eigenvalue equation

In the Fourier modal method, no layer contains any charges or currents.[3] Furthermore, the permittivity and permeability tensors $\varepsilon^{\alpha\beta}$ and $\mu^{\alpha\beta}$ are periodic with respect to x^1 and x^2 with periods P^1 and P^2, respectively. Hence, we find for any integer values m, n:

$$\varepsilon^{\alpha\beta}(x^1+mP^1, x^2+nP^2, x^3) = \varepsilon^{\alpha\beta}(x^1, x^2, x^3)\,,$$
$$\mu^{\alpha\beta}(x^1+mP^1, x^2+nP^2, x^3) = \mu^{\alpha\beta}(x^1, x^2, x^3)\,. \tag{2.14}$$

Owing to the periodicity, we can use Bloch's theorem and employ the following ansatz for the electric and magnetic field:

$$F_\alpha(x^1, x^2, x^3) = e^{ik_1x^1+ik_2x^2} f_\alpha(x^1, x^2, x^3)\,. \tag{2.15}$$

Here, F_α stands for either the electric or magnetic field component, and $f_\alpha(x^1, x^2, x^3)$ indicates a periodic function with respect to x^1 and x^2. The terms k_α with $\alpha = 1, 2$ are conserved in all layers and equal the lateral components of the incident wave vector.

The next steps for deriving the master equation of the Fourier modal method can be interchanged in their order. We suggest to start with inserting equation (2.15) in the covariant form of the curl Maxwell equations (2.3) and to Fourier transform the results in the lateral directions x^1 and x^2. Thus, we obtain for the curl of the magnetic field [10]:

$$K_{2n}H_{3mn} + i\partial_3 H_{2mn} = -k_0 \sum_{p,q} \hat{\varepsilon}^{1\alpha}_{mn,pq} E_{\alpha pq}\,, \tag{2.16a}$$

$$-i\partial_3 H_{1mn} - K_{1m}H_{3mn} = -k_0 \sum_{p,q} \hat{\varepsilon}^{2\alpha}_{mn,pq} E_{\alpha pq}\,, \tag{2.16b}$$

$$K_{1m}H_{2mn} - K_{2n}H_{1mn} = -k_0 \sum_{p,q} \hat{\varepsilon}^{3\alpha}_{mn,pq} E_{\alpha pq}\,. \tag{2.16c}$$

Similarly, the curl of the electric field yields in Fourier space [10]:

$$K_{2n}E_{3mn} + i\partial_3 E_{2mn} = k_0 \sum_{p,q} \hat{\mu}^{1\alpha}_{mn,pq} H_{\alpha pq}\,, \tag{2.17a}$$

$$-i\partial_3 E_{1mn} - K_{1m}E_{3mn} = k_0 \sum_{p,q} \hat{\mu}^{2\alpha}_{mn,pq} H_{\alpha pq}\,, \tag{2.17b}$$

$$K_{1m}E_{2mn} - K_{2n}E_{1mn} = k_0 \sum_{p,q} \hat{\mu}^{3\alpha}_{mn,pq} H_{\alpha pq}\,. \tag{2.17c}$$

---

[3]It is in principle possible to solve the emission problem with an oscillating point dipole inside the structure of interest by reformulating the boundary problem at the interface between two adjacent layers [70], but the discussion on this topic is beyond the scope of this work.

The reciprocal space representations $E_{\alpha mn}$ and $H_{\alpha mn}$ of the electric and magnetic field evolve from the Fourier transform of the periodic function $f_\alpha(x^1, x^2, x^3)$ that has been introduced in equation (2.15), and still depend on x^3:

$$F_{\alpha mn}(x^3) = \frac{1}{P^1 P^2} \int_V f_\alpha(x^1, x^2, x^3) e^{-iG_{1m}x^1 - iG_{2n}x^2} \mathrm{d}x^1 \mathrm{d}x^2. \qquad (2.18)$$

In this case, V denotes the area of one unit cell, and $G_{\alpha m}$ are the covariant components of the reciprocal lattice vectors $\mathbf{G}_{mn}$ with $G_{\alpha m} = 2\pi m / P^\alpha$ for $m \in \mathbb{Z}$. The terms $K_{\alpha m}$ in equations (2.16a) to (2.17c) originate from the derivative operators in direction α and are related to the reciprocal lattice vectors as $K_{\alpha m} = k_\alpha + G_{\alpha m}$.

The most complicated expressions in the reciprocal curl Maxwell equations (2.16a) to (2.17c) are $\hat{\varepsilon}^{\alpha\beta}_{mn,pq}$ and $\hat{\mu}^{\alpha\beta}_{mn,pq}$ as the Fourier representations of the permittivity and permeability tensors. In a straight-forward calculation, they are connected with the spatial tensors by the following relation:

$$\hat{f}^{\alpha\beta}_{mn,pq}(x^3) = \frac{1}{P^1 P^2} \int_V f^{\alpha\beta}(x^1, x^2, x^3) e^{-i(G_{1m} - G_{1p})x^1 - i(G_{2n} - G_{2q})x^2} \mathrm{d}x^1 \mathrm{d}x^2.$$

$$(2.19)$$

However, this so-called Laurent's rule is only correct in an infinite Fourier space. A detailed analysis of the Laurent's rule in a truncated Fourier space yields a poor convergence in the case of discontinuous functions. In order to overcome this problem, Li developed the factorization rules for discontinuous functions [74], where it is suggested to reformulate the Laurent's rule under certain conditions. We will discuss the factorization rules in detail in section 2.5. For the moment, the reader may consider $\hat{\varepsilon}^{\alpha\beta}_{mn,pq}$ and $\hat{\mu}^{\alpha\beta}_{mn,pq}$ simply as the Fourier representations of the permittivity and permeability tensors that can be obtained by well-defined operations.

The next step towards the master equation of the Fourier modal method is to eliminate the E_3 and H_3 components in equations (2.16a) to (2.17c), which is rather lengthy and tedious. However, we can display the results in a compact form by introducing the operator $\hat{l}^\pm_\gamma$ of reference [10]. This operator applied to an arbitrary 3×3 matrix A results in the matrix $\tilde{A} \equiv \hat{l}^\pm_\gamma(A)$ with the following components:

$$\tilde{A}^{\alpha\beta} = \begin{cases} (A^{\gamma\gamma})^{-1} & \text{for } \alpha = \gamma, \, \beta = \gamma; \\ (A^{\gamma\gamma})^{-1} A^{\gamma\beta} & \text{for } \alpha = \gamma, \, \beta \neq \gamma; \\ A^{\alpha\gamma}(A^{\gamma\gamma})^{-1} & \text{for } \alpha \neq \gamma, \, \beta = \gamma; \\ A^{\alpha\beta} \pm A^{\alpha\gamma}(A^{\gamma\gamma})^{-1} A^{\gamma\beta} & \text{for } \alpha \neq \gamma, \, \beta \neq \gamma. \end{cases} \qquad (2.20)$$

Note that the elements of A can be also elements of a finite or infinite Hilbert space, so that the inverse has to be understood as an operator. For instance, we can define

$$\tilde{\varepsilon} = \hat{l}_3^-(\varepsilon), \qquad \tilde{\mu} = \hat{l}_3^-(\hat{\mu}), \qquad (2.21)$$

where $\hat{\varepsilon}$ and $\hat{\mu}$ are 3×3 block matrices with elements $\hat{\varepsilon}_{mn,pq}^{\alpha\beta}$ and $\hat{\mu}_{mn,pq}^{\alpha\beta}$ that evolve from the Fourier transform of the generalized permeability and permittivity tensor elements defined by equation (2.6).

Thus, the elimination of E_3 and H_3 in equations (2.16a) to (2.17c) leads to

$$-i\partial_3 \underbrace{\begin{pmatrix} \vec{\mathcal{E}}_{||} \\ \vec{\mathcal{H}}_{||} \end{pmatrix}}_{\equiv \vec{\mathcal{F}}_{||}} = \underbrace{\begin{bmatrix} \hat{\mathcal{N}}(\tilde{\mu}, \tilde{\varepsilon}) & -\hat{\mathcal{L}}(\tilde{\mu}, \tilde{\varepsilon}) \\ \hat{\mathcal{L}}(\tilde{\varepsilon}, \tilde{\mu}) & \hat{\mathcal{N}}(\tilde{\varepsilon}, \tilde{\mu}) \end{bmatrix}}_{\equiv \mathcal{M}} \underbrace{\begin{pmatrix} \vec{\mathcal{E}}_{||} \\ \vec{\mathcal{H}}_{||} \end{pmatrix}}_{\equiv \vec{\mathcal{F}}_{||}}, \qquad (2.22)$$

with the tensor operators

$$\hat{\mathcal{N}}(\mathcal{A}, \mathcal{B}) = \begin{pmatrix} -\mathcal{A}^{23}\mathcal{K}_2 - \mathcal{K}_1\mathcal{B}^{31} & \mathcal{A}^{23}\mathcal{K}_1 - \mathcal{K}_1\mathcal{B}^{32} \\ \mathcal{A}^{13}\mathcal{K}_2 - \mathcal{K}_2\mathcal{B}^{31} & -\mathcal{A}^{13}\mathcal{K}_1 - \mathcal{K}_2\mathcal{B}^{32} \end{pmatrix}, \qquad (2.23)$$

$$\hat{\mathcal{L}}(\mathcal{A}, \mathcal{B}) = \frac{1}{k_0} \begin{pmatrix} -k_0^2\mathcal{A}^{21} - \mathcal{K}_1\mathcal{B}^{33}\mathcal{K}_2 & -k_0^2\mathcal{A}^{22} + \mathcal{K}_1\mathcal{B}^{33}\mathcal{K}_1 \\ k_0^2\mathcal{A}^{11} - \mathcal{K}_2\mathcal{B}^{33}\mathcal{K}_2 & k_0^2\mathcal{A}^{12} + \mathcal{K}_2\mathcal{B}^{33}\mathcal{K}_1 \end{pmatrix}. \qquad (2.24)$$

In this case, $\mathcal{A}$ and $\mathcal{B}$ denote 3×3 block tensors. Furthermore, we define $\mathcal{K}_\alpha$ as the derivative operator, which is a diagonal matrices with elements

$$(\mathcal{K}_1)_{mn,pq} = K_{1m}\delta_{mp}\delta_{nq}, \qquad (\mathcal{K}_2)_{mn,pq} = K_{2n}\delta_{mp}\delta_{nq}. \qquad (2.25)$$

Note the following conventions. By calligraphic letters $\vec{\mathcal{X}}$ with vector symbols, we denote either the full set of Fourier coefficients X_{mn} as defined by equation (2.18) or – in order to cope with the vectorial quantities in Maxwell's equations – a block vector with blocks consisting of such sets of coefficients. For instance, the vectors $\vec{\mathcal{E}}_{||}$ and $\vec{\mathcal{H}}_{||}$ represent the lateral components of the electric and magnetic field, respectively:

$$\vec{\mathcal{E}}_{||} = \begin{pmatrix} \vec{\mathcal{E}}_1 \\ \vec{\mathcal{E}}_2 \end{pmatrix}, \qquad \vec{\mathcal{H}}_{||} = \begin{pmatrix} \vec{\mathcal{H}}_1 \\ \vec{\mathcal{H}}_2 \end{pmatrix}. \qquad (2.26)$$

Furthermore, we usually distinguish by calligraphic letters $\mathcal{X}$ without vector symbols the full Fourier representation of a matrix operator from its element-wise representation $X_{mn,pq}$ defined by equation (2.19). In some cases, calligraphic letters may also be used for block matrix operators, where each block consists of matrix operators $\mathcal{X}$ with elements $X_{mn,pq}$ [see, e.g., the operator $\mathcal{M}$ defined in equation (2.22)].

The matrix and vector notations are motivated by the numerical calculations, where $\mathcal{X}$ becomes a finite matrix of size $N_G \times N_G$, and $\vec{\mathcal{X}}$ is a column vector of size $N_G \times 1$ in a truncated Fourier space with a total amount of N_G Fourier harmonics.

So far, we have made no assumptions on the x^3 dependence of the permeability and permittivity tensors defined by equation (2.6). If we consider a layer with a translation invariance along the x^3 axis, the matrix $\mathcal{M}$ in equation (2.22) is constant, so that we can construct a general solution of equation (2.22) by linear combination of vectors $\vec{\mathcal{F}}_{\|\,n}$ that solve the eigenvalue equation

$$\lambda_n \vec{\mathcal{F}}_{\|\,n} = \mathcal{M} \vec{\mathcal{F}}_{\|\,n}\,. \tag{2.27}$$

This is the master equation of the Fourier modal method [10]. Its solutions represent field distributions with a spatial dependence

$$F_\alpha^{(n)}(x^1, x^2, x^3) = e^{ik_1 x^1 + ik_2 x^2 + i\lambda_n x^3} \sum_{p,q} F_{\alpha pq}^{(n)} e^{iG_{1p} x^1 + iG_{2q} x^2}\,, \tag{2.28}$$

where F_α denotes either E_α or H_α. As the vectors $\vec{\mathcal{F}}_{\|\,n}$ originate from Bloch's theorem and span the eigenvector space of $\mathcal{M}$, such field distributions are called Fourier-Bloch modes. They can propagate and decay forward or backward in the direction of translation invariance without changing their lateral shape. It is therefore convenient to distinguish them by their direction of propagation or decay as regards the x^3 axis and summarize the eigenvalues into subsets $\{\lambda_n^+\}$ and $\{\lambda_n^-\}$, where $\{\lambda_n^\pm\}$ contains eigenvalues λ_n with either positive or negative imaginary part for forward or backward decay, respectively. In the special case that an eigenvalue λ_n is purely real, we assign it to $\{\lambda_n^\pm\}$ in dependence on the sign of the real part.

In the case of a truncated Fourier space, equation (2.27) can be solved by standard tools of linear algebra. Throughout this work, we use a rectangular truncation with $G_{\alpha m} = 2\pi m/P^\alpha$ for $m = 0, \pm 1, \pm 2, ..., \pm N_\alpha$, and $N_G = (2N_1 + 1) \times (2N_2 + 1)$.

As mentioned above, we can construct a general solution of equation (2.27) by linear combination. In compact matrix notation, we find:

$$\begin{bmatrix} \vec{\mathcal{E}}_\|(x^3) \\ \vec{\mathcal{H}}_\|(x^3) \end{bmatrix} = \underbrace{\begin{pmatrix} \mathcal{E}_\|^+ & \mathcal{E}_\|^- \\ \mathcal{H}_\|^+ & \mathcal{H}_\|^- \end{pmatrix}}_{\equiv \mathcal{F}_\|} \begin{bmatrix} \exp(i\Lambda^+ x^3) & 0 \\ 0 & \exp(i\Lambda^- x^3) \end{bmatrix} \begin{pmatrix} \vec{\mathbb{A}}^+ \\ \vec{\mathbb{A}}^- \end{pmatrix}\,.$$

$$\tag{2.29}$$

The vectors $\vec{\mathbb{A}}^\pm$ contain a set of coefficients that define the amplitude and phase of the Fourier-Bloch modes at $x^3 = 0$. The x^3 dependence is determined by

the matrices $\exp(i\Lambda^{\pm}x^3)$, where $\Lambda^{\pm}$ denotes a diagonal matrix with diagonal elements $\lambda_n^{\pm}$. The corresponding eigenvectors are assigned as columns to the so-called material matrix $\mathcal{F}_{||}$ [62] with equally sized blocks $\mathcal{E}_{||}^{\pm}$ and $\mathcal{H}_{||}^{\pm}$ for the electric and magnetic field in forward and backward direction, respectively.

The Fourier representation of E_3 and H_3 can be derived from equation (2.16c) and (2.17c):

$$
\begin{bmatrix} \vec{\mathcal{E}}_3(x^3) \\ \vec{\mathcal{H}}_3(x^3) \end{bmatrix} = \begin{pmatrix} -\tilde{\varepsilon}^{31} & -\tilde{\varepsilon}^{32} & \dfrac{\tilde{\varepsilon}^{33}}{k_0}\mathcal{K}_2 & -\dfrac{\tilde{\varepsilon}^{33}}{k_0}\mathcal{K}_1 \\ -\dfrac{\tilde{\mu}^{33}}{k_0}\mathcal{K}_2 & \dfrac{\tilde{\mu}^{33}}{k_0}\mathcal{K}_1 & -\tilde{\mu}^{31} & -\tilde{\mu}^{32} \end{pmatrix} \begin{bmatrix} \vec{\mathcal{E}}_1(x^3) \\ \vec{\mathcal{E}}_2(x^3) \\ \vec{\mathcal{H}}_1(x^3) \\ \vec{\mathcal{H}}_2(x^3) \end{bmatrix} . \quad (2.30)
$$

2.3.3 Special tensors

In section 2.3.2, we allowed any kind of periodic permittivity and permeability tensors. Significant simplifications occur, when we assume that $\varepsilon^{3\alpha}$ and $\varepsilon^{\alpha3}$ as well as $\mu^{3\alpha}$ and $\mu^{\alpha3}$ are identical to zero for $\alpha \neq 3$. Consequently, the tensor $\hat{\mathcal{N}}$ defined by equation (2.23) equals zero, too. Hence, we can eliminate, for instance, the Fourier representation of the magnetic field in equation (2.27) [75] and solve the simplified eigenvalue equation

$$
(\lambda_n^{\pm})^2 \vec{\mathcal{E}}_{||\,n}^{\pm} = -\hat{\mathcal{L}}(\tilde{\mu}, \tilde{\varepsilon})\hat{\mathcal{L}}(\tilde{\varepsilon}, \tilde{\mu})\vec{\mathcal{E}}_{||\,n}^{\pm} . \quad (2.31)
$$

The integer n labels the different eigenvalues and eigenvectors for forward ($+$ sign) or backward ($-$ sign) propagation and decay. Owing to the peculiar form of the eigenvalue problem, $\lambda_n^- = -\lambda_n^+$ and $\vec{\mathcal{E}}_{||\,n}^+ = \vec{\mathcal{E}}_{||\,n}^-$. Hence, it is convenient to introduce a single diagonal eigenvalue matrix Λ with diagonal elements λ_n^+ and to summarize the corresponding eigenvectors as columns in a matrix $\mathcal{E}_{||}$.

In a next step, we can construct the Fourier representation of the magnetic field as

$$
\mathcal{H}_{||}^{\pm} = \pm\mathcal{H}_{||}, \qquad \mathcal{H}_{||} = \hat{\mathcal{L}}(\tilde{\varepsilon}, \tilde{\mu})\mathcal{E}_{||}\Lambda^{-1} . \quad (2.32)
$$

Hence, the material matrix $\mathcal{F}_{||}$ exhibits a simplified form:

$$
\mathcal{F}_{||\,\text{simple}} = \begin{pmatrix} \mathcal{E}_{||} & \mathcal{E}_{||} \\ \mathcal{H}_{||} & -\mathcal{H}_{||} \end{pmatrix} . \quad (2.33)
$$

Care has to be taken in the special case that an eigenvalue equals zero. Then, we cannot construct the corresponding magnetic field via equation (2.32), because we would have to divide by zero. Instead, we have to consult equation (2.27), where it is obvious that we can choose the electric and magnetic field independently for $\hat{\mathcal{N}} = 0$ and $\lambda_0 = 0$. In this case, the magnetic field can be constructed as an element of the kernel of $\hat{\mathcal{L}}(\tilde{\mu}, \tilde{\varepsilon})$.

Note that we can consider instead of equation (2.31) also an equivalent problem for the magnetic field [70]. To the best of our knowledge, there is no significant advantage for one or the other. If possible, it is however recommended to solve one of these equations instead of equation (2.27), because the calculation time for an $N \times N$ eigenvalue problem grows with N^3. In addition, we can use group theoretic approaches in order to benefit from specific symmetry properties of the structure of interest, and, thus, solve the eigenvalue equation (2.27) or (2.31) very efficiently [87–91]. However, we have not implemented this approach in our code yet. Therefore, we refrain from a detailed discussion on this topic.

2.3.4 Homogeneous layers

As long as we consider uniform coordinate transformations with $\partial \bar{x}^\alpha / \partial x^\beta =$ constant – such as the inclination defined by equations (2.1a) to (2.1c) – we can find the solution of homogeneous layers analytically. Homogeneous layers are uniform and isotropic with respect to the orthonormal coordinate system $O\bar{x}^1\bar{x}^2\bar{x}^3$:

$$\bar{\varepsilon}^{\alpha\beta} = \varepsilon\delta^{\alpha\beta}\,, \qquad\qquad\qquad \varepsilon = \text{constant}\,, \qquad\qquad (2.34)$$

$$\bar{\mu}^{\alpha\beta} = \mu\delta^{\alpha\beta}\,, \qquad\qquad\qquad \mu = \text{constant}\,. \qquad\qquad (2.35)$$

Due to the fact that all metric terms g, $g_{\alpha\beta}$, and $g^{\alpha\beta}$ are constant, the Fourier transform of the redefined tensors $\varepsilon^{\alpha\beta}$ and $\mu^{\alpha\beta}$ [see equation (2.6)] is trivial, independently on the application of the different Fourier factorizations described later in section 2.5. Thus, we find for the expressions $\tilde{\varepsilon}$ and $\tilde{\mu}$ in equation (2.22):

$$\tilde{f}^{\alpha\beta}_{mn,pq} = \delta_{mp}\delta_{nq}\tilde{g}^{\alpha\beta} \times \begin{cases} f^{-1} & \text{for } \alpha = \beta = 3\,, \\ 1 & \text{for } \alpha = 3 \veebar \beta = 3\,, \\ f & \text{otherwise}\,. \end{cases} \qquad (2.36)$$

In this case, f stands for either ε or μ, and $\veebar$ denotes the exclusive or. The terms $\tilde{g}^{\alpha\beta}$ evolve from the application of the operator $\hat{l}_3^-$ [see definition in equation (2.20)] on the tensor of the conjugate metric components times the square root of the metric determinant, $\sqrt{g}g^{\alpha\beta}$.

Owing to the peculiar diagonal form of the matrices in equation (2.36), the eigenvalue problem defined by equation (2.27) can be split into independent

sub-blocks for the different Fourier harmonics, with

$$\left(\lambda_{mn} + K_{1m}\tilde{g}^{13} + K_{2n}\tilde{g}^{23}\right) \left(\begin{array}{c} E_{1mn} \\ E_{2mn} \end{array} \right) = -L_{mn} \left(\begin{array}{c} H_{1mn} \\ H_{2mn} \end{array} \right) , \tag{2.37}$$

$$\left(\lambda_{mn} + K_{1m}\tilde{g}^{13} + K_{2n}\tilde{g}^{23}\right) \left(\begin{array}{c} H_{1mn} \\ H_{2mn} \end{array} \right) = \frac{\varepsilon}{\mu} L_{mn} \left(\begin{array}{c} E_{1mn} \\ E_{2mn} \end{array} \right) , \tag{2.38}$$

where the 2×2 matrix L_{mn} is defined as

$$L_{mn} = \frac{1}{k_0 \varepsilon} \left(\begin{array}{cc} -k_0^2 \varepsilon \mu \tilde{g}^{21} - K_{1m}\tilde{g}^{33}K_{2n} & -k_0^2 \varepsilon \mu \tilde{g}^{22} + K_{1m}\tilde{g}^{33}K_{1m} \\ k_0^2 \varepsilon \mu \tilde{g}^{11} - K_{2n}\tilde{g}^{33}K_{2n} & k_0^2 \varepsilon \mu \tilde{g}^{12} + K_{2n}\tilde{g}^{33}K_{1m} \end{array} \right) . \tag{2.39}$$

The eigenvalues λ_{mn} of each Fourier harmonic can be derived by the combination of equation (2.37) and (2.38), which yields

$$\left(\lambda_{mn} + K_{1m}\tilde{g}^{13} + K_{2n}\tilde{g}^{23}\right)^2 \left(\begin{array}{c} F_{1mn} \\ F_{2mn} \end{array} \right) = -\frac{\varepsilon}{\mu} L_{mn}^2 \left(\begin{array}{c} F_{1mn} \\ F_{2mn} \end{array} \right) . \tag{2.40}$$

In this case, $F_{\alpha mn}$ denotes either $E_{\alpha mn}$ or $H_{\alpha mn}$. As L_{mn}^2 is diagonal, with

$$-\frac{\varepsilon}{\mu} L_{mn}^2 = \left(\frac{K_{mn}^3}{g^{33}} \right)^2 \left(\begin{array}{cc} 1 & 0 \\ 0 & 1 \end{array} \right) , \tag{2.41}$$

where the terms K_{mn}^3 are defined as

$$K_{mn}^3 = \left\{ g^{33} \left[k_0^2 \varepsilon \mu - (K_{1m})^2 g^{11} - (K_{2n})^2 g^{22} - 2K_{1m}K_{2n}g^{12} \right] \right.$$
$$\left. + \left(K_{1m}g^{13} + K_{2n}g^{23} \right)^2 \right\}^{\frac{1}{2}} , \tag{2.42}$$

we obtain two eigenvalues $\lambda_{mn}^{\pm}$ as the covariant components $K_{3mn}^{\pm}$ of wave vectors $\mathbf{K}_{mn}^{\pm}$, with $\pm K_{mn}^3 = g^{31}K_{1m} + g^{32}K_{2n} + g^{33}K_{3mn}^{\pm}$ [10]:

$$K_{3mn}^{\pm} \equiv \lambda_{mn}^{\pm} = \frac{1}{g^{33}} \left[\pm K_{mn}^3 - \left(K_{1m}g^{13} + K_{2n}g^{23} \right) \right] . \tag{2.43}$$

The corresponding eigenvectors can be chosen as plane waves with the spatial representation

$$E_\alpha^{(\beta,m,n,\pm)}(x^1, x^2, x^3) = e_{\alpha mn}^{\beta\pm} \, e^{iK_{1m}x^1 + iK_{2n}x^2 + iK_{3mn}^{\pm}x^3} , \tag{2.44}$$

where we can distinguish for each pair m, n two solutions of different polarization β, which is defined according to the orientation of the polarization

term $e_{\alpha mn}^{\beta\pm}$ in the $x^1 x^2$ plane. In the simplest case, the lateral components ($\alpha = 1, 2$) are oriented in either direction 1 or 2. Denoting these two solutions by $\beta = 1$ and $\beta = 2$, respectively, we can define the lateral polarization terms as $e_{\alpha mn}^{\beta\pm} = \delta_\alpha^\beta$. Note that we have normalized in this definition the lateral components of the electric field without the loss of generality. The exact contribution of each plane wave in a specific problem depends on the structure of interest as well as the incidence parameters, and will be derived later in section 2.4.

It should be mentioned that we can construct new eigenvectors $E_\alpha^{(\beta,m,n,\pm)}$ for equation (2.40) by any linear combination of eigenvectors with the same eigenvalue. Common alternative sets are the sp basis (see section 2.4.3) or left and right circularly polarized light (see, e.g., [92, 93]). Therefore, the variable β denotes in general a specific basis state of the plane wave defined in equation (2.44), whereas m, n, and $\pm$ can be considered as the quantum numbers of the respective state.

Similar to the general solution of equation (2.27), we define for the homogeneous layers the diagonal matrices $\Lambda_{\text{homo}}^\pm$ with diagonal elements $\lambda_{mn}^\pm$. Furthermore, we assign the values K_{mn}^3 to the diagonal elements of a diagonal matrix Δ, so that the material matrix of the homogeneous layers can be written without the loss of generality as [10]

$$\mathcal{F}_{\parallel\,\text{homo}} = \begin{bmatrix} \mathcal{I} & \mathcal{I} \\ \frac{\varepsilon}{\mu}\hat{\mathcal{L}}(\tilde{\mu}, \tilde{\varepsilon})\Delta^{-1} & -\frac{\varepsilon}{\mu}\hat{\mathcal{L}}(\tilde{\mu}, \tilde{\varepsilon})\Delta^{-1} \end{bmatrix}. \tag{2.45}$$

In this case, $\mathcal{I}$ denotes a unity matrix, whereas $\hat{\mathcal{L}}(\tilde{\mu}, \tilde{\varepsilon})$ contains independent sub-blocks as defined by equation (2.39).

As in section 2.3.3, we have to be careful whenever $K_{mn}^3 = 0$ for some solutions. In such cases, the lateral magnetic field distribution can be chosen as $H_{\alpha pq}^{(\beta,m,n,\pm)} = \pm\delta_p^m \delta_q^n \delta_\alpha^\beta$, with $\alpha, \beta = 1, 2$.

2.4 Scattering matrix formalism

From the general solution of Maxwell's equations inside a layer with translation invariance, we can derive the solution of a stack of layers with identical periodicity and direction of translation invariance in a scattering matrix formalism. Scattering matrices $\mathbb{S}$ provide a relation between the input $|I\rangle$ of a system and the respective output $|O\rangle$ as $|O\rangle = \mathbb{S}|I\rangle$, and are used in many fields of physics [94–96]. In the following, we will show how to construct such a scattering matrix from the solution of equation (2.27) in an iterative procedure (see also schematic in figure 2.3).
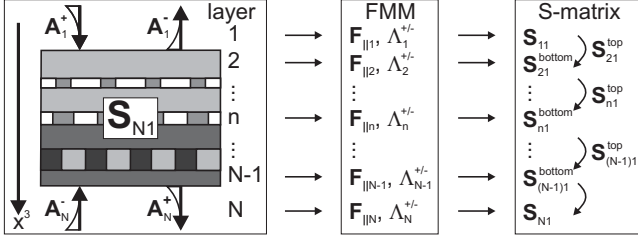
Figure 2.3: Schematic of scattering matrix calculations. The system is separated into several layers with translation invariance along the x^3-axis. Then, a general solution is constructed inside each layer using equation (2.27). Finally, the solutions are combined by considering the vertical boundary conditions in a scattering matrix approach.

For a stack of periodic layers, the input $|I\rangle$ summarizes all waves propagating or decaying towards the top layer 1 and the bottom layer N.[4] The output $|O\rangle$ contains all waves propagating or decaying away from the system. Therefore, the corresponding scattering matrix $\mathbb{S}_{N1}$ is defined as follows:

$$\underbrace{\begin{pmatrix} \vec{\mathbb{A}}_N^+ \\ \vec{\mathbb{A}}_1^- \end{pmatrix}}_{\equiv |O\rangle} = \underbrace{\begin{pmatrix} \mathbb{S}_{N1}^{++} & \mathbb{S}_{NN}^{+-} \\ \mathbb{S}_{11}^{-+} & \mathbb{S}_{1N}^{--} \end{pmatrix}}_{\equiv \mathbb{S}_{N1}} \underbrace{\begin{pmatrix} \vec{\mathbb{A}}_1^+ \\ \vec{\mathbb{A}}_N^- \end{pmatrix}}_{\equiv |I\rangle} . \tag{2.46}$$

The construction of $\mathbb{S}_{N1}$ is not unique. A detailed discussion on this topic can be found in reference [97]. In this work, we present the instructive method using a propagation matrix $\mathbb{P}$ inside a layer and an interface transfer matrix $\mathbb{T}$ for the connection of neighboring layers, which turns out to be also very efficient in the case that the material matrix $\mathcal{F}_\parallel$ of equation (2.29) exhibits specific symmetry properties [97].

2.4.1 Propagation and interface transfer matrices

Inside a layer n, the propagation matrix $\mathbb{P}_n(L)$ provides solutions at positions $x^3 = x_0^3 + L$ when knowing the solutions at $x^3 = x_0^3$:

$$\begin{bmatrix} \vec{\mathbb{A}}_n^+(x_0^3 + L) \\ \vec{\mathbb{A}}_n^-(x_0^3 + L) \end{bmatrix} = \underbrace{\begin{bmatrix} \exp(i\Lambda_n^+ L) & 0 \\ 0 & \exp(i\Lambda_n^- L) \end{bmatrix}}_{\equiv \mathbb{P}_n(L)} \begin{bmatrix} \vec{\mathbb{A}}_n^+(x_0^3) \\ \vec{\mathbb{A}}_n^-(x_0^3) \end{bmatrix} . \tag{2.47}$$

---

[4]Note that the top layer is located at smaller values x^3 than the bottom layer due to the orientation of the x^3 axis defined in figure 2.2.

When passing an interface at position x_0^3 between layers $n-1$ and n, we can relate the amplitude vectors $\vec{\mathbb{A}}_{n-1}^{\pm}(x_0^3 - \delta)$ and $\vec{\mathbb{A}}_n^{\pm}(x_0^3 + \delta)$ for $\delta \to 0$ by the interface transfer matrix $\mathbb{T}_{n(n-1)}$:

$$
\left[
\begin{array}{c}
\vec{\mathbb{A}}_{n-1}^{+}(x_0^3 - \delta) \\
\vec{\mathbb{A}}_{n-1}^{-}(x_0^3 - \delta)
\end{array}
\right]
=
\underbrace{
\left[
\begin{array}{cc}
\mathbb{T}_{n(n-1)}^{++} & \mathbb{T}_{n(n-1)}^{+-} \\
\mathbb{T}_{n(n-1)}^{-+} & \mathbb{T}_{n(n-1)}^{--}
\end{array}
\right]
}_{\equiv \mathbb{T}_{n(n-1)}}
\left[
\begin{array}{c}
\vec{\mathbb{A}}_n^{+}(x_0^3 + \delta) \\
\vec{\mathbb{A}}_n^{-}(x_0^3 + \delta)
\end{array}
\right] . \qquad (2.48)
$$

Its elements can be derived by the material matrices $\mathcal{F}_{\| n-1}$ and $\mathcal{F}_{\| n}$ as well as the continuity condition for the lateral field components $\vec{\mathcal{E}}_{\|}$ and $\vec{\mathcal{H}}_{\|}$ [92]. From equation (2.29), we obtain:

$$
\underbrace{
\left(
\begin{array}{cc}
\mathcal{E}_{\| n-1}^{+} & \mathcal{E}_{\| n-1}^{-} \\
\mathcal{H}_{\| n-1}^{+} & \mathcal{H}_{\| n-1}^{-}
\end{array}
\right)
}_{\equiv \mathcal{F}_{\| n-1}}
\left(
\begin{array}{c}
\vec{\mathbb{A}}_{n-1}^{+} \\
\vec{\mathbb{A}}_{n-1}^{-}
\end{array}
\right)
=
\underbrace{
\left(
\begin{array}{cc}
\mathcal{E}_{\| n}^{+} & \mathcal{E}_{\| n}^{-} \\
\mathcal{H}_{\| n}^{+} & \mathcal{H}_{\| n}^{-}
\end{array}
\right)
}_{\equiv \mathcal{F}_{\| n}}
\left(
\begin{array}{c}
\vec{\mathbb{A}}_n^{+} \\
\vec{\mathbb{A}}_n^{-}
\end{array}
\right) . \qquad (2.49)
$$

Hence,

$$
\mathbb{T}_{n(n-1)} = \mathcal{F}_{\| n-1}^{-1} \mathcal{F}_{\| n} . \qquad (2.50)
$$

Equation (2.50) simplifies in the case of the permittivity and permeability tensors described in section 2.3.3. Owing to the special form of $\mathcal{F}_{\| \text{simple}}$ derived in equation (2.33) [71],

$$
\mathbb{T}_{n(n-1)}^{\text{simple}} = \frac{1}{2}
\left(
\begin{array}{cc}
\mathcal{E}_{\| n-1}^{-1}\mathcal{E}_{\| n} + \mathcal{H}_{\| n-1}^{-1}\mathcal{H}_{\| n} & \mathcal{E}_{\| n-1}^{-1}\mathcal{E}_{\| n} - \mathcal{H}_{\| n-1}^{-1}\mathcal{H}_{\| n} \\
\mathcal{E}_{\| n-1}^{-1}\mathcal{E}_{\| n} - \mathcal{H}_{\| n-1}^{-1}\mathcal{H}_{\| n} & \mathcal{E}_{\| n-1}^{-1}\mathcal{E}_{\| n} + \mathcal{H}_{\| n-1}^{-1}\mathcal{H}_{\| n}
\end{array}
\right) . \qquad (2.51)
$$

2.4.2 Derivation of the scattering matrix

For the scattering matrix iteration, it is convenient to define some non-commutative operations on 2×2 block matrices $\mathbb{X}$ and $\mathbb{Y}$, with

$$
\mathbb{X} =
\left(
\begin{array}{cc}
\mathbb{X}_{11} & \mathbb{X}_{12} \\
\mathbb{X}_{21} & \mathbb{X}_{22}
\end{array}
\right) , \qquad
\mathbb{Y} =
\left(
\begin{array}{cc}
\mathbb{Y}_{11} & \mathbb{Y}_{12} \\
\mathbb{Y}_{21} & \mathbb{Y}_{22}
\end{array}
\right) . \qquad (2.52)
$$

The scattering matrix is calculated in an iterative procedure, where each step consists of either adding a propagation over a distance L_n inside a layer n or passing an interface between two layers $n-1$ and n.

Let $\mathbb{X}$ be either an interface transfer matrix $\mathbb{T}$ or an inverse propagation matrix $\mathbb{P}(-L)$. It is straight-forward to derive an operation $\mathbb{X} * \mathbb{Y}$ with $\mathbb{Y}$ as a scattering matrix that results in a new scattering matrix including the

interface described by $\mathbb{T}$ or an additional propagation over length L in the current layer [62]. In particular,

$$\mathbb{X} * \mathbb{Y} = \begin{pmatrix} -\mathbb{W}_{11}^{-1}\mathbb{Y}_{11} & -\mathbb{W}_{11}^{-1}\mathbb{W}_{12} \\ \mathbb{Y}_{21} - \mathbb{Y}_{22}\mathbb{X}_{21}\mathbb{W}_{11}^{-1}\mathbb{Y}_{11} & \mathbb{Y}_{22}\mathbb{X}_{22} - \mathbb{Y}_{22}\mathbb{X}_{21}\mathbb{W}_{11}^{-1}\mathbb{W}_{12} \end{pmatrix}, \quad (2.53)$$

with

$$\mathbb{W}_{\alpha\beta} = \mathbb{Y}_{\alpha 2}\mathbb{X}_{2\alpha} - \mathbb{X}_{\alpha\beta}. \quad (2.54)$$

For two scattering matrices $\mathbb{X}$ and $\mathbb{Y}$, we can define the following operation in order to construct the scattering matrix of the combined system with the structure described by $\mathbb{X}$ below[5] the structure described by $\mathbb{Y}$ [71]:

$$\mathbb{X} \star \mathbb{Y} = \begin{bmatrix} \mathbb{X}_{11}\left(\mathbb{I} - \mathbb{Y}_{12}\mathbb{X}_{21}\right)^{-1}\mathbb{Y}_{11} & \mathbb{X}_{12} + \mathbb{X}_{11}\left(\mathbb{I} - \mathbb{Y}_{12}\mathbb{X}_{21}\right)^{-1}\mathbb{Y}_{12}\mathbb{X}_{22} \\ \mathbb{Y}_{21} + \mathbb{Y}_{22}\left(\mathbb{I} - \mathbb{X}_{21}\mathbb{Y}_{12}\right)^{-1}\mathbb{X}_{21}\mathbb{Y}_{11} & \mathbb{Y}_{22}\left(\mathbb{I} - \mathbb{X}_{21}\mathbb{Y}_{12}\right)^{-1}\mathbb{X}_{22} \end{bmatrix}. \quad (2.55)$$

Here, $\mathbb{I}$ denotes the identity matrix of dimensions equal to the blocks of $\mathbb{X}$ and $\mathbb{Y}$.

With the operators defined by equations (2.53) and (2.55), it is possible to write the scattering matrix iteration in an elegant way. The scattering matrix iteration is initialized by an identity matrix $\mathbb{S}_{11}$. Knowing the scattering matrix $\mathbb{S}_{(n-1)1}^{\text{bottom}}$ on the bottom of layer $n-1$, we can construct the scattering matrix $\mathbb{S}_{n1}^{\text{bottom}}$ on the bottom of layer n as follows:

$$\mathbb{S}_{n1}^{\text{bottom}} = \mathbb{P}_n(-L_n) * \underbrace{\mathbb{T}_{n(n-1)} * \mathbb{S}_{(n-1)1}^{\text{bottom}}}_{=\mathbb{S}_{n1}^{\text{top}}}. \quad (2.56)$$

Here, L_n denotes the propagation length inside layer n along the x^3 axis.

In a typical scattering matrix calculation, we set the propagation length in the top and bottom layer to zero, because we assume these layers to be infinite half spaces, where the Fourier-Bloch modes are either damped or propagate to the far field. With these simplifications, the scattering matrix $\mathbb{S}_{N1}$ of a stacked system from layer 1 to layer N can be derived as

$$\mathbb{S}_{N1} = \mathbb{T}_{N(N-1)} * \mathbb{P}_{N-1}(-L_{N-1}) * \mathbb{T}_{(N-1)(N-2)} * \ldots * \mathbb{T}_{32} * \mathbb{P}_2(-L_2) * \mathbb{T}_{21} * \mathbb{S}_{11}. \quad (2.57)$$

Alternatively, we can combine two scattering matrices $\mathbb{S}_{NM}$ and $\mathbb{S}_{M1}$ by equation (2.55):

$$\mathbb{S}_{N1} = \mathbb{S}_{NM} \star \mathbb{S}_{M1}. \quad (2.58)$$

---

[5] For the orientation of the x^3 axis defined in figure 2.2, a system is below another system if it is located at larger x^3.

In principle, any combination of equation (2.57) and (2.58) is possible and it depends on the application, which scheme is preferable [97].

The combination of scattering matrices as described by equation (2.58) is definitely superior in cases where a lot of similar problems have to be calculated that differ only by the propagation length in a specific layer M. Then, we can calculate the scattering matrices $\mathbb{S}_{M1}^{\text{top}}$ and $\mathbb{S}_{NM}$ once and derive the combined scattering matrix for various propagation lengths L_M as follows[76]:

$$\mathbb{S}_{N1}(L_M) = \mathbb{S}_{NM} \star \left[\mathbb{P}_M(-L_M) * \mathbb{S}_{M1}^{\text{top}} \right] \,. \tag{2.59}$$

2.4.3 Small scattering matrix

In the previous sections, the scattering matrix was assumed to be either infinitely large or – in the case of truncation – of size $4N_G \times 4N_G$ with N_G as the total amount of Fourier-Bloch modes. Among the Fourier-Bloch modes of the top layer 1 and bottom layer N, only a few contribute to the far field spectra. We denote these modes as open far field channels. The condition for a propagation into the far field is a purely real eigenvalue λ_n in equation (2.27). Therefore, we can truncate the final scattering matrix $\mathbb{S}_{N1}$ further when interested in the far field spectra, because all modes with a nonzero imaginary part of λ_n are damped down in the infinite half spaces on top and on bottom [98, 99].[6]

We assume in this section that the top and bottom layers are homogeneous, with far field channels corresponding to plane waves as defined by equation (2.44). Note that this is not necessarily the case in situations where some eigenvalues of equation (2.27) are degenerate in the top or bottom layer. Furthermore, the lateral electric field components of the open far field channels are supposed to obey for $\alpha, \beta = 1, 2$:[7]

$$E_\alpha^{(\beta,m,n,\pm)}(x^1, x^2, x^3) = \delta_\alpha^\beta \exp(iK_{1m}x^1 + iK_{2n}x^2 + iK_{3mn}^\pm x^3) \,. \tag{2.60}$$

When considering a small scattering matrix containing only open far field channels, it is convenient to carry out a normalization and rotation such that the elements of this so-called small scattering matrix $\mathbb{S}^R$ correspond to reflection and transmission coefficients of the different input and output diffraction

---

[6] It should be kept in mind that such a truncation to propagating channels cannot be carried out in the internal layers 2 to $N-1$, because we cannot neglect the decaying modes in general.

[7] Note that we consider in this case a coordinate system $Ox^1x^2x^3$ that is uniform. In the next chapters of this thesis, we refrain from this restriction so that the occurring fields have to be converted from the non-uniform coordinate system to a uniform coordinate system in order to apply the equations derived in this section.

orders in s (from German *senkrecht* = perpendicular) and p (parallel) polarization [98]:

$$\mathbb{S}_{N1}^{\mathrm{R}} = \begin{pmatrix} r_{11}^{\mathrm{pp}} & r_{11}^{\mathrm{ps}} & t_{1N}^{\mathrm{pp}} & t_{1N}^{\mathrm{ps}} \\ r_{11}^{\mathrm{sp}} & r_{11}^{\mathrm{ss}} & t_{1N}^{\mathrm{sp}} & t_{1N}^{\mathrm{ss}} \\ t_{N1}^{\mathrm{pp}} & t_{N1}^{\mathrm{ps}} & r_{NN}^{\mathrm{pp}} & r_{NN}^{\mathrm{ps}} \\ t_{N1}^{\mathrm{sp}} & t_{N1}^{\mathrm{ss}} & r_{NN}^{\mathrm{sp}} & r_{NN}^{\mathrm{ss}} \end{pmatrix}. \tag{2.61}$$

Here, $r_{11}^{\beta\beta'}$ and $t_{N1}^{\beta\beta'}$ denote general reflection and transmission coefficients for all open channels with β' polarized input from the top layer and β polarized output, where β and β' stand for either s or p. Similarly, $r_{NN}^{\beta\beta'}$ and $t_{1N}^{\beta\beta'}$ indicate the reflection and transmission coefficients for bottom input.

Note that s and p polarization are defined to be such that the electric field vibrates either perpendicular or parallel to the plane defined by the $\overline{x}^3$ axis as the normal of the planar layers and the wave vector $\mathbf{K}_{mn}^{\pm}$ with components K_{1m}, K_{2n}, and $K_{3mn}^{\pm}$. If m and n specify the input channel for a plane wave incidence, the latter plane equals the incidence plane (see figure 2.2). Alternative notations for s and p are transverse electric (TE) and transverse magnetic (TM) orientation.

It should be mentioned that our definition of s and p is relative to the diffraction orders defined by the integers m and n. Thus, it is not necessary to fix the input channel of the small scattering matrix to $m = 0$ and $n = 0$. Furthermore, the orientation of s and p changes in dependence on the component $K_{3mn}^{\pm}$, which allows to treat incidence from the top or the bottom layer in the same way. For this purpose, we additionally choose the sp basis such that the vectors $\mathbf{E}_{mn}^{\mathrm{p}\pm}$, $\mathbf{E}_{mn}^{\mathrm{s}\pm}$, and $\mathbf{K}_{mn}^{\pm}$ form a right handed system in that order. This definition has the advantage that it corresponds one by one to the experimental measurements, where the light beam is supposed to be defined with respect to its source, which is either the sample in the case of reflection, transmission, and diffraction measurements, or the illuminating light. However, care has to be taken when constructing secondary quantities such as left or right circularly polarized light as well as Stokes parameters [93] and the related Jones and Jones-Mueller matrices [100] from this sp basis (for further information, see also section 2.4.4). A detailed discussion on the problem is beyond the scope of this work, and we refer to well-known text books such as [92, 93].

Denoting $\beta = \mathrm{s}, \mathrm{p}$ for s or p polarized light, the polarization terms $e_{\alpha mn}^{\beta\pm}$ of

the plane wave expansion [see equation (2.44)] obey:

$$e_{1mn}^{\mathrm{p}\pm} = \frac{\pm 1}{N_{mn}^{\mathrm{p}\pm}} K_{mn}^3 K_{1m}, \qquad\qquad e_{1mn}^{\mathrm{s}\pm} = \frac{1}{N_{mn}^{\mathrm{s}\pm}} \left(\pm K_{mn}^3 g^{32} - K_n^2 g^{33} \right), \quad (2.62\mathrm{a})$$

$$e_{2mn}^{\mathrm{p}\pm} = \frac{\pm 1}{N_{mn}^{\mathrm{p}\pm}} K_{mn}^3 K_{2n}, \qquad\qquad e_{2mn}^{\mathrm{s}\pm} = \frac{1}{N_{mn}^{\mathrm{s}\pm}} \left(K_m^1 g^{33} \mp K_{mn}^3 g^{31} \right), \quad (2.62\mathrm{b})$$

$$e_{3mn}^{\mathrm{p}\pm} = \frac{-1}{N_{mn}^{\mathrm{p}\pm}} \left(K_m^1 K_{1m} + K_n^2 K_{2m} \right), \quad e_{3mn}^{\mathrm{s}\pm} = \frac{1}{N_{mn}^{\mathrm{s}\pm}} \left(K_m^1 g^{32} - K_n^2 g^{31} \right). \quad (2.62\mathrm{c})$$

The scalars $N_{mn}^{\mathrm{p}\pm}$ and $N_{mn}^{\mathrm{s}\pm}$ define the normalization of the fields to a constant component S^3 of the Poynting vector $\mathbf{S}$ in order to preserve the power flux through the $x^1 x^2$ plane for lossless media [99]:

$$|S_{mn}^{3\pm}| = \frac{c}{8\pi} e_{mn}^{\alpha\pm} e_{\alpha mn}^{\pm} \frac{K_{mn}^3}{\mu k_0} = \text{constant}. \qquad (2.63)$$

Note that we assume K_{mn}^3 to be real, because we are interested in open far field channels. As a valid normalization, we have chosen $|S_{mn}^{3\pm}| = c/8\pi$. Thus,

$$N_{mn}^{\mathrm{p}\pm} = \sqrt{k_0 \varepsilon K_{mn}^3} \left[g^{33} \left(K_m^1 K_{1m} + K_n^2 K_{2n} \right) \mp K_{mn}^3 \left(K_{1m} g^{13} + K_{2n} g^{23} \right) \right]^{\frac{1}{2}},$$

$$(2.64\mathrm{a})$$

$$N_{mn}^{\mathrm{s}\pm} = \sqrt{\frac{K_{mn}^3}{g k_0 \mu}} \left[g^{33} \left(K_m^1 K_{1m} + K_n^2 K_{2n} \right) \mp K_{mn}^3 \left(K_{1m} g^{13} + K_{2n} g^{23} \right) \right]^{\frac{1}{2}}.$$

$$(2.64\mathrm{b})$$

Equations (2.62a) to (2.62c) result by straight-forward calculus from the divergence condition of homogeneous layers with

$$K_m^1 e_{1mn}^{\beta\pm} + K_n^2 e_{2mn}^{\beta\pm} \pm K_{mn}^3 e_{3mn}^{\beta\pm} = 0, \qquad (2.65)$$

and the conditions $e_{mn}^{3\pm} = 0$ for s polarized fields as well as $e_{1mn}^{\mathrm{p}\pm} = c_{mn}^{\pm} K_{1m}$ and $e_{2mn}^{\mathrm{p}\pm} = c_{mn}^{\pm} K_{2n}$ with constant $c_{mn}^{\pm}$ for p polarized light. Note that there exists an ambiguity in the definition of s and p polarization whenever $K_{1m} = K_{2n} = 0$ for some diffraction orders. In such cases, we define p polarized light by an electric field parallel to the $\bar{x}^1 \bar{x}^3$ plane and s polarized light by the corresponding orthogonal polarization.

Defining diagonal matrices $\mathcal{E}_\alpha^{\mathrm{s}\pm}$ and $\mathcal{E}_\alpha^{\mathrm{p}\pm}$ with the diagonal components $e_{\alpha mn}^{\mathrm{s}\pm}$ and $e_{\alpha mn}^{\mathrm{p}\pm}$, respectively, we obtain the following transformation matrices $\mathbb{U}^{\pm}$ from a sp basis to the standard basis $e_{\alpha mn}^{\beta\pm} = \delta_\alpha^\beta$ with $\alpha, \beta = 1, 2$:

$$\mathbb{U}^{\pm} = \begin{pmatrix} \mathcal{E}_1^{\mathrm{p}\pm} & \mathcal{E}_1^{\mathrm{s}\pm} \\ \mathcal{E}_2^{\mathrm{p}\pm} & \mathcal{E}_2^{\mathrm{s}\pm} \end{pmatrix}. \qquad (2.66)$$

Hence, the small scattering matrix can be constructed via the restriction to open channels as

$$
\mathbb{S}_{N1}^{\mathrm{R}} = \left[\begin{array}{cc} 0 & \left(\mathbb{U}_1^-\right)^{-1} \\ \left(\mathbb{U}_N^+\right)^{-1} & 0 \end{array} \right]_{\mathrm{open}} \left(\begin{array}{cc} \mathbb{S}_{N1}^{++} & \mathbb{S}_{N1}^{+-} \\ \mathbb{S}_{N1}^{-+} & \mathbb{S}_{N1}^{--} \end{array} \right)_{\mathrm{open}} \left(\begin{array}{cc} \mathbb{U}_1^+ & 0 \\ 0 & \mathbb{U}_N^- \end{array} \right)_{\mathrm{open}} , \quad (2.67)
$$

where the subscripts 1 and N indicate that the transformation matrix originates from the eigenvalue equation in the top and bottom layer, respectively.

Note that other authors may consider a slightly different normalization [98, 101]. However, the presented normalization leads to simplified symmetry properties of the small scattering matrix. For instance, $\mathbb{S}_{N1}^{\mathrm{R}}$ is unitary in the case that all layers consist of lossless materials.

2.4.4 Jones matrix, Mueller matrix, and polarization ellipse

In many practical applications, people are used to describing the optical properties of a system by different concepts than the scattering matrix formalism. In this section, we will present the connection between the small scattering matrix and the Jones and Mueller matrices. In addition, we are going to show how to derive the polarization ellipse from the outgoing sp basis of the small scattering matrix.

Jones matrix

In the small scattering matrix, we describe the incoming and outgoing waves in terms of a sp basis. If we restrict ourselves to only one incoming and one outgoing diffraction order in either reflection or transmission, the corresponding matrix elements of the small scattering matrix set up a 2×2 matrix that can be understood as a Jones matrix J. Thus, we can benefit from the established Jones calculus for the description of linear optical elements such as linear and circular polarizers, as long as we can neglect any interaction between these elements and the structure described by the scattering matrix.

In the Jones calculus [102], the light is described by two orthogonal polarizations – usually s and p, and any optical elements in an experimental setup can be translated into a so-called Jones matrix J_n. It is generally assumed that the optical elements do not interact with each other. Therefore, we can derive the relation between incoming and outgoing light by a product of the different Jones matrices as

$$
\left(\begin{array}{c} E_{\mathrm{p}} \\ E_{\mathrm{s}} \end{array} \right)_{\mathrm{out}} = \underbrace{\prod_n J_n}_{\equiv J_{\mathrm{tot}}} \left(\begin{array}{c} E_{\mathrm{p}} \\ E_{\mathrm{s}} \end{array} \right)_{\mathrm{in}} . \quad (2.68)
$$

Polarization ellipse

So far, we have neglected the time dependence in Maxwell's equations. In this section, we would like to remind the reader that the physical solution corresponding to a plane wave with complex components E_p and E_s has to be constructed by taking the real part of $E_p \exp(-i\omega t)$ and $E_s \exp(-i\omega t)$, respectively. For these real quantities, the sp basis defines the plane of vibration for the electric field. Depending on the phase relation between E_p and E_s, the electric field vector can be characterized as linearly polarized, circularly polarized, or elliptically polarized [93].

Let us define φ as the relative phase between s and p polarization. Linearly polarized light corresponds to $\varphi = 0$, so that the electric field vector vibrates along a line in the plane of vibration. In the case of circularly polarized light, the trajectory of the tip of the electric field vector describes a circle in the plane of vibration, which requires $|E_p| = |E_s|$ and $\varphi = \pm\pi/2$. The most general case is that of an elliptically polarized light with arbitrary E_s, E_p, and φ. In this case, the tip of the electric field vector rotates on an ellipse in the plane of vibration, which is called polarization ellipse.

In general, the directions defined by s and p do not coincide with the long and short semi-axes of the polarization ellipse. Let us denote the long and short semi-axes by a and b, respectively. The angle between the direction of the p polarized light and the large semi-axis shall be defined as Ψ. We find for the polarization ellipse [93]:

$$a = \sqrt{\frac{1}{2}\left(|E_p|^2 + |E_s|^2 + |L|\right)}, \quad b = \sqrt{\frac{1}{2}\left(|E_p|^2 + |E_s|^2 - |L|\right)}, \quad \Psi = \frac{1}{2}\arg(L).$$

$$(2.69)$$

In this case,

$$L = |E_p|^2 - |E_s|^2 + 2i\Re(E_p E_s^*). \qquad (2.70)$$

Stokes vector and Mueller matrix

The Jones calculus as well as the polarization ellipse are quantities that describe polarized light. However, in many cases, light is incoherent and randomly polarized. A general description of such unpolarized light can be achieved by the Stokes vector $\vec{S}$ with components S_0, S_1, S_2, and S_3. The first component S_0 defines the total intensity of the light; the components S_1, S_2, and S_3 characterize the polarization state.

A positive or negative component S_1 corresponds to p or s polarized contributions, respectively. Component S_2 specifies linear polarization along an axis that is rotated by 45° with respect to s and p polarization; component S_3 indicates the left and right circularly polarized contribution. In general,

$S_0^2 \geq S_1^2 + S_2^2 + S_3^2$, with the equality sign denoting fully polarized light. In this case, we find for the Stokes vector [92]:

$$S_0 = |E_p|^2 + |E_s|^2\,, \quad S_1 = |E_p|^2 - |E_s|^2\,, \quad S_2 = 2\Re(E_p E_s^*)\,, \quad S_3 = 2\Im(E_p E_s^*)\,. \tag{2.71}$$

Especially for ellipsometry measurements, the description via Stokes vectors is quite common. Similar to the Jones calculus, the relation between incoming and outgoing Stokes vectors can be written in a matrix notation as

$$\vec{S}_{\text{out}} = M\vec{S}_{\text{in}}\,, \tag{2.72}$$

where M denotes the so-called Mueller matrix. In contrast to the Jones calculus, the Mueller calculus can treat also unpolarized light. However, in this work, we are interested in fully polarized light only, for which it is sufficient to consider the subclass of the so-called Jones-Mueller matrices. The relation between a Jones matrix J and the corresponding Jones-Mueller matrix M is as follows [100]:

$$M = U^\dagger \left(J \otimes J^*\right) U\,. \tag{2.73}$$

In this case, $\otimes$ denotes the Kronecker product, and

$$U = \frac{1}{\sqrt{2}} \begin{pmatrix} 1 & 1 & 0 & 0 \\ 0 & 0 & 1 & -i \\ 0 & 0 & 1 & i \\ 1 & -1 & 0 & 0 \end{pmatrix}\,. \tag{2.74}$$

2.5 Factorization rules

As mentioned above in section (2.3.2), the straight-forward computation of matrix elements for products in Fourier space [see equation (2.19)] does not converge very fast under certain circumstances. In 1996, Li investigated this problem and formulated some rules for an optimized convergence [74], which are proven in reference [69]. We are going to discuss in this section the factorization rules of Li briefly and provide their general application to Maxwell's equations.

2.5.1 Products in Fourier space

For the sake of simplicity, let us merely consider now one-dimensional functions $f(x)$, $g(x)$, and $h(x)$. Their Fourier transforms shall be denoted by Fourier coefficients f_n, g_n, and h_n. If we are interested in the product $f(x) = g(x) \cdot h(x)$, it transforms in Fourier space into a convolution:

$$f(x) = g(x) \cdot h(x) \quad \Rightarrow \quad f_m = \sum_n g_{m-n} h_n\,. \tag{2.75}$$

The multiplication rule for constructing the Fourier coefficients of the product function, as written on the right side of equation (2.75), is usually referred to as Laurent's rule.

It is well-known that the truncated Fourier expansion of discontinuous functions exhibits a hampered convergence due to the Gibbs phenomenon [103], which is manifested in over- and undershoots close to the jump discontinuity (see dashed line in figure 2.4a). The influence of this phenomenon becomes worse when carrying out the product of two functions with concurrent jump discontinuities in a truncated convolution as defined by equation (2.75). For instance, the dashed line figure 2.4b denotes the spatial representation of the convolution $\sum_n g_{m-n} h_n$, with $g(x) = 1/h(x)$, $h(x) = 1 + \Theta(x - 0.4)\Theta(0.6 - x)$ in the interval $[0, 1]$, and $\Theta(x)$ as the Heaviside function. Evidently, the result of Laurent's rule exhibits a large deviation at the concurrent jump discontinuities, even though the product should be continuous. For this special case of a continuous product, Li formulated the so-called inverse rule, so that we can distinguish the following two different constructions of matrices for products in Fourier space:

$$\text{normal rule: } \vec{f} = [g]\vec{h}, \quad \text{inverse rule: } \vec{f} = [g^{-1}]^{-1}\vec{h}. \quad (2.76)$$

Here, $\vec{f}$ and $\vec{h}$ denote column vectors with a size equal to the truncation order, whereas $[g]$ and $[g^{-1}]$ represent square matrices derived by Laurent's rule from the functions $g(x)$ and $g^{-1}(x)$, respectively. Using the inverse rule in the example of figure 2.4b (diamonds) results in a perfect convergence for the used truncation order of 32 harmonics.

For the general definition of the factorizations rules, let us define $\{x_f\}$, $\{x_g\}$, and $\{x_h\}$ as the locations of jump discontinuities of function $f(x)$, $g(x)$, and $h(x)$, respectively. The factorization rules state [74]:

1. In the case that $g(x)$ and $h(x)$ have no concurrent jump discontinuities so that $\{x_g\} \cap \{x_h\} = \{\}$, the product $f(x) = g(x) \cdot h(x)$ should be constructed in Fourier space by the Laurent's rule.

2. If $g(x)$ and $h(x)$ have concurrent jump discontinuities such that $f(x)$ is continuous at these points with $\{x_g\} \cap \{x_h\} \notin \{x_f\}$, the best convergence of the product $f(x) = g(x) \cdot h(x)$ can be achieved in Fourier space by the inverse rule.

3. Whenever $g(x)$ and $h(x)$ have at least one concurrent jump discontinuity for which $f(x) = g(x) \cdot h(x)$ is discontinuous with $\{x_f\} \cap \{x_g\} \neq \{\}$ or $\{x_f\} \cap \{x_h\} \neq \{\}$, neither normal nor inverse rule converge very fast.
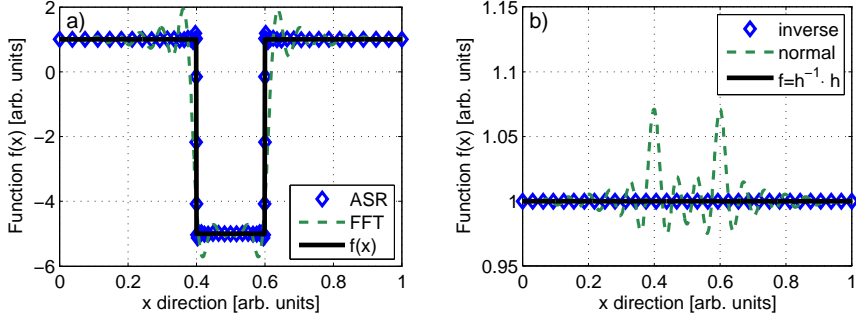
Figure 2.4: (a) Convergence of a truncated Fourier transform with (diamonds) and without (dashed line) adaptive spatial resolution in the case of a discontinuous function f (thick black line). (b) Comparison of the normal and inverse rule in the case of a pair of discontinuous functions $g(x) = 1/h(x)$ and $h(x)$ with $h(x) = 1 + \Theta(x - 0.4)\Theta(0.6 - x)$.

2.5.2 Boundary conditions

The factorization rules are of essential importance for the Fourier modal method, because the master equation (2.27) contains matrices that evolve from the permittivity and permeability tensors $\varepsilon^{\alpha\beta}$ and $\mu^{\alpha\beta}$ with discontinuities at the material interfaces. On the other hand, the products $\varepsilon^{\alpha\beta}E_\beta$ and $\mu^{\alpha\beta}H_\beta$ may be continuous. The conditions for the continuity can be derived by considering the boundary conditions of Maxwell's equations, which is basic text book knowledge in the case of orthonormal coordinate systems $O\overline{x}^1\overline{x}^2\overline{x}^3$ [92].

At any source-free material interfaces, the boundary conditions state that the normal component of the electric displacement and the magnetic induction are conserved. Furthermore, the tangential components of the electric and magnetic field are continuous at these interfaces. Owing to the invariance of the covariant form of Maxwell's equations defined in section 2.3.1, we can directly deduce identical relations for the electric and magnetic field as well as the general displacement and induction in a new coordinate system $Ox^1x^2x^3$.

It should be kept in mind that the covariant components A_α of a vector $\mathbf{A}$ are tangential to both the $x^\alpha x^\beta$ and $x^\alpha x^\gamma$ planes, whereas the contravariant components A^α are normal to the $x^\beta x^\gamma$ plane for $\alpha \neq \beta$, $\beta \neq \gamma$, and $\alpha \neq \gamma$ (see discussion in section 3.1). Hence, it is trivial to identify normal and tangential vector components at material interfaces in the case that all interface normals are collinear to one of the coordinate axes x^1, x^2, and x^3 of the underlying coordinate system [10]. Thus, we find that E_α and H_α are continuous at any

source-free interfaces parallel to the $x^\alpha x^\beta$ planes, whereas both D^α and B^α are conserved in the general coordinate system $Ox^1 x^2 x^3$ when passing an interface parallel to the $x^\beta x^\gamma$ plane with $\alpha \neq \beta$ and $\alpha \neq \gamma$. We will henceforth assume such a peculiar configuration, as it simplifies the correct application of the factorization rules to Maxwell's equations tremendously.

2.5.3 Application to Maxwell's equations

The Fourier factorization rules state that we must not apply the Laurent's rule to the product of functions with concurrent jump discontinuities but continuous product. The derivation of the correct application to Maxwell's equations is rather lengthy and not unique [10, 11], but the final results can be summarized effectively by the operators $\hat{l}_\gamma^\pm$ defined in equation (2.20). Let $\hat{F}_\alpha$ be an operator that creates the matrices for products in Fourier space from the Fourier transform in direction x^α by using Laurent's rule. Thus, we can derive the following equivalent forms of correct Fourier factorization [10]:

$$\hat{f} = \underbrace{\hat{l}_2^+ \hat{F}_2 \hat{l}_2^-}_{\equiv \hat{L}_2} \underbrace{\hat{l}_1^+ \hat{F}_1 \hat{l}_1^-}_{\equiv \hat{L}_1} (f) \,, \qquad \hat{f} = \underbrace{\hat{l}_1^+ \hat{F}_1 \hat{l}_1^-}_{\equiv \hat{L}_1} \underbrace{\hat{l}_2^+ \hat{F}_2 \hat{l}_2^-}_{\equiv \hat{L}_2} (f) \,. \qquad (2.77)$$

Here, f represents either the permittivity or the permeability tensor defined in equation (2.6). The corresponding output $\hat{\varepsilon}$ and $\hat{\mu}$ should then be inserted in equation (2.21) for a convincing convergence behavior of the numerical solution for equation (2.27).

As mentioned by Li, the tensors defined by equation (2.77) exhibit an asymmetry in the case that the structure of interest is symmetric in the lateral directions [10]. Instead, he suggests considering a mean value of both operators at the cost of a violation of the energy conservation in the case of lossless materials.

For the special tensors discussed in section 2.3.3, we suggest as an alternative to the mean value to take the Fourier transformed elements partially from both definitions in equation (2.77) [11]:

$$\hat{f} = \left\{ \begin{array}{ccc} \left[\hat{L}_2 \hat{L}_1(f)\right]^{11} & \left[\hat{L}_2 \hat{L}_1(f)\right]^{12} & 0 \\ \left[\hat{L}_1 \hat{L}_2(f)\right]^{21} & \left[\hat{L}_1 \hat{L}_2(f)\right]^{22} & 0 \\ 0 & 0 & \left[\hat{F}_1 \hat{F}_2(f)\right]^{33} \end{array} \right\} \,. \qquad (2.78)$$

Here, $[\hat{L}_\alpha \hat{L}_\beta(f)]^{\gamma\delta}$ and $[\hat{F}_\alpha \hat{F}_\beta(f)]^{\gamma\delta}$ denote the tensor elements $\hat{f}^{\gamma\delta}$ constructed by one of the schemes in equation (2.77) or the simple Laurent's rule, respectively. Thus, we do not violate the energy conservation, but also have a perfect symmetry in the Fourier transformed tensors.

It is worth mentioning that several papers are devoted to an application of the correct Fourier factorization rules in cases, where the interface normals do not coincide with the coordinate axes [78–80]. These papers refer to the so-called fast Fourier factorization [77], where it is suggested to consider the application of factorization rules by projecting to a normal and a tangent vector with respect to the interfaces and to apply either the inverse or normal rule to the resulting projections.

2.6 Adaptive spatial resolution

Although the correct application of factorization rules improves the convergence of the Fourier modal method tremendously, the Gibbs phenomenon still hampers the convergence of the Fourier transformed discontinuous permittivity and permeability tensors. Especially metals exhibit a slow convergence, so that additional improvements are necessary. Granet suggested in 1999 to apply a coordinate transformation, where the spatial resolution is increased at the material interfaces [12]. In this section, we are going to explain the fundamental principles behind this concept of adaptive spatial resolution (ASR). For further details, the reader may consult chapter 3, where the application of coordinate transformations is described in a more general context.

2.6.1 General concept

The permittivity and permeability tensors defined in equation (2.6) consist of the product of a metric term and the tensor of a orthonormal coordinate system $O\overline{x}^1\overline{x}^2\overline{x}^3 = Oxyz$. Let us consider an isotropic layer with simplified permittivity and permeability distributions $\overline{\varepsilon}^{\alpha\beta} = \varepsilon(x)\delta^{\alpha\beta}$ and $\overline{\mu}^{\alpha\beta} = \mu(x)\delta^{\alpha\beta}$ that are translation invariant in directions y and z and periodic with period L in x. Defining a new coordinate system $Ox^1x^2x^3 = Ouyz$ with $x = x(u) = x(u + L)$, we obtain permittivity and permeability tensors of the form

$$
A = \left\{
\begin{array}{ccc}
\left(\frac{\partial x}{\partial u}\right)^{-1} f[x(u)] & 0 & 0 \\
0 & \frac{\partial x}{\partial u} f[x(u)] & 0 \\
0 & 0 & \frac{\partial x}{\partial u} f[x(u)]
\end{array}
\right\}, \qquad (2.79)
$$

where f represents either the permittivity or permeability distribution ε and μ, respectively.

As the factorization rules dictate that we should use the inverse rule for the element A^{11} and the normal rule for the other diagonal elements A^{22} and A^{33}, we have to carry out the following type of Fourier transforms in the

non-uniform coordinate system $Ouyz$:

$$f_n = \frac{1}{L} \int_0^L \frac{\partial x}{\partial u} f(u) e^{i(k_x + \frac{2\pi}{L} n)u} du \,. \tag{2.80}$$

Hence, the effective jump height at a discontinuity can be reduced if the coordinate transformation is chosen such that $\partial x/\partial u$ is small at the jump discontinuities of $f(u)$. This can be achieved by increasing the spatial resolution at these points. Figure 2.4a illustrates the superior convergence when transforming a discontinuous function f (thick black line) through the concept of adaptive spatial resolution. The standard fast Fourier transform (FFT) is depicted by the dashed line and clearly suffers under the Gibbs phenomenon. For the same truncation order of 32 harmonics, the diamonds indicate the improved description via adaptive spatial resolution by showing the spatial representation of $[\partial x/\partial u]^{-1}\vec{f}$. We have used in that case the one-dimensional coordinate transformation defined in reference [104], where $x(u)$ is constructed between two discontinuities at x_{l-1} and x_l as follows:

$$x_{[u_{l-1}, u_l]}(u) = \frac{u_l x_{l-1} - u_{l-1} x_l}{u_l - u_{l-1}} + \frac{x_l - x_{l-1}}{u_l - u_{l-1}} u$$
$$+ \frac{(1-\eta)(u_l - u_{l-1}) - (x_l - x_{l-1})}{2\pi} \sin\left(2\pi \frac{u - u_{l-1}}{u_l - u_{l-1}}\right) \,. \tag{2.81}$$

The transformation strength is given by the parameter η with $0 \leq \eta \leq 1$, where $\eta = 1$ corresponds to the maximum possible resolution increment with a zero derivative $\partial x/\partial u$ at the interfaces. In figure 2.4a, we use a transformation strength $\eta = 0.99$. Note that the interface positions u_l and u_{l-1} of the transformed coordinate system $Ouyz$ can differ from those in the uniform coordinate system $Oxyz$. Usually, they are chosen such that all intervals $[u_{l-1}, u_l]$ are of equal size.

The concept of adaptive spatial resolution can be easily applied whenever all interface normals are collinear to one of the coordinate axes of the underlying uniform coordinate system. Let us denote such a general uniform coordinate system by coordinates $\tilde{x}^\alpha$. Then, the transformation defined in equation (2.81) can be applied to the coordinates $\tilde{x}^1$ and $\tilde{x}^2$ independently.

In a similar manner, perfectly matched layers can be introduced in the Fourier modal method by using a nonlinear coordinate transformation [83]. Thus, the method is capable of deriving the optical properties of non-periodic structures. Although of general interest, it is beyond the scope of this work to present further details on this topic. An interested reader may consult the provided references [82, 83] and references therein.

2.6.2 Numerical example

Let us illustrate the convergence improvements of adaptive spatial resolution and factorization rules using the example 4 of reference [10]. There, an inclined coordinate system $O\check{x}^1\check{x}^2\check{x}^3$ with $\zeta = 30°$ and $\chi = \xi = 0°$ is introduced. The structure itself consists of a metallic film with $\overline{\varepsilon}_{\mathrm{metal}}^{\alpha\beta} = (1 + 5i)^2\delta^{\alpha\beta}$ and $\overline{\mu}^{\alpha\beta} = \delta^{\alpha\beta}$ with air on top and a quartz substrate with $\overline{\varepsilon}_{\mathrm{sub}}^{\alpha\beta} = 2.25\delta^{\alpha\beta}$. Inside the metal film, there are air holes of side length $1\,\mu$m (see figure 2.5a). The lateral periods are $2\,\mu$m; the incidence parameters are wavelength $1\,\mu$m, $\theta = 30°$, and $\phi = 30°$.
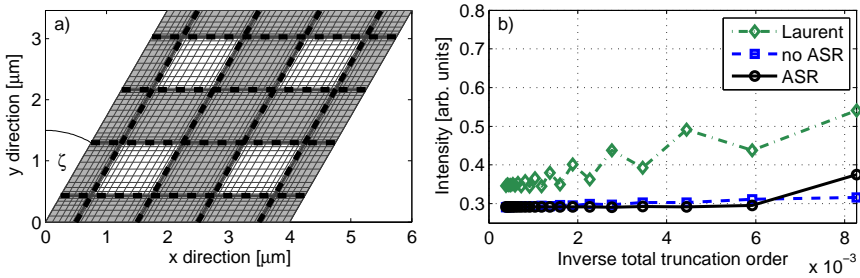
Figure 2.5: (a) Array of holes in a metallic film as defined by example 4 in [10]. (b) Convergence of the absolute square value of the reflection coefficient from the fundamental diffraction order to the fundamental diffraction order at a wavelength of $1\,\mu$m without factorization rules (diamonds), with factorization rules (squares), and additionally adaptive spatial resolution for $\eta = 0.99$ (circles).

As it can be seen in figure 2.5b, the absolute square value of the reflection coefficient from the fundamental diffraction order to the fundamental diffraction order converges worst when using the simple Laurent's rule (diamonds). A tremendous convergence improvement can be achieved by the correct application of factorization rules (squares), whereas the best convergence behavior occurs with factorization rules and adaptive spatial resolution (circles). The coordinate system $Ox^1x^2x^3$ with adaptive spatial resolution has been generated by applying the transformation defined in equation (2.81) to both directions $\check{x}^1$ and $\check{x}^2$ independently with a transformation parameter $\eta = 0.99$ (see mesh in figure 2.5a).

Note that the conjugate metric components $g^{\alpha\beta}$ as well as the determinant g of the metric components have been computed analytically, whereas the Fourier expansion of the redefined permittivity and permeability tensors defined in equation (2.6) has been carried out via the fast Fourier transform algorithm on a spatial grid of 1024×1024 points. The results without adaptive

spatial resolution resemble more or less the findings of figure 6 in reference [10].

Further examples for the superior convergence behavior of calculations with the standard one- and two-dimensional adaptive spatial resolution can be found in references [11–13, 104].

2.7 Comparison between Fourier modal method and experiment

For practical applications, it is not only necessary to achieve a good convergence behavior, but also a good agreement between numerical calculation and experiment. Here, the Fourier modal method with the correct rules of Fourier factorization and adaptive spatial resolution has proven to be quite accurate [45, 47, 48, 66, 105], in spite of the experimental imprecision. In this section, we show exemplarily the numerical and experimental results of our recent publication on plasmon rulers [47].

The general idea of a plasmon ruler is as follows. The spectral response of a specific metallo-dielectric system crucially depends on the spatial arrangement of the metallic elements. The reason is that the plasmonic resonances occurring in the case of single metallic elements hybridize when two or more metallic particles are placed close to each other [50]. Thus, we observe a mode splitting that depends on the distance between the metal particles, which means that we can derive the distance between the particles from the spectral positions of the hybridized modes. However, optically active plasmonic resonances are usually rather broad, so that it is difficult to derive the exact resonance positions from a measured spectrum. Hence, we suggest to couple the broad dipolar resonance of one metal wire to the quadrupolar higher order plasmon resonance of two parallel metal wires, which exhibits a narrow linewidth. Thus, we observe sharp features in the far field spectra, which we can trace in dependence on the spatial arrangement of the metal wires.

As a proof of principle experiment, the structure described in our publication on plasmon rulers is periodic with a period of 600 nm in both lateral directions. The directions of periodicity and the direction of translation invariance are orthogonal with respect to each other ($\zeta = \chi = \xi = 0$). Using a Cartesian coordinate system $Oxyz$ for the description of the spatial arrangement, the sequence of layers is as follows.

The uppermost superstrate layer is an infinite half space filled with air, followed by a homogeneous layer consisting of the photopolymer PC403 (scalar permittivity $\varepsilon = 2.4$) with thickness 30 nm. The next layer contains two parallel y oriented rectangular gold wires with center to center distance 230 nm, variable length L_1, width 80 nm, and height 40 nm. The wires are surrounded

by PC403; their permittivity function is described by a Drude model with $\varepsilon_{AU} = \varepsilon_\infty - \omega_P^2/(\omega^2 + i\gamma\omega)$, where $\epsilon_\infty = 1$, $\omega_P = 1.37 \times 10^{16} \, \text{rad/s}$, and $\gamma = 1.22 \times 10^{14} \, \text{rad/s}$. The next layer is again a homogeneous PC403 layer with thickness 30 nm, followed by a 40 nm thick layer that includes a single x oriented rectangular gold wire with length 260 nm and width 80 nm, which is centered in x direction with respect to the two wires above, but may be shifted by a distance ΔS with respect to the center of the two wires in y direction. After another homogeneous PC403 layer with thickness 30 nm, we have placed a second layer with two y oriented gold wires, which have the same thickness and width as the first two wire layer, but the length L_2 may differ. These wires are positioned exactly below the upper two y oriented wires such that one end of the upper and lower wire pair coincides. Note that a positive y shift of the middle wire by a distance ΔS means a shift towards the coinciding ends of the two wire layers. Schematics of the structure can be seen in figure 2.1a as well as figure 2.6.
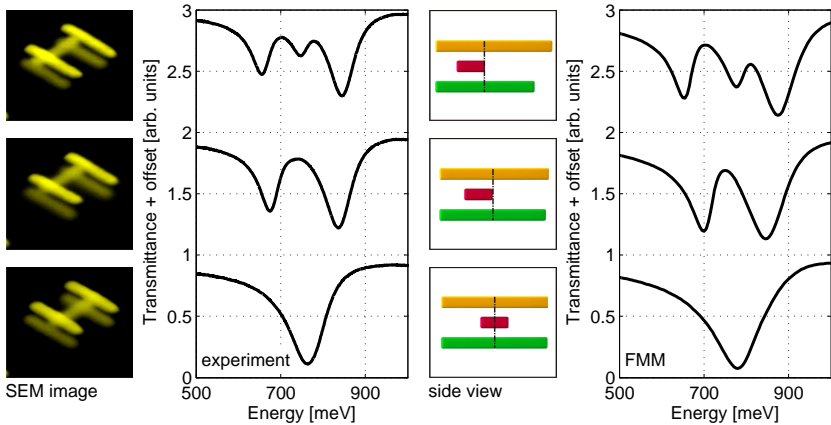
Figure 2.6: Comparison between experimental measurements and numerical results for a periodic multilayer system of metal wires (see figure 2.1a) at normal incidence. The experimentally measured transmittance spectra as well as some scanning electron microscopy (SEM) images can be seen on the left hand side for different spatial configurations. On the right hand side, we show the corresponding numerical results obtained by the Fourier modal method with factorization rules and adaptive spatial resolution for a truncation order of 25×25 harmonics.

Figure 2.6 displays the comparison between experimentally measured[8] and numerically calculated transmittance spectra of the multilayer system in the

---

[8]Fabrication and measurement by M. Hentschel.

case of three different spatial configurations at normal incidence. The uppermost curve depicts results for $L_1 = 340\,\mathrm{nm}$, $L_2 = 270\,\mathrm{nm}$, and $\Delta S = 40\,\mathrm{nm}$. The parameters for the middle curve are $L_1 = 310\,\mathrm{nm}$, $L_2 = 300\,\mathrm{nm}$, and $\Delta S = 40\,\mathrm{nm}$; the bottom curve has been calculated for $L_1 = L_2 = 310\,\mathrm{nm}$ and $\Delta S = 0\,\mathrm{nm}$.

The numerical calculations have been carried out for a truncation order of 25×25 harmonics with the Fourier modal method including factorization rules and adaptive spatial resolution. Note that the interface positions coincide in the adaptive and the physical coordinates; the parameter for adaptive spatial resolution is $\eta = 0.999$ [see equation (2.81)]. The underlying spatial grid contains 1024×1024 points for a good convergence of the fast Fourier transforms. Although the multilayer structure contains many metallic elements with a complex spatial arrangement, the agreement between the numerical results and the experimental measurements is quite good.

3 Matched coordinates

The derivation of accurate numerical results is one of the major problems in modern nano-optics. While the experimentally produced structures can be already quite complex [42, 106], especially the numerical calculation of metallo-dielectric composite structures is quite challenging. One reason for the slow convergence is a poor description of the metallo-dielectric interface using a staircase approximation (see, e.g., figure 2.1c) [107].

In order to avoid any staircasing, we developed the scheme of matched co-ordinates in the Fourier modal method, where general coordinate transformations are applied such that the interfaces can be described everywhere by surfaces of constant coordinates in the new coordinate system. Thus, we are able to combine adaptive spatial resolution and factorization rules in order to describe non-trivial structures such as those shown in figure 3.1 efficiently.
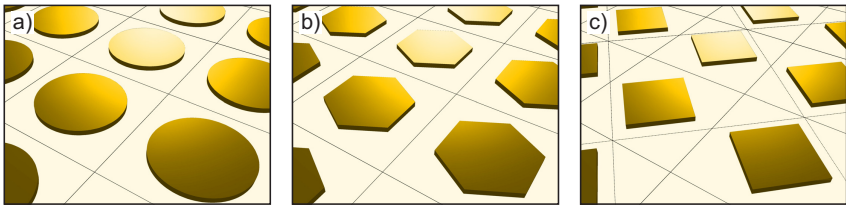
Figure 3.1: Simple structures that cannot be described efficiently by the standard Fourier modal method, either because the material interfaces are not aligned along the axes of periodicity as in case of the examples shown in panel (a) and (b), or it is necessary to consider a larger supercell with more than one element per unit cell for the standard calculations, as in the case of the structure in panel (c). An accurate description at low computational cost requires additional improvements of the Fourier modal method such as the presented concept of matched coordinates.

This chapter is devoted to explaining the general concept of matched coordinates as well as showing its validity in the case of several numerical examples. In addition, we present some possibilities for constructing the required coordinate transformations.

3.1 Invariance of Maxwell's equations

The previous chapter about the classical Fourier modal method has been formulated such that the application of arbitrary coordinate transformations is

rather simple and straight-forward. Most equations of chapter 2 remain correct when considering the coordinate system $Ox^1x^2x^3$ not only as inclined, but as non-uniform and curvilinear. In order to avoid any confusion, let us define here the different available coordinate systems:

1. The physical coordinate system $Oxyz = O\overline{x}^1\overline{x}^2\overline{x}^3$ is orthonormal. Related quantities are denoted by one line over the respective variable.

2. For cases where the directions of periodicity are not orthogonal or the axis of translation invariance does not coincide with the $\overline{x}^3$ axis, we introduce an uniform coordinate system $O\check{x}^1\check{x}^2\check{x}^3$ denoted by a check symbol on top of the respective quantities. The corresponding coordinate transformation $\overline{x}^\alpha = \overline{x}^\alpha(\check{x}^1, \check{x}^2, \check{x}^3)$ is defined by equations (2.1a) to (2.1c).

3. The general coordinate system used in the numerical calculations is defined as $Ouvw = Ox^1x^2x^3$ and can be neither uniform nor orthonormal. In this coordinate system, the material interfaces should be described by surfaces of constant coordinates.

4. In some examples, we introduce also a non-trivial intermediate coordinate system $O\grave{x}^1\grave{x}^2\grave{x}^3$.

3.1.1 General quantities in curvilinear coordinate systems

By choosing a center point in a three-dimensional space, any other point can be displayed as a coordinate vector $\mathbf{r}$ that is determined by the distance and the direction with respect to the center. In a Cartesian coordinate system $O\overline{x}^1\overline{x}^2\overline{x}^3$,

$$\mathbf{r}(\overline{x}^1, \overline{x}^2, \overline{x}^3) = \overline{x}^\alpha \overline{\mathbf{e}}_\alpha, \qquad \alpha = 1, 2, 3. \tag{3.1}$$

Owing to the orthonormality of the Cartesian coordinate system, the coordinates $\overline{x}^\alpha$ are the projection of $\mathbf{r}$ to the orthonormal Cartesian basis vectors $\overline{\mathbf{e}}_\alpha$. Alternatively, $\mathbf{r}$ can be displayed in dependence on new coordinates x^α:

$$\mathbf{r}(x^1, x^2, x^3) = \overline{x}^\alpha(x^1, x^2, x^3)\overline{\mathbf{e}}_\alpha. \tag{3.2}$$

If the transformation is continuous, invertible, and has no singular points, then the above equation defines the coordinate curves $\mathbf{r}(x^1, c^2, c^3)$, $\mathbf{r}(c^1, x^2, c^3)$, and $\mathbf{r}(c^1, c^2, x^3)$ with c^α = constant. The tangential vectors of these curves are usually denoted by $\mathbf{e}_\alpha$ [36, 108]. Furthermore, it is possible to construct coordinate surfaces with $x^\alpha(\overline{x}^1, \overline{x}^2, \overline{x}^3)$ = constant and normal vectors $\mathbf{e}^\alpha$. The vectors $\mathbf{e}_\alpha$ and $\mathbf{e}^\alpha$ can be derived as

$$\mathbf{e}_\alpha = \frac{\partial \mathbf{r}}{\partial x^\alpha}, \qquad \mathbf{e}^\alpha = \overline{\nabla}x^\alpha. \tag{3.3}$$

The orientation of these vectors and curves is depicted for a two-dimensional transformation in figure 3.2(a).
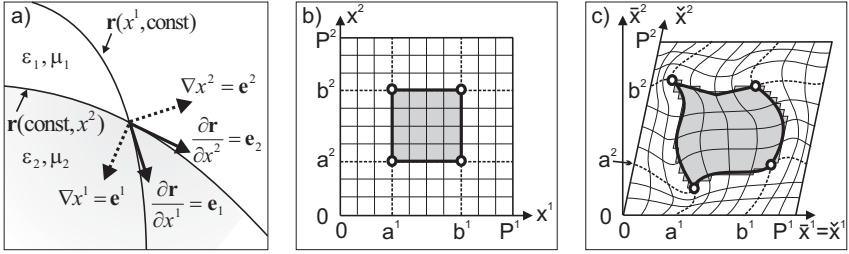
Figure 3.2: Panel (a) depicts the orientation of the conjugate basis vectors $\mathbf{e}^\alpha$ and $\mathbf{e}_\alpha$ of a matched curvilinear coordinate system $Ox^1x^2x^3$, which contains the interface between two materials as a surface of constant x^1. The concept of matched coordinates aims at finding such new coordinate systems $Ox^1x^2x^3$, where the unit cell is rectangular, and the material interfaces are aligned along the axes of periodicity [see panel (b)]. Panel (c) displays an example of matched coordinates in the physical coordinate system $O\overline{x}^1\overline{x}^2\overline{x}^3$, with interfaces described by lines of constant $x^\alpha = a^\alpha$ and $x^\alpha = b^\alpha$. The gray area in panel (c) denotes a staircase approximation of the shape defined by the thick curved black lines. As discussed in chapter 2, the Fourier modal method allows also calculations with non-rectangular unit cells, for which we define the inclined uniform coordinate system $O\breve{x}^1\breve{x}^2\breve{x}^3$.

It is possible to show that the vectors in equation (3.3) form a set of reciprocal bases with $\mathbf{e}^\alpha \cdot \mathbf{e}_\beta = \delta^\alpha_\beta$ [36, 108]. The representation of any vector $\mathbf{A}$ in one of these bases is

$$\mathbf{A} = A^\alpha \mathbf{e}_\alpha = A_\alpha \mathbf{e}^\alpha . \tag{3.4}$$

Note that the representation of vector $\mathbf{A}$ by the coefficients A^α or A_α may be spatially dependent, in contrast to the global representation in uniform coordinate systems.

The covariant component A_α is the projection of $\mathbf{A}$ on $\mathbf{e}_\alpha$, while the contravariant component A^α results from the projection on $\mathbf{e}^\alpha$. These relations can be deduced from the orthogonality relation $\mathbf{e}^\alpha \cdot \mathbf{e}_\beta = \delta^\alpha_\beta$ by scalar multiplication of equation (3.4) with either $\mathbf{e}_\alpha$ or $\mathbf{e}^\alpha$. In addition, we can derive [108]:

$$A_\alpha = (\mathbf{e}_\alpha \cdot \mathbf{e}_\beta) A^\beta = \sum_{\gamma=1}^{3} \frac{\partial \overline{x}^\gamma}{\partial x^\alpha} \frac{\partial \overline{x}^\gamma}{\partial x^\beta} A^\beta = g_{\alpha\beta} A^\beta , \tag{3.5}$$

$$A^\alpha = (\mathbf{e}^\alpha \cdot \mathbf{e}^\beta) A_\beta = \sum_{\gamma=1}^{3} \frac{\partial x^\alpha}{\partial \overline{x}^\gamma} \frac{\partial x^\beta}{\partial \overline{x}^\gamma} A_\beta = g^{\alpha\beta} A_\beta . \tag{3.6}$$

The quantities $g_{\alpha\beta}$ and $g^{\alpha\beta}$ have been introduced in section 2.3.1. With the above equations (3.5) and (3.6), we can interpret them now as tensors that provide the relation between covariant and contravariant components.

The general rule for the transformation of contravariant tensors $\overline{A}^\alpha$ and covariant tensors $\overline{A}_\alpha$ of rank one and weight w from the Cartesian system $O\overline{x}^1\overline{x}^2\overline{x}^3$ to the general non-uniform system $Ox^1x^2x^3$ is as follows [108]:

$$A^\alpha = \sqrt{g}^w \frac{\partial x^\alpha}{\partial \overline{x}^\beta} \overline{A}^\beta , \qquad A_\alpha = \sqrt{g}^w \frac{\partial \overline{x}^\beta}{\partial x^\alpha} \overline{A}_\beta . \tag{3.7}$$

Similarly, we can transform tensors of rank 2 and weight w as

$$A^{\alpha\beta} = \sqrt{g}^w \frac{\partial x^\alpha}{\partial \overline{x}^\gamma} \frac{\partial x^\beta}{\partial \overline{x}^\delta} \overline{A}^{\gamma\delta} , \qquad A_{\alpha\beta} = \sqrt{g}^w \frac{\partial \overline{x}^\gamma}{\partial x^\alpha} \frac{\partial \overline{x}^\delta}{\partial x^\beta} \overline{A}_{\gamma\delta} , \tag{3.8}$$

whereas scalars $\overline{a}$ of weight w obey $a = \sqrt{g}^w \overline{a}$. The quantity g denotes the square root of the metric determinant and is defined in equation (2.8).

3.1.2 Transformation of Maxwell's equations

As discussed in section 2.3.1, Maxwell's equations can be written invariantly as regards well-behaved coordinate transformations. Hence, all relations provided in chapter 2 – except those of section 2.3.4 and 2.4.3 – remain unchanged when redefining the occurring quantities as follows:

1. The covariant components of the electric and magnetic field **E** and **H** transform as absolute tensors of rank one and weight zero as defined in equation (2.4).

2. The contravariant components of the permittivity and permeability tensors $\underline{\underline{\varepsilon}}$ and $\underline{\underline{\mu}}$ transform as relative tensors of rank two and weight one [see equation (2.6)].

3. The contravariant components of the electric displacement and the magnetic induction **D** and **B** as well as the current **j** transform as relative tensors of rank one and weight one [see equations (2.11) and (2.13)].

4. As defined in equation (2.11), the general charge term ϱ transforms as a scalar tensor of weight one.

Thus, even in the case of complicated curvilinear coordinate transformations, we can derive the general solution of Maxwell's equations inside a layer with translation invariance along direction x^3 and periodicity in the directions x^1 and x^2 by the equivalent eigenvalue problem defined in equation (2.27). The

only condition is that $\varepsilon^{\alpha\beta}$ and $\mu^{\alpha\beta}$ do not depend on x^3. In particular, we assume that $\partial\overline{x}^\alpha/\partial x^3 = \text{constant}$ for $\alpha = 1, 2, 3$, and $\overline{\varepsilon}^{\alpha\beta}$ as well as $\overline{\mu}^{\alpha\beta}$ are independent on $\overline{x}^3$. As in the case of uniform coordinate systems, equation (2.27) simplifies to equation (2.31) if $\varepsilon^{3\alpha} = \varepsilon^{\alpha3} = \mu^{3\alpha} = \mu^{\alpha3} = 0$ for $\alpha = 1, 2$.

At this point, we have to emphasize that the reciprocal space in which we describe the lateral components of the electric and magnetic field in the case of non-uniform coordinate systems $Ox^1x^2x^3$ according to equation (2.18) does not coincide with the reciprocal space one would use in the uniform coordinate system $O\breve{x}^1\breve{x}^2\breve{x}^3$. That is one of the main differences between the concept of matched coordinates and the fast Fourier factorization by Popov and others [77–80], where the solution of Maxwell's equations is obtained in the same reciprocal space as in the case of the standard Fourier modal method described in chapter 2.

The most important property for the numerical solution of Maxwell's equations in non-trivial systems $Ox^1x^2x^3$ is that also the boundary conditions (see section 2.5.2) for the normal components of the electric displacement $\mathbf{D}$ and the magnetic induction $\mathbf{B}$ as well as for the tangential components of the electric and magnetic fields $\mathbf{E}$ and $\mathbf{H}$ remain unchanged. In particular, if the material interfaces are described in the coordinate system $Ox^1x^2x^3$ everywhere by surfaces of constant coordinates, we can deduce from equations (3.5) and (3.6) that E_α and H_α as the tangential components as well as D^α and B^α as the normal components are conserved at any interface. Therefore, we can use the same factorization rules for the Fourier transform of the occurring products as provided in section 2.5.

Furthermore, if all layers in a stacked system are described by the same lateral coordinate transformation and share the direction of translation invariance, we can use the scattering matrix formalism described in section 2.4 without any modifications in order to derive the optical properties of such a stacked system. However, care has to be taken in the case of homogeneous layers, as it is described later in section 3.4.

3.1.3 Adaptive spatial resolution in general coordinate systems

An important question is whether the concept of adaptive spatial resolution works even in the case of complicated non-uniform coordinate systems. As we cannot distinguish formally between a complex coordinate transformation and anisotropic permittivity and permeability tensors, it is sufficient to show that the principles of adaptive spatial resolution described in section 2.6.1 are valid in the case of the latter.

Let us consider a coordinate system $O\grave{x}^1\grave{x}^2\grave{x}^3$, in which $\grave{\varepsilon}^{\alpha\beta}$ and $\grave{\mu}^{\alpha\beta}$ denote

the components of general anisotropic permittivity and permeability tensors. Furthermore, we describe the transformation between $O\grave{x}^1\grave{x}^2\grave{x}^3$ and the coordinate system $Ox^1x^2x^3$ with adaptive spatial resolution by the functions $\grave{x}^1(x^1)$ and $\grave{x}^2(x^2)$ as defined in equation (2.81), and $\grave{x}^3 = x^3$. Thus, the redefined permittivity and permeability tensors $\underline{\underline{\varepsilon}}$ and $\underline{\underline{\mu}}$ can be obtained according to equation (2.6) as

$$
A = \begin{pmatrix} \dfrac{\partial x^1}{\partial \grave{x}^1} \dfrac{\partial x^2}{\partial \grave{x}^2} \end{pmatrix}^{-1} \begin{pmatrix} \dfrac{\partial x^1}{\partial \grave{x}^1} & 0 & 0 \\ 0 & \dfrac{\partial x^2}{\partial \grave{x}^2} & 0 \\ 0 & 0 & 1 \end{pmatrix} \begin{pmatrix} \grave{A}^{11} & \grave{A}^{12} & \grave{A}^{13} \\ \grave{A}^{21} & \grave{A}^{22} & \grave{A}^{23} \\ \grave{A}^{31} & \grave{A}^{32} & \grave{A}^{33} \end{pmatrix} \begin{pmatrix} \dfrac{\partial x^1}{\partial \grave{x}^1} & 0 & 0 \\ 0 & \dfrac{\partial x^2}{\partial \grave{x}^2} & 0 \\ 0 & 0 & 1 \end{pmatrix}
$$

$$
= \begin{bmatrix} \left(\dfrac{\partial \grave{x}^1}{\partial x^1}\right)^{-1} \dfrac{\partial \grave{x}^2}{\partial x^2} \grave{A}^{11} & \grave{A}^{12} & \dfrac{\partial \grave{x}^2}{\partial x^2} \grave{A}^{13} \\ \grave{A}^{21} & \dfrac{\partial \grave{x}^1}{\partial x^1} \left(\dfrac{\partial \grave{x}^2}{\partial x^2}\right)^{-1} \grave{A}^{22} & \dfrac{\partial \grave{x}^1}{\partial x^1} \grave{A}^{23} \\ \dfrac{\partial \grave{x}^2}{\partial x^2} \grave{A}^{31} & \dfrac{\partial \grave{x}^1}{\partial x^1} \grave{A}^{32} & \dfrac{\partial \grave{x}^1}{\partial x^1} \dfrac{\partial \grave{x}^2}{\partial x^2} \grave{A}^{33} \end{bmatrix} = \begin{pmatrix} A^{11} & A^{12} & A^{13} \\ A^{21} & A^{22} & A^{23} \\ A^{31} & A^{32} & A^{33} \end{pmatrix},
$$

$$(3.9)$$

where the 3×3 tensor A denotes either $\underline{\underline{\varepsilon}}$ or $\underline{\underline{\mu}}$. Looking at the correct application of the Fourier factorization rules defined in equation (2.77), we find that the Fourier transform in direction γ involves always the pair of operators $\hat{F}_\gamma \hat{l}_\gamma^-$. According to equation (2.20), the operator $\hat{l}_\gamma^-$ contains the inverse of $A^{\gamma\gamma}$, which yields in the case of equation (3.9) the following expressions:

$$
(A^{11})^{-1} = \frac{\partial \grave{x}^1}{\partial x^1} \left(\frac{\partial \grave{x}^2}{\partial x^2} \grave{A}^{11} \right)^{-1}, \qquad (A^{22})^{-1} = \frac{\partial \grave{x}^2}{\partial x^2} \left(\frac{\partial \grave{x}^1}{\partial x^1} \grave{A}^{22} \right)^{-1}. \quad (3.10)
$$

Almost every element in equation (2.20) contains these inverse elements, except the terms $A^{\alpha\beta}$ with $\alpha \neq \gamma$ and $\beta \neq \gamma$. However, these elements are also proportional to $\partial \grave{x}^\gamma / \partial x^\gamma$, so that all the elements of $\tilde{A} = \hat{l}_\gamma^\pm(A)$ fulfill $\tilde{A}^{\alpha\beta} \propto \partial \grave{x}^\gamma / \partial x^\gamma$ for $\alpha, \beta = 1, 2, 3$.

As $\partial \grave{x}^\gamma / \partial x^\gamma$ is by construction small at any interface, the effective jump height is reduced before carrying out the Fourier transform in direction γ. Hence, the influence of the Gibbs phenomenon should be decreased for both of the subsequent Fourier transformations in equation (2.77). Thus, the principles of adaptive spatial resolution are valid even for non-trivial permittivity and permeability tensors due to anisotropic media or general coordinate transformations or both.

Note that we assumed so far an independent application of adaptive spatial resolution in the directions $\grave{x}^1$ and $\grave{x}^2$. In practical applications, it turns out that this is not a necessary condition, and we can apply adaptive spatial resolution locally inside an unit cell [81], so that adaptive spatial resolution cannot be formally separated from the matched coordinates anymore.

3.2 Derivation of appropriate coordinate transformations

As described above, the application of general coordinate transformations is straight-forward in the Fourier modal method and can be combined easily with the correct application of factorization rules if the interfaces are described everywhere by surfaces of constant coordinates. The remaining problem is the derivation of appropriate transformations including adaptive spatial resolution.

The most powerful tool for the derivation of the coordinate transformations would be an automatized procedure with interfaces as the input and the matched coordinates as the output. Some work has been devoted to this problem in the case of the Fourier modal method by minimizing a fictitious functional favoring points close to the interfaces [81, 109]. The concept is taken from a paper on the derivation of adaptive coordinates for calculations of the electronic structure of molecules [110]. In general, this approach is quite promising, but the minimization has to be carried out over a large parameter space, which makes the method rather slow.

In this work, we present some alternatives that provide appropriate coordinate transformations for a large class of problems. The advantage of these methods compared to the minimization of a fictitious functional is a fast computation of the coordinate transformations for various geometry parameters.

3.2.1 Scheme of smooth modulation

A quite intuitive approach for finding appropriate coordinate transformations is to imagine that the matched coordinates arise from a deformation of the standard uniform coordinate system inside the unit cell. Then, adaptive spatial resolution can be added in a second step on such a deformed system. In general, it may be difficult to derive an expression for the transformation between the different coordinate systems. However, for some simple systems, we can derive the transformation rather easily.

It should be kept in mind that we have to apply the transformation to matched coordinates only in the lateral directions, because we assume a translation invariance in direction $\check{x}^3$ of the underlying uniform coordinate system $O\check{x}^1\check{x}^2\check{x}^3$. Hence, we can define in this section $x^3 = \check{x}^3$ and neglect for the sake of simplicity the x^3 dependence of the provided functions describing the coordinate transformations.

Hexagonal structure

In the simplest kind of lateral geometries, it is sufficient to construct a transformation $\breve{x}^\alpha(x^1, x^2)$ for only one lateral coordinate. For instance, as seen in figure 3.3a, a hexagonal structure can be aligned in a quadratic unit cell such that two planar interfaces are oriented tangential to the directions $\breve{x}^2 = y$ and $\breve{x}^3 = z$. In that case, we have to find only an appropriate transformation $\breve{x}^2(x^1, x^2)$, because all surfaces with constant $\breve{x}^1 = x$ are already matched to the lateral geometry.
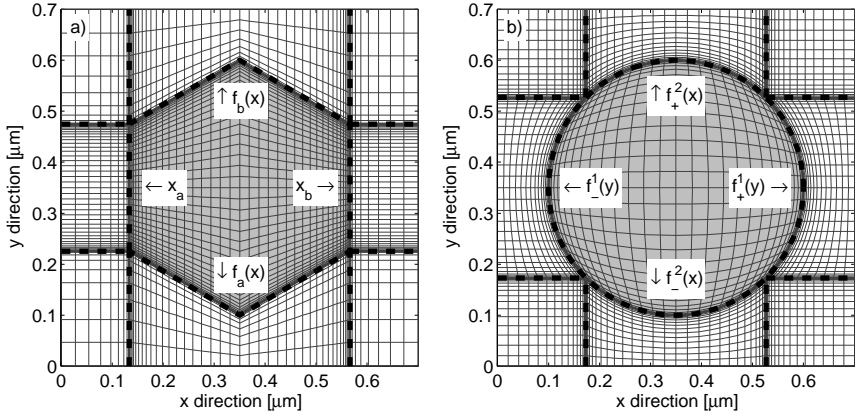
Figure 3.3: Examples of coordinate transformations matching a periodic array of hexagons in panel (a) and circular cylinders in panel (b).

Let $\breve{x}^1_{\mathrm{a}}$ and $\breve{x}^1_{\mathrm{b}}$ be the vertical interface positions of a given structure. Furthermore, the bottom and top interfaces can be described inside the planar unit cell by functions $f_{\mathrm{a}}(\breve{x}^1)$ and $f_{\mathrm{b}}(\breve{x}^1)$, respectively. Then, we can introduce new coordinates x^1 and x^2 with $x^1 = \breve{x}^1$ such that $\breve{x}^2(x^1, x^2_{\mathrm{a/b}}) \equiv f_{\mathrm{a/b}}(\breve{x}^1)$, and

$$
\breve{x}^2(x^1, x^2) = \begin{cases}
\dfrac{x^2 + P^2 - x_{\mathrm{b}}^2}{x_{\mathrm{a}}^2 + P^2 - x_{\mathrm{b}}^2} f_{\mathrm{a}}(x^1) + \dfrac{x^2 - x_{\mathrm{a}}^2}{x_{\mathrm{b}}^2 - P^2 - x_{\mathrm{a}}^2} f_{\mathrm{b}}(x^1) & \text{for } 0 \le x^2 \le x_{\mathrm{a}}^2, \\[3mm]
\dfrac{x^2 - x_{\mathrm{b}}^2}{x_{\mathrm{a}}^2 - x_{\mathrm{b}}^2} f_{\mathrm{a}}(x^1) + \dfrac{x^2 - x_{\mathrm{a}}^2}{x_{\mathrm{b}}^2 - x_{\mathrm{a}}^2} f_{\mathrm{b}}(x^1) & \text{for } x_{\mathrm{a}}^2 \le x^2 \le x_{\mathrm{b}}^2, \\[3mm]
\dfrac{x^2 - x_{\mathrm{b}}^2}{x_{\mathrm{a}}^2 + P^2 - x_{\mathrm{b}}^2} f_{\mathrm{a}}(x^1) + \dfrac{x^2 - P^2 - x_{\mathrm{a}}^2}{x_{\mathrm{b}}^2 - P^2 - x_{\mathrm{a}}^2} f_{\mathrm{b}}(x^1) & \text{for } x_{\mathrm{b}}^2 \le x^2 \le P^2.
\end{cases}
$$

$$(3.11)$$

Owing to the linear interpolation between different functions $f_{\mathrm{a}}(\breve{x}^1)$ and $f_{\mathrm{b}}(\breve{x}^1)$, we refer to the construction of such coordinate transformations as the

scheme of smooth modulation. Note that we assume $f_a(\check{x}^1)$ and $f_b(\check{x}^1)$ to be defined over the whole unit cell and periodic with period P^1. The interval $[0, x_a^2]$ describes the area below the bottom interface, whereas $[x_b^2, P^2]$ is located above the top interface. In addition, we can apply adaptive spatial resolution to the above defined coordinate transformation by replacing x^1 and x^2 with functions $\grave{x}^1(x^1)$ and $\grave{x}^2(x^2)$ that are constructed using equation (2.81).

Circular structure

For some structures, we can derive an analytic expression for the coordinate transformation even when we have to deform both coordinates x^1 and x^2 in order to match the material interfaces. One example is the transformation to match a periodic array of circular cylinders in a rectangular unit cell depicted in figure 3.3b.

Let us denote the radius of the cylinders by R and consider without the loss of generality the situation, where the cylinders are centered in one unit cell described by $x = \overline{x}^1 \in [0, P^1)$ and $y = \overline{x}^2 \in [0, P^2)$. Thus, the interfaces can be written as lines

$$f_\pm^\alpha(x^{\beta \neq \alpha}) = \begin{cases} \frac{P^\alpha}{2} \pm \sqrt{R^2 - \left(x^\beta - \frac{P^\beta}{2}\right)^2} & \text{for } c_-^\beta \leq x^\beta \leq c_+^\beta , \\ c_\pm^\alpha & \text{elsewhere} , \end{cases} \quad (3.12)$$

with $c_\pm^\alpha = (P^\alpha \pm \sqrt{2}R)/2$ (see figure 3.3b). Similarly to the hexagons, we can construct the transformation $\overline{x}^\alpha(x^1, x^2)$ by smoothly changing the profile between the border of the unit cell and the functions $f_\pm^\alpha$ [11]:

$$\overline{x}^\alpha(x^\alpha, x^{\beta \neq \alpha}) = \begin{cases} \dfrac{x^\alpha}{c_-^\alpha} \, f_-^\alpha(x^\beta) & \text{for } 0 \leq x^\alpha < c_-^\alpha , \\[2ex] \dfrac{x^\alpha - c_-^\alpha}{c_+^\alpha - c_-^\alpha} \, f_+^\alpha(x^\beta) + \dfrac{x^\alpha - c_+^\alpha}{c_-^\alpha - c_+^\alpha} \, f_-^\alpha(x^\beta) & \text{for } c_-^\alpha \leq x^\alpha \leq c_+^\alpha , \\[2ex] \dfrac{x^\alpha - P^\alpha}{c_+^\alpha - P^\alpha} \, f_+^\alpha(x^\beta) + \dfrac{x^\alpha - c_+^\alpha}{P^\alpha - c_+^\alpha} \, P^\alpha & \text{for } c_+^\alpha < x^\alpha \leq P^\alpha . \end{cases}$$

$$(3.13)$$

As in the previous section, we can introduce adaptive spatial resolution by substituting $\grave{x}^\alpha(x^\alpha)$ for x^α.

General approach

The scheme of smooth modulation can be extended also to more complicated structures than the periodic array of hexagonal or circular shapes. A schematic of the approach can be seen in figure 3.4.
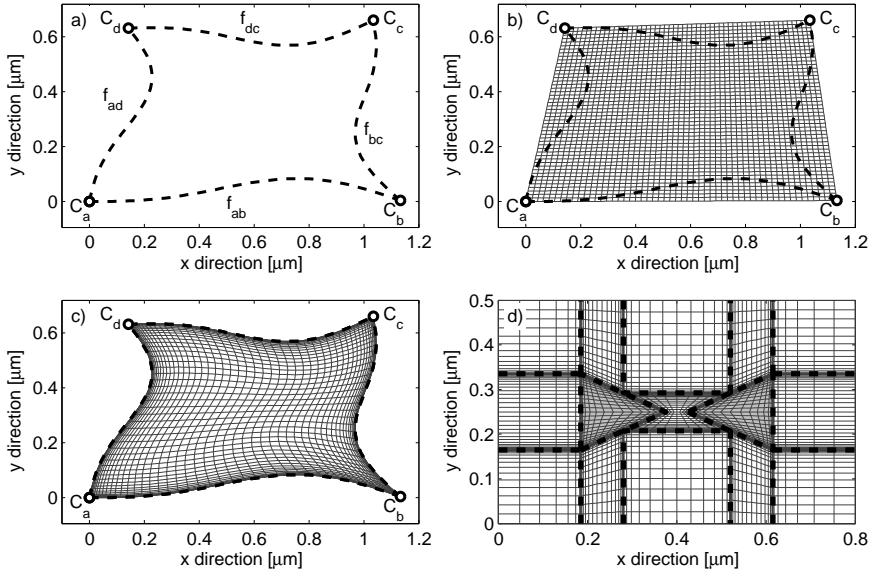
Figure 3.4: (a) Corner points C_m (circles) and boundary lines f_{mn} (dashed lines) of a more or less arbitrarily shaped area. (b) Reference system of straight lines as defined by equation (3.14). (c) Coordinate lines with adaptive spatial resolution that are constructed by equation (3.15) and match the boundary lines. (d) Example of a bowtie structure constructed via sectioning of the unit cell (dashed lines) and using equation (3.15) for the description of the areas in between.

In general, the idea is to separate the unit cell into several areas – as it is indicated by the dashed boundary lines in figures 3.2 to 3.4 – and to derive a system of matched coordinates for each area independently. An appropriate division of the unit cell depends on the given geometry, but it is essential that the material interfaces are described in the lateral directions by boundary lines.

Using an orthonormal coordinate system $O\overline{x}^1\overline{x}^2\overline{x}^3$, each area can be defined in the $\overline{x}^1\overline{x}^2$ plane by four corner points $C_a = (c_a^1, c_a^2)$, $C_b = (c_b^1, c_b^2)$, $C_c = (c_c^1, c_c^2)$, and $C_d = (c_d^1, c_d^2)$ as well as by the boundary lines $f_{ab}(s) = [f_{ab}^1(s), f_{ab}^2(s)]$, $f_{bc}(s) = [f_{bc}^1(s), f_{bc}^2(s)]$, $f_{dc}(s) = [f_{dc}^1(s), f_{dc}^2(s)]$, and $f_{ad}(s) = [f_{ad}^1(s), f_{ad}^2(s)]$ in between (see figure 3.4a). Without the loss of generality, we choose the parameterization of the lines $f_{mn}(s)$ such that $f_{mn}(0) = C_m$ and $f_{mn}(1) = C_n$ for $m, n = a, b, c, d$.

The next step is to create in each area an intermediate coordinate system

$O\grave{x}^1\grave{x}^2\grave{x}^3$, laterally consisting of straight lines (see figure 3.4b)

$$\grave{x}^\alpha(s^1,s^2) = c_a^\alpha + (c_b^\alpha - c_a^\alpha)s^1 + [c_d^\alpha + (c_c^\alpha - c_d^\alpha)s^1 - c_a^\alpha - (c_b^\alpha - c_a^\alpha)s^1]s^2 \,, \quad (3.14)$$

where $\alpha = 1, 2$; the third component should remain unchanged with $\grave{x}^3 = x^3$. As for the parameterization of $f_{mn}(s)$, we define $0 \leq s^\alpha \leq 1$. The straight lines $\grave{x}^\alpha$ serve as a reference frame that deviates at the boundary lines from the desired geometry as follows:

$$\Delta_{mn}^\alpha(s) = f_{mn}^\alpha(s) - c_m^\alpha - (c_n^\alpha - c_m^\alpha)s \,. \quad (3.15)$$

As $\Delta_{mn}^\alpha(0) = \Delta_{mn}^\alpha(1) = 0$, we are able to construct the coordinate lines $\overline{x}^1(s^1, s^2)$ and $\overline{x}^2(s^1, s^2)$ matching the boundary lines via a linear interpolation:

$$\begin{aligned}\overline{x}^\alpha(s^1, s^2) =& \grave{x}^\alpha(s^1, s^2) + \Delta_{ab}^\alpha(s^1)(1 - s^2) \\ &+ \Delta_{dc}^\alpha(s^1)s^2 + \Delta_{ad}^\alpha(s^2)(1 - s^1) + \Delta_{bc}^\alpha(s^2)s^1 \,.\end{aligned} \quad (3.16)$$

As in the previous examples, we can add adaptive spatial resolution by replacing s^α with $\grave{s}^\alpha(s^\alpha)$, where $\grave{s}^\alpha(s^\alpha)$ is defined by equation (2.81). An example of such a coordinate transformation can be seen in figure 3.4c.

This general method of constructing adaptive coordinate systems provides the possibility to describe a large variety of different structures such as the bowtie depicted in figure 3.4d. In the case of metallic bowties, these structures may exhibit a high field enhancement between the tips of the opposing triangles, leading to enhanced nonlinear effects [106], but the numerical derivation of even the linear properties is very challenging.
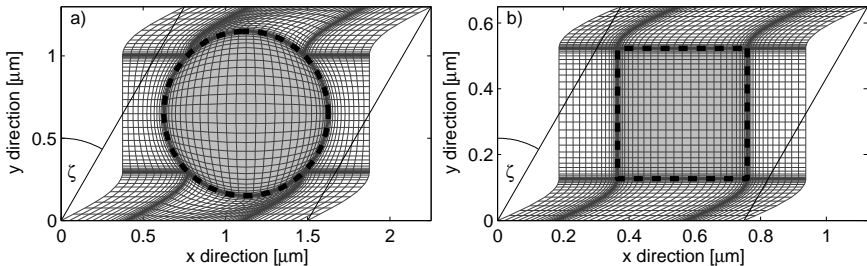
Figure 3.5: Equilateral triangular lattice of cylinders in panel (a) and squares in panel (b) with equal periods $P^1 = P^2$ and $\zeta = 30°$.

It should be mentioned that it is not necessary to keep the border of the unit cell invariant under the coordinate transformation. Sometimes, it even cannot be avoided to deviate at the border of the unit cell from the uniform coordinate

system $O\breve{x}^1\tilde{x}^2\tilde{x}^3$, or it simplifies the derivation of appropriate coordinate transformations significantly. For instance, we can derive transformations matching shapes with curved interfaces in non-rectangular unit cells by shifting parts of the unit cell below or above the material interfaces. Thus, we can calculate the equilateral triangular lattice of cylinders depicted in figure 3.5a, as well as the inclined system of squares shown in figure 3.5b.

With the method of smooth modulation, it is also possible to construct matched coordinates for structures that evolve from a rotation of a rectangular structure inside the unit cell. The example depicted in figure 3.6a exhibits coordinate lines that are either normal or tangential at the material interfaces with smooth coordinate derivatives, whereas figure 3.6b has been constructed without these additional restrictions for the same rotation angle of 45°.
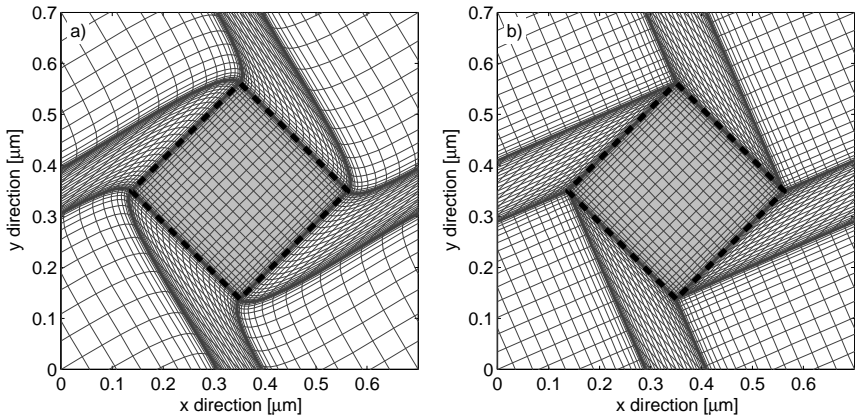
Figure 3.6: Coordinate transformations matching a rotated square with normal coordinate lines at the interfaces in panel (a) and simply straight lines in panel (b).

Note that the quality of the coordinate transformation strongly depends on the sectioning of the unit cell. Unfortunately, we cannot provide general rules for an optimized coordinate transformation up to now, and the obtained transformations have to be tested individually.

3.2.2 Rotated elements

In order to compare different coordinate transformations, we want to introduce also an alternative for the construction of coordinate systems matching rotated elements, which is specifically designed for such systems.

The starting point is an unrotated structure described in an intermediate coordinate system $O\mathring{x}^1\mathring{x}^2\mathring{x}^3$ that may contain adaptive spatial resolution and that exhibits interfaces perfectly aligned along the axes of periodicity inside a rectangular unit cell (see figure 3.7a). The outermost interfaces provide us a rectangle (white line in figure 3.7a) that is supposed to be rotated by a specific angle φ inside the $\mathring{x}^1\mathring{x}^2$ plane. For this purpose, we construct a function $h(\mathring{x}^1,\mathring{x}^2)$ such that

$$h(\mathring{x}^1,\mathring{x}^2) = \begin{cases} 1 & \text{at the border of the unit cell}\,, \\ 0 & \text{inside the unrotated rectangle}\,. \end{cases} \qquad (3.17)$$

In addition, h should change smoothly between 0 and 1 outside the rectangle.
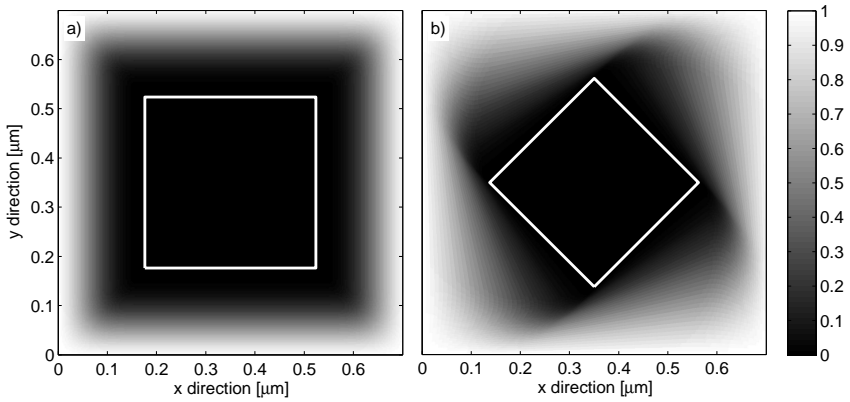
Figure 3.7: (a) Unrotated and (b) rotated square (white lines) inside a rectangular unit cell. The background color denotes a function h_1 that equals zero inside the square and one at the border of the unit cell. Thus, we can define a local degree of rotation in the unit cell with maximum rotation at points with $h_1 = 0$ and no rotation at $h_1 = 1$.

An example for such a function is indicated by the background color in figure 3.7a, which has been constructed by normalizing the distance between points outside the unrotated rectangle and the boundary lines of the rectangle. Thus, the profile changes almost linearly from 0 to 1, except at the corners of the unit cell. Henceforth, we refer to this function as h_1. Using h_1 as a starting point, we can furthermore defined the following alternative smooth functions:

$$h_2 = h_1^2\,, \qquad h_3 = -2\left(h_1 - \frac{1}{2}\right)^3 + \frac{3}{2}h_1 - \frac{1}{4}\,. \qquad (3.18)$$

The subscripts denote the order of the polynomial with argument h_1.

    With the function h, we can define a local degree of rotation inside the unit cell that changes between unrotated at the border of the unit cell and maximum rotation at the border and inside of the rotated rectangle.

    The concept of a smooth function h has been taken from a paper by Antos [80], where it is suggested to smoothly alter the polarization bases for the application of the fast Fourier factorization [77] between circular at the border as well as the center of the unit cell and linear at the border of a round cylinder. Hence, it is necessary to describe the local polarization state by a smooth function similar to h, which is – in contrast to our function – also one at the center of the unit cell.

    As a next step, it is convenient to map the lateral components $\dot{x}^1$ and $\dot{x}^2$ to the complex plane as $\dot{X} \equiv \dot{x}^1 + i\dot{x}^2$. Thus, we can define the rotation of the rectangle by the function

$$\mathrm{R}(\dot{X}, \dot{X}_0, \varphi) = (\dot{X} - \dot{X}_0)\mathrm{e}^{i\varphi} + \dot{X}_0 \,, \tag{3.19}$$

where $\dot{X}_0$ defines the center of the rectangle, and φ denotes the rotation angle. Hence, the coordinate transformation matching the rotated rectangle can be found as $\overline{x}^1 = \Re(\overline{X})$ and $\overline{x}^2 = \Im(\overline{X})$, with

$$\overline{X} = \mathrm{R}[\dot{X}, \dot{X}_0, (1 - h)\varphi] \,. \tag{3.20}$$

Depending on the function h, we can influence the behavior of the coordinate transformation. Using simply function h_1 results in merely a small deformation of the unit cell, but we observe discontinuous coordinate derivatives at the edges of the rectangle and the border of the unit cell (see figure 3.8a). Function h_2 leads to transformations that exhibit continuous coordinate derivatives at the edges of the rotated rectangle, but the coordinate derivatives are not continuous at the border of the unit cell (see figure 3.8b). Completely continuous coordinate derivatives can be achieved by using function h_3. However, this results in a strong deformation of the unit cell and works only in cases where the rectangle is small enough compared to the unit cell. Therefore, we refrain from the application of h_3 in the following.

    In contrast to the transformations in figure 3.6, the transformations obtained by equation (3.20) equal the unrotated coordinate system at the border of the unit cell (see figure 3.8). Hence, it may be a drawback of the method that there are areas inside the unit cell at which the matched coordinates deviate strongly from the uniform coordinate system, resulting in large coordinate derivatives, or – in some cases – a complete failure of the approach. On the other hand, the concept is rather simple and straight-forward, because it is not necessary to think about an appropriate sectioning of the unit cell.
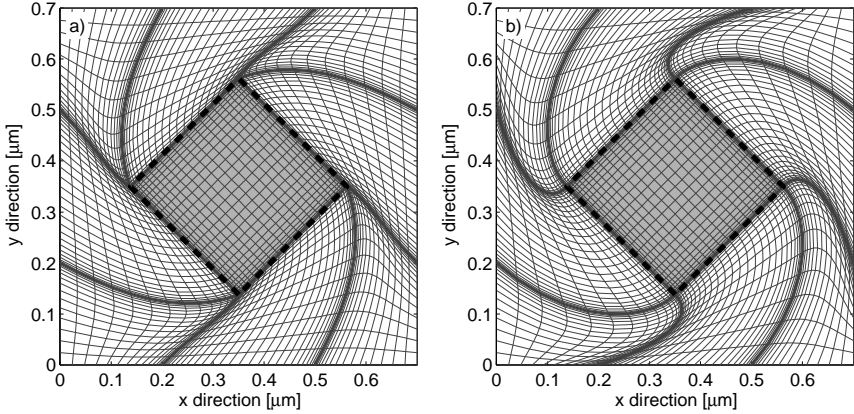
Figure 3.8: Alternative coordinate transformations matching a rotated square. The transformations have been constructed by equation (3.20) using the smooth function h_1 for panel (a) and h_2 for panel (b).

It should be mentioned that the presented concepts for rotated systems can be applied in order to rotate structures that are more complex than rectangles aligned in the unit cell. One example may be a periodic array of split ring resonators, where each split ring is rotated by a specific angle inside the unit cell [9]. Alternatively, the rotated rectangle can itself contain a curvilinear coordinate transformation such as the transformations depicted in figure 3.3. For the sake of simplicity, we have merely discussed the peculiar case of the rectangles.

3.3 Array of dielectric cylinders

As the first test system of the matched coordinates, we discuss in the following a periodic array of dielectric cylinders. The coordinate transformation matching such a system is depicted in figure 3.3b. For the sake of simplicity, we define the permeability to be $\overline{\mu}^{\alpha\beta} = \delta^{\alpha\beta}$ in all further calculations.

3.3.1 Solution for isolated cylinders

The problem of an isolated cylinder can be solved analytically by considering Maxwell's equations in cylindrical coordinates and results in a transcendental equation for an effective propagation constant λ in the invariant direction of

the cylinder [56].

Let us denote the radius of the cylinder by R and define scalar permittivity and permeability values as ε_m and μ_m, respectively, with $m = 1$ inside and $m = 2$ outside the cylinder. Then, the transcendental equation for the effective propagation constant λ is

$$\frac{n^2\lambda^2}{R^2}\left(\frac{1}{\kappa_1^2} - \frac{1}{\kappa_2^2}\right)^2 - k_0^2\left(\frac{\mu_1\tilde{J}_n}{\kappa_1} + \frac{\mu_2\tilde{K}_n}{i\kappa_2}\right)\left(\frac{\varepsilon_1\tilde{J}_n}{\kappa_1} + \frac{\varepsilon_2\tilde{K}_n}{i\kappa_2}\right) = 0\,, \quad (3.21)$$

where

$$\kappa_m = \sqrt{k_0^2\varepsilon_m\mu_m - \lambda^2}\,, \qquad \tilde{J}_n = \frac{J_n'(\kappa_1 R)}{J_n(\kappa_1 R)}\,, \qquad \tilde{K}_n = \frac{K_n'(-i\kappa_2 R)}{K_n(-i\kappa_2 R)}\,, \quad (3.22)$$

with $J_n(x)$ as the Bessel function of the first kind, $K_n(x)$ as the modified Bessel function of the second kind, and the prime denoting the derivative of $J_n(x)$ and $K_n(x)$ with respect to the argument x, respectively. The solutions can be distinguished by the integer n occurring as the order parameter of the Bessel functions. For $n = 0$, we find independent sets of transverse electric (TE) and transverse magnetic (TM) fiber modes, whereas the fundamental fiber mode HE_{11} with no cut-off energy is found for $n = 1$ [56].

The solution of equation (3.21) can be derived numerically with an accuracy that is more or less limited only by the machine precision. In the following examples, we have chosen the tolerance for finding solutions of equation (3.21) to be $< 10^{-15}$, which is more than enough for a comparison with the Fourier modal method. Henceforth, we refer to these solutions of equation (3.21) as λ^{exact}.

3.3.2 Comparison with isolated cylinders

If the solution of the fields decays exponentially outside the cylinder and the decay length is much shorter than the size of the chosen period in the Fourier modal calculation, the interaction of different unit cells can be neglected for such modes. Hence, the propagation constant λ^{exact} should be a solution of the eigenvalue problem defined by equation (2.27).

We chose a structure with vacuum outside and $\varepsilon = 4$ inside the cylinder [11]. The diameter is $2R = 1\,\mu\text{m}$ and the unit cell size is $1.5\,\mu\text{m} \times 1.5\,\mu\text{m}$. At $2562.21\,\text{meV}$, we determined the propagation constants of the HE_{11} mode as $\lambda_{\text{HE}}^{\text{exact}} = 25.56\ 1/\mu\text{m}$, the fundamental TE mode as $\lambda_{\text{TE}}^{\text{exact}} = 25\ 1/\mu\text{m}$, and the fundamental TM mode as $\lambda_{\text{TM}}^{\text{exact}} = 24.87\ 1/\mu\text{m}$. As $K_n(x) \propto \exp(-x)$ for $x \to \infty$, and $-i\kappa_2 \approx 21$ for $\lambda \approx 25$ at $2562.21\,\text{meV}$, we can estimate the decay of these modes to be in the order of $\exp(-21)$ at a distance of $1\ \mu\text{m}$ away from the center of the cylinder. The mode profiles are depicted in figure 3.9.
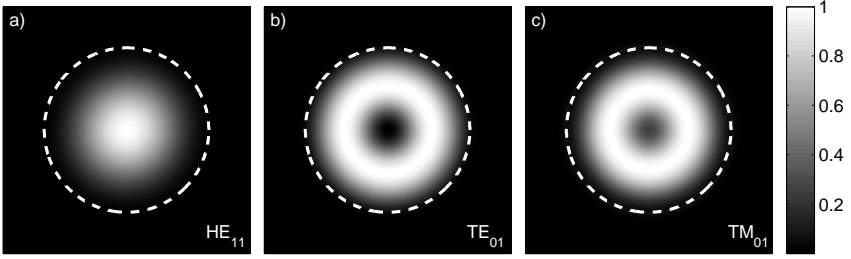
Figure 3.9: Three different fundamental fiber modes that are used for comparison between exact results of single cylinders and solutions of the Fourier modal method with a periodic array of cylinders. The mode profiles have been extracted from the Fourier modal method using a truncation order of 25×25 harmonics. The gray scale denotes the energy density of the electric field normalized to the maximum value. All three modes decay more or less rapidly outside the cylinder (interface indicated by dashed white line).

The relative deviation between the numerical solutions and the analytically derived propagation constant can be seen in figure 3.10. By square symbols, we depict the results for a zig-zag approximation of the cylinders in a square lattice configuration, where the round interface of the cylinders is replaced in a Cartesian coordinate system $O\overline{x}^1\overline{x}^2\overline{x}^3$ by surfaces of constant $\overline{x}^1$ and $\overline{x}^2$, respectively. A schematic of such a zig-zag approximation can be seen in figure 2.1c. While the latter sketch shows a coarse zig-zag approximation, we used a very fine approximation in the calculations with a side length in the order of 1 nm.

The results with matched coordinates and adaptive spatial resolution are displayed for two different lattice configurations; a square lattice (circles) with a transformation according to equation (3.13) and an equilateral triangular lattice (diamonds) with an unit cell as depicted in figure 3.5.

All numerical results were obtained at normal incidence with $k_1 = k_2 = 0$. The parameter for the adaptive spatial resolution [see equation (2.81)] is $\eta = 0.99$. For all three fiber modes, we observe an increased convergence behavior using matched coordinates, independently on the lattice configuration.[1]

In order to allow a better comparison with other methods or implementations of the concept of matched coordinates, we provide the numerically derived propagation constant λ for the fundamental TE mode also in table 3.1.

---

[1]In principle, it would be preferable to compare our results with the normal vector field approach [78], as it is superior compared to the zig-zag approximation. However, we have not implemented this method yet.
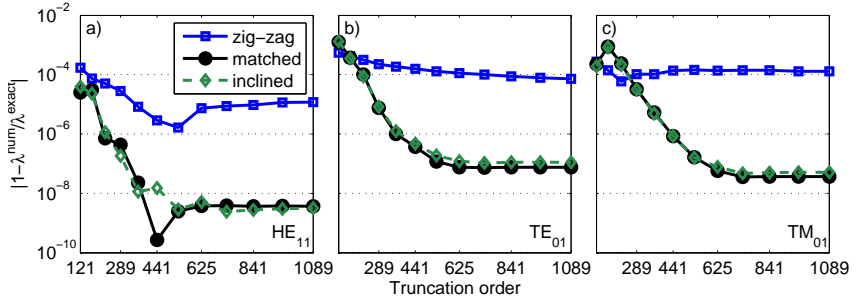
Figure 3.10: Relative deviation between exact propagation constants of single cylinders and solutions for equation (2.27) obtained with and without matched coordinates for varying total truncation orders. The corresponding mode profiles can be seen in figure 3.9. The different lines depict solutions of the Fourier modal method for a zig-zag approximation of the cylinder (squares) as well as matched coordinates for cylinders in a square lattice (circles) and an equilateral triangular lattice with an inclined unit cell (diamonds). Starting from 289 harmonics, the scheme with matched coordinates is superior to the zig-zag approximation in all three examples, independently on the lattice configuration.

$N_1 \times N_2$	zig-zag	matched	inclined
11×11	24.986337483	24.968437868	24.967105007
13×13	24.989639658	24.990751544	24.991167549
15×15	24.992071833	24.997479027	24.997796029
17×17	24.994369210	24.999808869	24.999792612
19×19	24.995390180	24.999974789	24.999968379
21×21	24.996045273	24.999990818	24.999988351
23×23	24.996777530	24.999997029	24.999995320
25×25	24.997214319	24.999998088	24.999996939
27×27	24.997495400	24.999998181	24.999997364
29×29	24.997815900	24.999998134	24.999997246
31×31	24.998044004	24.999998134	24.999997217
33×33	24.998197869	24.999998131	24.999997215

Table 3.1: Values of the propagation constant λ derived by the Fourier modal method for the fundamental TE mode with $\lambda^{\text{exact}} = 25\ 1/\mu\text{m}$ at $2562.2076384\,\text{meV}$ for different truncation orders $N_G = N_1 \times N_2$.

Note that we have achieved an improved convergence compared to our paper on matched coordinates [11], because we chose a higher parameter for the adaptive spatial resolution and we designed the coordinate transformation such

that the interfaces of the cylinder are located between two grid lines on the lateral spatial grid of 1024×1024 points. Thus, the fast Fourier transform resembles the desired cylinder radius better than in cases where the cylinder interface is included explicitly on the grid. The reason is that there exists an ambiguity on the exact position of discontinuities in the discrete Fourier transform, because there is no difference between continuous functions with steep slopes and a real discontinuity when describing such functions by a finite set of points.

3.4 Homogeneous layers

3.4.1 General problem

It is a central assumption of the concept of coordinate transformations in the Fourier modal method that the convergence of the numerical solutions can be improved in the new coordinate system $Ox^1x^2x^3$. This assumption has to be validated individually. One problem is that not every layer converges better in a non-uniform coordinate system $Ox^1x^2x^3$.

For instance, we can derive the solution of a homogeneous layer analytically in an uniform coordinate system $O\check{x}^1\check{x}^2\check{x}^3$, as it is described in section 2.3.4. Even the numerical solution will be correct up to a round-off error in the order of the machine precision, because the involved matrices consist of independent diagonal blocks of maximum size 4×4. However, the matrices are no longer block-diagonal in a complex curvilinear coordinate system $Ox^1x^2x^3$, so that we cannot derive the solution of equation (2.27) analytically in most cases.

It is worth mentioning that only in the limit of an infinite truncation order, the analytical solutions obtained in the uniform system $O\check{x}^1\check{x}^2\check{x}^3$ should coincide with the solutions of equation (2.27) in the curvilinear coordinate system $Ox^1x^2x^3$. For a finite truncation order, the Hilbert space $\check{H}^{N_G}$ spanned by the exact solutions and the Hilbert space H^{N_G} spanned by the solution of equation (2.27) in a truncated curvilinear space will differ. In other words, the Fourier representation of the analytical solutions in the adaptive curvilinear space $Ox^1x^2x^3$ does not reproduce in general the solution of equation (2.27) for a finite truncation order N_G.

The reason for the mismatch between the Hilbert spaces $\check{H}^{N_G}$ and H^{N_G} can be easily explained in the case of one-dimensional structures with adaptive spatial resolution. For the sake of simplicity, $k_1 = k_2 = 0$ and $\zeta = \chi = \xi = 0$, so that the uniform coordinate system for solving equation (2.27) can be chosen orthonormal. As discussed in section 2.3.4, the analytical solutions for homogeneous layers can be chosen as plane waves, which exhibit in the case of one-dimensional structures the functional dependence

$\overline{E}_\alpha^{(\beta,n,0,\pm)}(\overline{x}^1, \overline{x}^2, \overline{x}^3) \propto \exp(iG_{1n}\overline{x}^1 + i\lambda_{n0}^\pm \overline{x}^3)$. Hence, the eigenvalues $\lambda_{n0}^\pm$ correspond to specific harmonics in the uniform coordinate system. On the other hand, the exact transformation of $\overline{E}_\alpha^{(\beta,n,0,\pm)}(\overline{x}^1, \overline{x}^2, \overline{x}^3)$ to the reciprocal space of $Ox^1x^2x^3 = Ox^1\overline{x}^2\overline{x}^3$ yields for this particular example:

$$E_{1pq}^{(1,n,0,\pm)} = \frac{\delta_{q0}}{P} \int_V \frac{\partial \overline{x}^1}{\partial x^1} \overline{E}_1^{(1,n,0,\pm)}(\overline{x}^1, \overline{x}^2, \overline{x}^3) e^{-iG_{1p}x^1} \, dx^1 \,, \tag{3.23a}$$

$$E_{2pq}^{(2,n,0,\pm)} = \frac{\delta_{q0}}{P} \int_V \overline{E}_2^{(2,n,0,\pm)}(\overline{x}^1, \overline{x}^2, \overline{x}^3) e^{-iG_{1p}x^1} \, dx^1 \,. \tag{3.23b}$$

Figure 3.11a depicts the real part of the component $\partial \overline{x}^1/\partial x^1 \overline{E}_1^{(1,n,0,\pm)}$ for $n = 1, 2, 3$. Evidently, these functions exhibit steep slopes, so that the expansion in terms of harmonics $\exp(iG_{1p}x^1)$ requires a sufficient number of higher order harmonics. Figure 3.11b shows the L^2 convergence for the Fourier expansions of different exact solutions in dependence on the truncation order N_G.
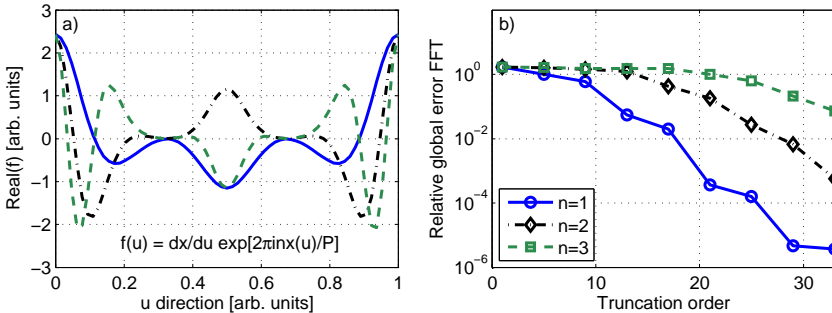
Figure 3.11: One-dimensional example showing real part of analytical solutions for Maxwell's equations in homogeneous layers versus adaptive coordinate u in panel (a). The convergence of the corresponding fast Fourier transform is depicted in panel (b) by the L^2 norm. The parameters of the used adaptive spatial resolution are as in the numerical example described in section 2.6.1. Note that the legend of line styles is valid for both panels.

Obviously, it is a necessary condition for a good convergence of a specific solution $E_\alpha^{(\beta,n,0,\pm)}$ that the truncation order N_G is much larger than $2|n| + 1$. Hence, it is impossible that $\check{H}^{N_G}$ and H^{N_G} span the same subspaces.

The same conclusion can be drawn in the case of two-dimensional structures. In summary, only a few eigenvalues $\lambda_{mn}^\pm$ and eigenvectors $\vec{\mathcal{E}}_{||}^{(\beta,m,n,\pm)}$ corre-

sponding to small spatial harmonics $\exp(iG_{1m}\check{x}^1 + iG_{2n}\check{x}^2)$ converge properly. Fortunately, these solutions are the most important contributions in homogeneous layers, because we can deduce from equation (2.43) that the corresponding eigenvalues $\lambda_{mn}^{\pm}$ usually have a large real and a small imaginary part, so that they can propagate very far along the direction of invariance in these layers. All other solutions are damped rather quickly due to their large imaginary parts.

Still, the difference between the exact solutions of Maxwell's equations in homogeneous layers and the solutions of equation (2.27) obtained in a curvilinear coordinate system may spoil any convergence improvements obtained in other layers. Especially close to the opening of additional diffraction orders, the effect may be large, because a small deviation from the exact solution can cause the plane wave anomaly to appear at the wrong position.

Figure 3.12 depicts the convergence of the numerical eigenvalues λ_{10}^{+} derived by equation (2.27) with matched coordinates for hexagons (diamond symbols), circles (circles), and rotated squares (squares). The corresponding coordinate transformations have been constructed by equations (3.11), (3.13), and (3.20), respectively. The structures are all in a square lattice with a period of 700 nm; the eigenvalues have been calculated for $k_1 = k_2 = 0$ at 1000 meV in panel (a) and 1750 meV in panel (b). Evidently, the convergence is worst for the rotated squares (see figure 3.8b) close to the opening of the first additional diffraction order around 1771 meV. The reason may be the discontinuous coordinate derivatives at the border of the unit cell.
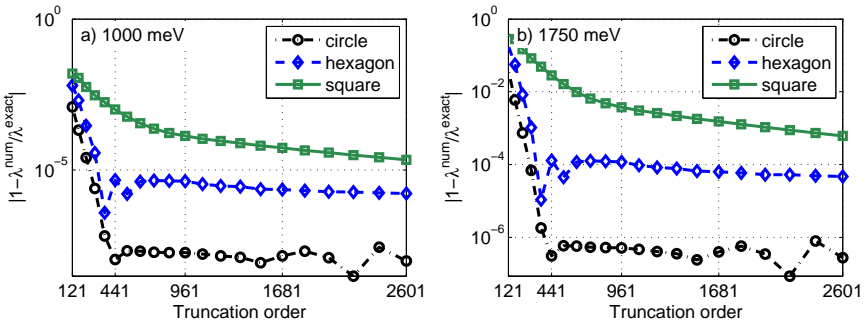
Figure 3.12: Relative deviation between the exact eigenvalues λ_{10}^{+} of homogeneous layers and the numerical solutions of equation (2.27) obtained by using the matched coordinates for hexagons (see figure 3.3a), circles (see figure 3.3b), and rotated squares (see figure 3.8b) at 1000 meV in panel (a) and 1750 meV in panel (b). The material of the homogeneous layer is vacuum.

3.4.2 Replacement of far field channels

There is an ongoing discussion on how to treat the eigenvalue equation (2.27) appropriately in an adaptive non-uniform coordinate system [11, 111–113]. Especially, the efficient and accurate treatment of the homogeneous layers has drawn a lot of attention. However, it is beyond the scope of this work to discuss this problem in greater detail due to the following reasons.

Firstly, we do not know a straight-forward application of the reformulations discussed by Guizal et. al [111] to the concept of coordinate transformations in two-dimensional systems and a general proof for the superiority of this reformulation is missing.

Secondly, we have made so far very good experience with the approach discussed in the original paper on two-dimensional adaptive spatial resolution [13], namely to replace the solution of those channels that allow light to propagate to the far field by the expansion of the exact solutions in terms of the harmonics of the adaptive coordinate system $Ox^1x^2x^3$. Thus, we not only warrant an accurate convergence of the far field spectra, but we also get rid of any problems with a potential eigenvalue degeneracy. In such a case, any linear combination of eigenvectors corresponding to the same eigenvalue provides another solution to the same eigenvalue. Hence, the numerical solution of equation (2.27) does not necessarily correspond to a plane wave expansion, which is in turn a fundamental assumption for the derivation of the far field spectra in section 2.4.3. Therefore, we must be able to construct the plane wave expansion in terms of the adaptive harmonics at least for the open far field channels.

If $\check{F}_\beta$ denotes the β component of an exact solution of the electric or magnetic field in the uniform coordinate system $O\check{x}^1\check{x}^2\check{x}^3$, we can construct its equivalent solution in the adaptive non-uniform coordinate system $Ox^1x^2x^3$ by the following Fourier transform:

$$F_{\alpha m n} = \frac{1}{V} \int\limits_V \frac{\partial \check{x}^\beta}{\partial x^\alpha} \check{F}_\beta \, e^{-iK_{1m}x^1 - iK_{2n}x^2} \, \mathrm{d}x^1 \mathrm{d}x^2 \,. \tag{3.24}$$

In practical applications, we choose the exact solutions as a plane wave expansion, for which the reciprocal representation of the lateral electric field components can be written as

$$\check{E}_\alpha^{(\beta,m,n,\pm)} = e^{iK_{1m}\check{x}^1 + iK_{2n}\check{x}^2 + iK_{3mn}^\pm \check{x}^3} \delta_\alpha^\beta \,, \tag{3.25}$$

with $\alpha, \beta = 1, 2$. The divergence condition (2.65) provides the third component of the respective fields:

$$\check{E}_3^{(\beta,m,n,\pm)} = \mp \left(\frac{K_m^1}{K_{mn}^3} \delta_1^\beta + \frac{K_n^2}{K_{mn}^3} \delta_2^\beta \right) e^{iK_{1m}\check{x}^1 + iK_{2n}\check{x}^2 + iK_{3mn}^\pm \check{x}^3} \,. \tag{3.26}$$

The transformation of these electric fields to the reciprocal space of the adaptive curvilinear coordinate system $Ox^1x^2x^3$ yields

$$E_{\alpha pq}^{(1,m,n,\pm)} = \frac{1}{V} \int\limits_V \left(\frac{\partial \check{x}^1}{\partial x^\alpha} \mp \frac{K_m^1}{K_{mn}^3} \frac{\partial \check{x}^3}{\partial x^\alpha} \right) e^{iK_{1m}\check{x}^1 + iK_{2n}\check{x}^2 + iK_{3mn}^\pm \check{x}^3}$$

$$\times\, e^{-iK_{1p}x^1 - iK_{2q}x^2}\, \mathrm{d}x^1 \mathrm{d}x^2 \ , \tag{3.27}$$

$$E_{\alpha pq}^{(2,m,n,\pm)} = \frac{1}{V} \int\limits_V \left(\frac{\partial \check{x}^2}{\partial x^\alpha} \mp \frac{K_n^2}{K_{mn}^3} \frac{\partial \check{x}^3}{\partial x^\alpha} \right) e^{iK_{1m}\check{x}^1 + iK_{2n}\check{x}^2 + iK_{3mn}^\pm \check{x}^3}$$

$$\times\, e^{-iK_{1p}x^1 - iK_{2q}x^2}\, \mathrm{d}x^1 \mathrm{d}x^2 \ . \tag{3.28}$$

The exact solution of the magnetic fields can be found from equation (2.45) as follows:

$$\begin{bmatrix} \check{H}_1^{(1,m,n,\pm)} \\ \check{H}_2^{(1,m,n,\pm)} \end{bmatrix} = \pm \frac{e^{iK_{1m}\check{x}^1 + iK_{2n}\check{x}^2 + iK_{3mn}^\pm \check{x}^3}}{k_0\mu K_{mn}^3} \begin{pmatrix} -k_0^2\varepsilon\mu\tilde{g}^{21} - K_{1m}\tilde{g}^{33}K_{2n} \\ k_0^2\varepsilon\mu\tilde{g}^{11} - K_{2n}\tilde{g}^{33}K_{2n} \end{pmatrix} , \tag{3.29}$$

$$\begin{bmatrix} \check{H}_1^{(2,m,n,\pm)} \\ \check{H}_2^{(2,m,n,\pm)} \end{bmatrix} = \pm \frac{e^{iK_{1m}\check{x}^1 + iK_{2n}\check{x}^2 + iK_{3mn}^\pm \check{x}^3}}{k_0\mu K_{mn}^3} \begin{pmatrix} -k_0^2\varepsilon\mu\tilde{g}^{22} + K_{1m}\tilde{g}^{33}K_{1m} \\ k_0^2\varepsilon\mu\tilde{g}^{12} + K_{2n}\tilde{g}^{33}K_{1m} \end{pmatrix} . \tag{3.30}$$

In this case, the terms $\tilde{g}^{\alpha\beta}$ evolve from the application of the operator $\hat{l}_3^-$ [see equation (2.20)] on the metric tensor $\sqrt{g}g^{\alpha\beta}$. Similar to the electric field, the divergence condition for the magnetic field provides the respective third component:

$$\check{H}_3^{(\beta,m,n,\pm)} = \mp \frac{K_m^1}{K_{mn}^3} \check{H}_1^{(\beta,m,n,\pm)} \mp \frac{K_n^2}{K_{mn}^3} \check{H}_2^{(\beta,m,n,\pm)} \propto e^{iK_{1m}\check{x}^1 + iK_{2n}\check{x}^2 + iK_{3mn}^\pm \check{x}^3} . \tag{3.31}$$

Hence, the spatial representation of the exact magnetic field yields in the adaptive coordinate system $Ox^1x^2x^3$

$$H_\alpha^{(\beta,m,n,\pm)} = \left(\frac{\partial \check{x}^1}{\partial x^\alpha} \mp \frac{K_m^1}{K_{mn}^3} \frac{\partial \check{x}^3}{\partial x^\alpha} \right) \check{H}_1^{(\beta,m,n,\pm)} + \left(\frac{\partial \check{x}^2}{\partial x^\alpha} \mp \frac{K_n^2}{K_{mn}^3} \frac{\partial \check{x}^3}{\partial x^\alpha} \right) \check{H}_2^{(\beta,m,n,\pm)} . \tag{3.32}$$

Abbreviating equations (3.29) and (3.30) as

$$\check{H}_\alpha^{(\beta,m,n,\pm)} = \check{h}_{\alpha mn}^{\beta\pm} e^{iK_{1m}\check{x}^1 + iK_{2n}\check{x}^2 + iK_{3mn}^\pm \check{x}^3} , \tag{3.33}$$

we derive for the expansion of the exact magnetic field in terms of the harmonics of the adaptive coordinate system $Ox^1x^2x^3$:

$$H_{\alpha pq}^{(\beta,m,n,\pm)} = \check{h}_{1mn}^{\beta\pm} E_{\alpha pq}^{(1,m,n,\pm)} + \check{h}_{2mn}^{\beta\pm} E_{\alpha pq}^{(2,m,n,\pm)} . \tag{3.34}$$

In order to warrant a stable numerical algorithm for the derivation of the far field spectra according to section 2.4.3, all solutions for equation (2.27) that correspond to open far field channels should be replaced by the exact solutions using equations (3.27) and (3.28) as well as equation (3.34).

Note that we recommend to replace only a few properly converged eigenvectors, not all of them. Otherwise, one would introduce elements in the Fourier modal method that are not a proper solution of equation (2.27). Thus, the boundary conditions at the border of two stacked layers may be spurious.

3.4.3 Material and energy dependence of solutions for homogeneous layers

The numerical solution of equation (2.27) in homogeneous layers causes not only a stability problem in the derivation of the far fields when using matched coordinates, but it also leads to an increased calculation time compared to calculations in an uniform coordinate system, where we can use the analytical solution derived in section 2.3.4.

For the stability issue, we recommend to replace the open channels by the exact solutions, as discussed in subsection 3.4.2. Regarding the calculation time, we extended the approach by Yala et al. [112], which suggests to obtain the numerical solution of homogeneous layers only once and to use it for the derivation of the solution in all other homogeneous layers with the same incidence parameters. In addition, we proposed to use the solution also at different energies in the case that k_1 and k_2 as the in-plane projections of the incident wave vector are kept constant [14].

First of all, the analytic eigenvector solution in homogeneous layers does not depend on the energy when fixing k_1 and k_2. Second, the square of the contravariant eigenvector components K_{mn}^3 defined by equation (2.42) contains for fixed k_1 and k_2 only one term that depends on the energy and the material parameters ε and μ, namely $g^{33}k_0^2\varepsilon\mu$. Thus,

$$
\begin{aligned}
\left(K_{mn}^3\right)^2 - g^{33}k_0^2\varepsilon\mu = {}& -g^{33}\left[(K_{1m})^2 g^{11} + (K_{2n})^2 g^{22} + 2K_{1m}K_{2n}g^{12}\right] \\
& + \left(K_{1m}g^{13} + K_{2n}g^{23}\right)^2 \equiv f(k_1, k_2),
\end{aligned}
\tag{3.35}
$$

with f as a function that is independent on the energy and the material parameters.

When describing homogeneous layers in non-uniform coordinate systems, we assume now that the numerical solution of equation (2.27) exhibits for different energies and materials an identical systematic error, so that the eigenvector matrix $\mathcal{F}_{\parallel\,\mathrm{homo}}$ of one set of k_0, ε, and μ diagonalizes equation (2.27) for all other sets of k_0, ε, and μ. Furthermore, we can construct a K_n^3, which is related

with $K_{3n}^{\pm}$ via equation (2.43).[2] For such a K_n^3 in non-uniform coordinates, it seems to be reasonable to assume that $\left(K_n^3\right)^2 - g^{33}k_0^2\varepsilon\mu$ is also independent on the energy and the material parameters.

At least for the coordinate systems with $g^{\alpha 3} = g^{3\alpha} = 0$ for $\alpha = 1, 2$, we can circumstantiate this hypothesis [14]. In this case, $K_{3n}^{\pm} = \pm K_n^3/g^{33}$, and we can determine K_n^3/g^{33} as eigenvalues of equation (2.31). In particular,

$$\left(\frac{K_n^3}{g^{33}}\right)^2 \vec{\mathcal{E}}_{\|\,n}^{\pm} = -\frac{\varepsilon}{\mu}\hat{\mathcal{L}}^2(\tilde{\mu}, \tilde{\varepsilon})\vec{\mathcal{E}}_{\|\,n}^{\pm}. \tag{3.36}$$

The matrix operator on the right side of equation (3.36) can be written as follows:

$$\frac{\varepsilon}{\mu}\hat{\mathcal{L}}^2(\tilde{\mu}, \tilde{\varepsilon}) = \frac{1}{k_0^2\varepsilon\mu}\left[k_0^2\varepsilon\mu \underbrace{\begin{pmatrix} -\tilde{\mathcal{G}}^{21} & -\tilde{\mathcal{G}}^{22} \\ \tilde{\mathcal{G}}^{11} & \tilde{\mathcal{G}}^{12} \end{pmatrix}}_{\equiv\,\mathcal{A}} + \underbrace{\begin{pmatrix} -\mathcal{K}_1\tilde{\mathcal{G}}^{33}\mathcal{K}_2 & \mathcal{K}_1\tilde{\mathcal{G}}^{33}\mathcal{K}_1 \\ -\mathcal{K}_2\tilde{\mathcal{G}}^{33}\mathcal{K}_2 & \mathcal{K}_2\tilde{\mathcal{G}}^{33}\mathcal{K}_1 \end{pmatrix}}_{\equiv\,\mathcal{B}}\right]^2. \tag{3.37}$$

Here, $\tilde{\mathcal{G}}^{\alpha\beta}$ are the tensor elements evolving from the application of $\hat{l}_3^-$ on the Fourier representation of the metric tensors $\sqrt{g}g^{\alpha\beta}$, with $\hat{l}_3^-$ defined by equation (2.20).

Assuming that $\tilde{\mathcal{G}}^{\alpha\beta} = \tilde{\mathcal{G}}^{\beta\alpha}$ and $\tilde{\mathcal{G}}^{\alpha\beta}\tilde{\mathcal{G}}^{\gamma\delta} = \tilde{\mathcal{G}}^{\gamma\delta}\tilde{\mathcal{G}}^{\alpha\beta}$ as in the case of the respective spatial representations, it is straight-forward to show that

$$\mathcal{A}^2 = -\frac{1}{g^{33}}\mathcal{I}, \qquad \mathcal{B}^2 = 0, \tag{3.38}$$

where $\mathcal{I}$ denotes an unit matrix. Hence, we can reformulate equation (3.36) as follows:

$$\underbrace{\left[\left(\frac{K_n^3}{g^{33}}\right)^2 - \frac{k_0^2\varepsilon\mu}{g^{33}}\right]}_{\equiv\,\sigma_n}\vec{\mathcal{E}}_{\|\,n}^{\pm} = -(\mathcal{A}\mathcal{B} + \mathcal{B}\mathcal{A})\vec{\mathcal{E}}_{\|\,n}^{\pm}. \tag{3.39}$$

As neither $\mathcal{A}$ nor $\mathcal{B}$ depend on the energy or the material constants ε and μ, the redefined eigenvalues σ_n must also be independent on the energy and the material parameters. Hence, $\vec{\mathcal{E}}_{\|\,n}^{\pm}$ should be a solution for all homogeneous layers with the same in-plane wave vector components k_1 and k_2, and we can calculate the eigenvalues σ_n for any homogeneous layer by the condition

$$\sigma_n(k_0, \varepsilon, \mu) = \sigma_{\text{ref}}, \tag{3.40}$$

---

[2]In the case of homogeneous layers in non-uniform coordinates, we label eigenvalues and eigenvectors by a single integer n in order to avoid the impression that it is possible to identify for all solutions of equation (2.27) in a truncated Fourier space a corresponding analytic result in an uniform coordinate system.

where σ_{ref} has been derived as the solution for a reference layer. It should be emphasized that this relation is only valid in cases where k_1 and k_2 are fixed as the incidence parameters. If we fix the incident angles θ and ϕ (see figure 2.2a) in analogy to a given experiment, k_1 and k_2 vary with the incidence energy.

Note that condition (3.38) is fulfilled only approximatively in numerical calculations. Hence, equation (3.40) provides also only approximate solutions for the eigenvalues. However, the deviation is more or less negligible over a wide energy range. Figure 3.13 depicts the relative deviation between solving equation (2.27) for all energies and using equation (3.40) for a reference energy of $1000\,\mathrm{meV}$. The calculations have been carried out for the examples described in section 3.5.1, 3.5.2, and 3.5.3. In the case of the latter, the transformation for the rotated square has been derived via equation (3.20) using function h_2 (see section 3.2.2).
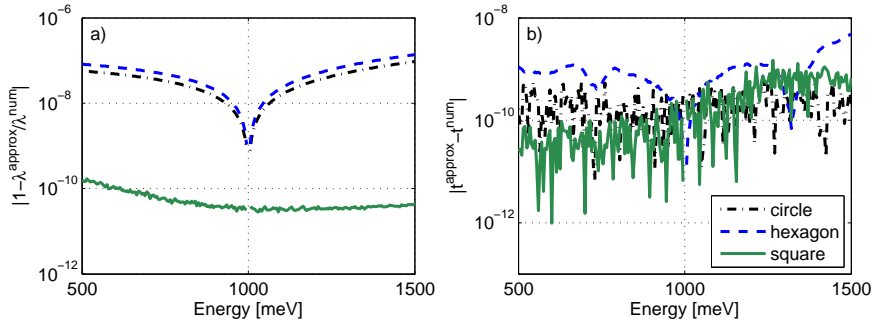
Figure 3.13: Comparison between results obtained by solving equation (2.27) in all layers numerically and approximating the solutions for homogeneous layers by equation (3.40) for a reference energy of $1000\,\mathrm{meV}$ in the case of (a) the eigenvalues as mean value and (b) the zeroth order transmission spectra. The different curves show a periodic array of gold cylinders as defined in section 3.5.1 (dashed-dotted lines), hexagons as defined in section 3.5.2 (dashed lines), and rotated squares as defined in section 3.5.3 (solid lines).

Both the mean value of the relative eigenvalue deviation as well as the relative difference in the zeroth order transmission[3] remain rather small for the chosen truncation order of 25×25 harmonics over the whole energy range. Especially in the case of the far field spectra, the deviation is mainly on the level of numerical noise.

---

[3]Zeroth order transmission means input and output in the fundamental harmonic.

3.5 Numerical examples

Except for figure 3.13b, the previous examples have been purely dielectric, and one may be able to derive a good accuracy at reasonable computational cost also without the concept of matched coordinates. In the following, we are going to present results for gold structures, where we expect a derivation of appropriate results only with the concept of matched coordinates.

For all the following examples, we have chosen a spatial grid of 1024×1024 points, with the interfaces located everywhere between two grid lines. Except for the calculations with standard adaptive spatial resolution, we have computed the occurring derivatives $\partial \overline{x}^{\alpha}/\partial x^{\beta}$ numerically. In the case of the standard adaptive spatial resolutions, we were able to use the corresponding analytical expressions. From $\partial \overline{x}^{\alpha}/\partial x^{\beta}$, it is straight-forward to construct $\partial x^{\alpha}/\partial \overline{x}^{\beta}$ for equation (2.6). Finally, we carried out a fast Fourier transform using the correct rules of Fourier factorization.

Note that all examples have been calculated by approximating the eigenvalues of homogeneous layers according to equation (3.40), unless the opening of an additional far field channel has been reached.

In the system of matched coordinates with adaptive spatial resolution, we have chosen a resolution parameter $\eta = 0.999$ [see equation (2.81)], and an equal distance between neighboring interfaces in agreement with our experience with the standard adaptive spatial resolution. Thus, the structures of interest fill 25% of the unit cell.

3.5.1 Gold cylinders

Let us first compare the convergence between matched coordinates and a zig-zag approximation in the case of a periodic array of round gold cylinders in a square lattice configuration. The system of matched coordinates has been constructed according to equation (3.13).

The geometry parameters are taken from reference [14], with a period of 700 nm and a radius of 250 nm. The gold cylinders are surrounded by vacuum; the height of the cylinders is 30 nm. As in the case of [14], we describe the gold permittivity by the analytic model introduced by Etchegoin et al. [114], the permeability is set to 1. A sketch of the periodic array of gold cylinders can be seen in figure 3.1a.

Figure 3.14a depicts the far field spectra for the given geometry at normal incidence. We observe a broad resonance around 1240 meV, with a minimum in transmittance (solid line) and a maximum in reflectance (dashed line) and absorbance (dashed-dotted line). Furthermore, the opening of the first additional far field channels can be seen around 1780 meV. Black lines denote the results obtained with adaptive spatial resolution and matched coordinates for

a truncation order of 25×25 harmonics, whereas the results of the zig-zag approximation are indicated by blue lines for a truncation order of 35×35. Although the truncation order has been chosen much larger in the case of the zig-zag approximation, the spectra still exhibit a spurious oscillating behavior, manifested in small oscillations that can be assumed to be spurious extra resonances.
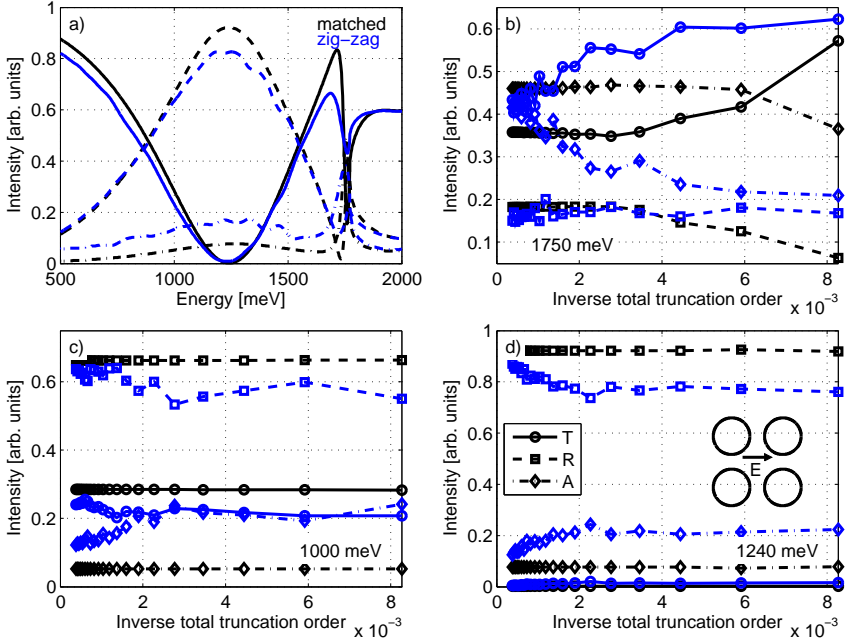

Figure 3.14: Example of an array of round gold cylinders in a square lattice configuration at normal incidence. Black color denotes matched coordinates, blue lines indicate a zig-zag approximation. Panel (a) depicts the far field spectra in transmittance (solid line), reflectance (dashed line), and absorbance (dashed-dotted line). The convergence behavior is shown in panels (b-d) versus inverse truncation order at 1750 meV in panel (b), 1000 meV in panel (c), and 1240 meV in panel (d). Note that the legend of line styles is valid for all panels.

The convergence behavior of transmittance, reflectance, and absorbance can be seen in panels (b-d) of figure 3.14 for different energies and truncation orders between 11×11 and 51×51 (2601 harmonics in total) at normal incidence. Similar to the results of reference [81], we observe a very good convergence with matched coordinates and adaptive spatial resolution, whereas the zig-

zag approximation exhibits a tendency towards the results of the matched coordinates, but converges rather slowly. Essig and Busch have investigated the convergence behavior of the zig-zag lines even up to a total truncation order of 23993 harmonics via symmetry considerations [81], with the same qualitative result that both zig-zag lines and matched coordinates seem to converge to the same values.

In the presented example, the worst convergence behavior can be observed in 3.14b at 1750 meV, close to the opening of the additional far field channels. At energies below the resonance (see figure 3.14c) and at the resonance (see figure 3.14d), the convergence behavior is much better. In all three cases, we can achieve convincing convergence with matched adaptive coordinates starting from a truncation order of 17×17 harmonics.
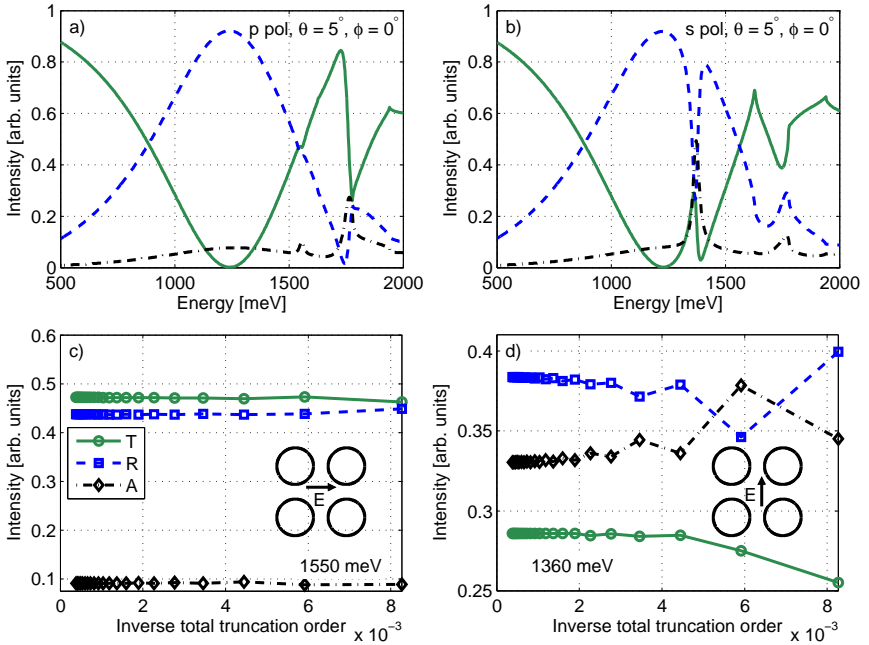
Figure 3.15: Array of gold cylinders as in figure 3.14, but for incidence angles $\theta = 5°$ and $\phi = 0°$. Panels (a) and (c) show p polarization, (b) and (d) s polarization. The upper row depicts the far field spectra in transmittance (solid green line), reflectance (dashed blue line), and absorbance (dashed-dotted black line). The convergence behavior is shown in (c) for 1550 meV and in (d) for 1360 meV. The insets in the lower panels denote the orientation of the incident electric field.

With the concept of matched coordinates, we can of course also derive spectra for inclined incidence. Figure 3.15a and 3.15b depict the far field spectra in p and s polarization, respectively, with adaptive spatial resolution and matched coordinates for incidence angles $\theta = 5°$ and $\phi = 0°$ (see figure 2.2a for the definition of θ and ϕ). In addition to the broad resonance seen in figure 3.14a, two sharp features appear; an additional resonance in s polarization around 1360 meV, and another resonance around 1550 meV in p polarization.

We have chosen these additional resonances in order to calculate the convergence behavior with matched coordinates in s and p polarization for inclined incidence. The results are depicted in figure 3.15c for p polarization and figure 3.15d for s polarization and reflect in general very well the behavior at normal incidence. Only the spectra in s polarization converge a little bit worse. Due to the similar convergence behavior, we are going to focus henceforth on calculations with normal incidence.

3.5.2 Gold hexagons

The concept behind the coordinate transformation defined in equation (3.11) for hexagonal structures is almost identical to that behind the transformation matching round cylinders [see equation (3.13)]. Hence we chose the test system for the hexagonal structures similar to the previous example of round cylinders.

The unit cell has a size of 700 nm × 700 nm and is filled with an equilateral gold hexagon with an edge length of 250 nm and a thickness of 30 nm (see figure 3.2b). The gold is described by the analytic method of reference [114], the hexagons are surrounded by vacuum.

As in the case of the gold cylinders, we combine the concept of matched coordinates with adaptive spatial resolution. The corresponding coordinate transformation can be seen in figure 3.3a. The main difference between the gold cylinders and the gold hexagons is that the gold cylinders are isotropic at normal incidence, whereas we can expect different results for orthogonal incidence polarizations in the case of the hexagons.

Figure 3.16a depicts the far field spectra of the gold hexagons at normal incidence with the incident electric field aligned along the x direction. The resonance position is very similar to the array of round gold cylinders. As in figure 3.14a, blue color denotes results obtained by a zig-zag approximation of the hexagons for a truncation order of 35×35 harmonics, whereas the spectra in black have been derived with adaptive spatial resolution and matched coordinates for a truncation order of 25×25 harmonics.

Evidently, the far field spectra still exhibit numerical artifacts using the zig-zag approximation at the presented truncation order, whereas the results with matched coordinates look reasonable. The convergence plots in panels (b-d) of
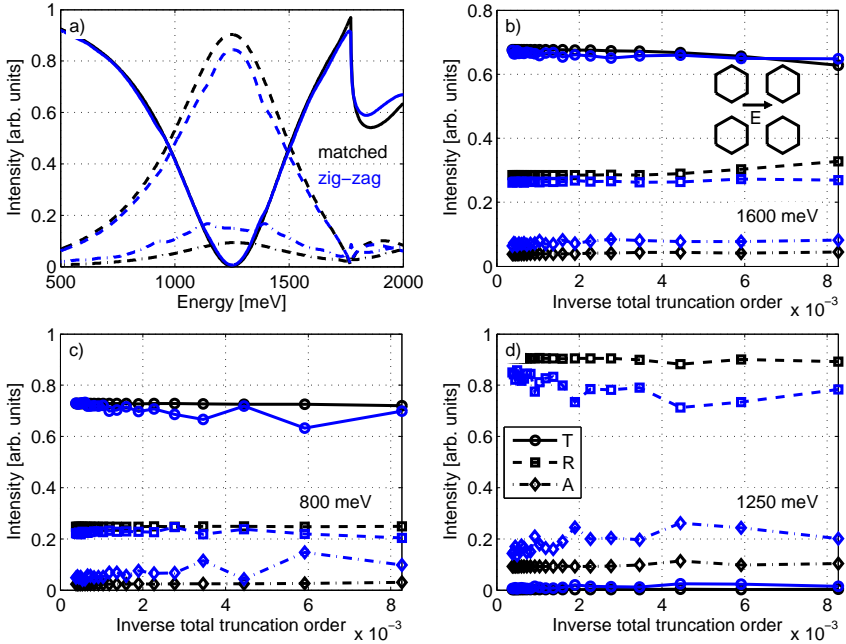
Figure 3.16: Transmittance (solid lines), reflectance (dashed lines), and absorbance (dashed-dotted lines) in the case of a periodic array of gold hexagons with the incident electric field aligned along the x direction [see inset in panel (b)]; panel (a) depicts the far field spectra, whereas panels (b-d) show the convergence behavior at different energies for truncation orders between 11×11 and 51×51 harmonics. Black color denotes results obtained with matched coordinates and adaptive spatial resolution as described by equation (3.11), whereas the results shown by blue color have been obtained by a zig-zag approximation.

figure 3.16 confirm this observation. The behavior is similar to the gold cylinders; the zig-zag approximation approaches the results with matched coordinates for very large truncation orders, whereas the calculations with matched coordinates exhibit only fluctuations on a small scale for the different truncation orders at all three energies.

For the sake of completeness, we display in figure 3.17 also the results for the case where the incident electric field is aligned along the y direction. Obviously, the results are more or less identical to figure 3.16. We observe in figure 3.17a a broad resonance around $1250\,\mathrm{meV}$, which is better described by the calculations with matched coordinates for a truncation order of 25×25 harmonics

than with the zig-zag approximation and a truncation order of 35×35 harmonics. Also, the convergence behavior is close to the orthogonal polarization of figure 3.16 with a superior convergence behavior using matched coordinates and adaptive spatial resolution. In contrast to figure 3.16, the convergence of the zig-zag approximation seems to be worse, especially in figure 3.17b for an energy of 1600 meV close to the opening of the additional far field channels.
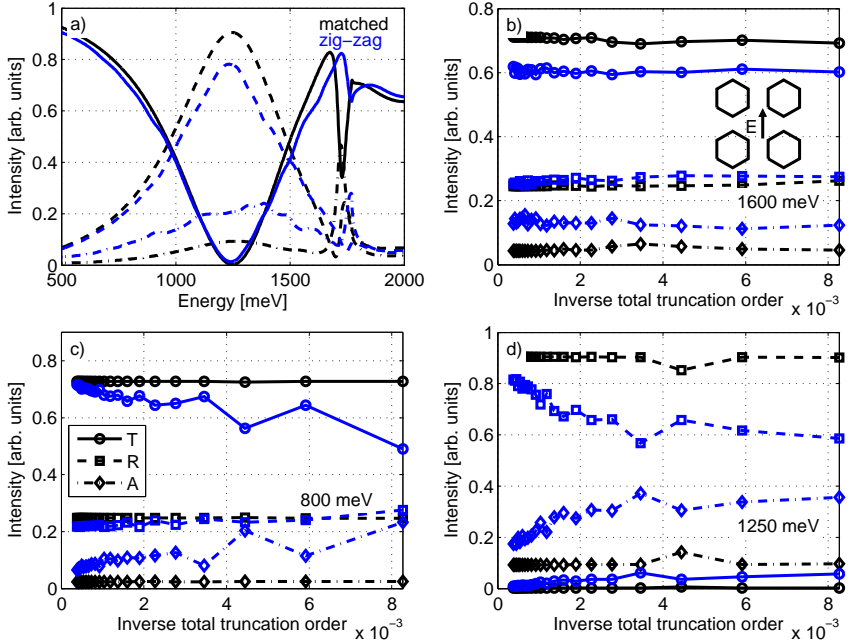
Figure 3.17: Results of transmittance (solid lines), reflectance (dashed lines), and absorbance (dashed-dotted lines) for the same structure as in figure 3.16, but with the incident electric field aligned along the y axis [see inset in panel(b)].

Because of the inferior convergence behavior of calculations with the zig-zag approximation, we will henceforth refrain from the results obtained by this approximation and focus on alternative validations for the scheme of matched coordinates.

3.5.3 Rotated gold squares

In section 3.2, we have derived several possible coordinate transformations matching a system with rotated rectangles, which allows us a comparison of

the different approaches.

Firstly, we have the scheme of smooth modulation described in section 3.2.1, where we can choose the intermediate areas such that we either have everywhere continuous coordinate derivatives (see figure 3.18a) or connect neighboring rectangles via straight lines (see figure 3.18c). Henceforth, we are going to refer to these transformations as *type A smooth* and *type A straight*, respectively.
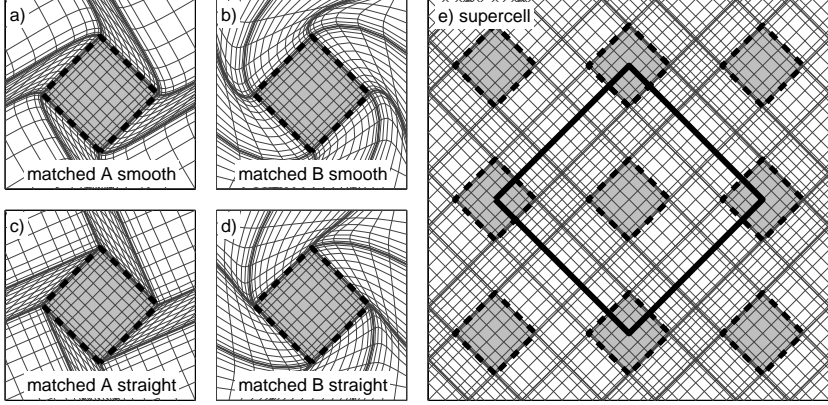
Figure 3.18: Different coordinate systems for the calculation of a square rotated by $45°$ in a quadratic unit cell; (a) and (c) are obtained by the scheme of smooth modulation described in section 3.2.1 with smoothly curved coordinates in (a) and simply straight lines in (c), whereas (b) and (d) have been constructed via equation (3.20) using functions h_2 and h_1, respectively. Alternatively, the rotated squares can be calculated for this particular geometry by the standard Fourier modal method with adaptive spatial resolution, when considering a supercell with two square elements per unit cell, as depicted in panel (e). A possible unit cell is indicated by the solid black lines.

Secondly, we can use the approach described in section 3.2.2, where we can also obtain lines that exhibit continuous coordinate derivatives at the interfaces (see figure 3.18b). This transformation requires a strong deformation of the unit cell, so that it is questionable, whether we should not overcome the restriction of smooth derivatives, as depicted in figure 3.18d. We will refer to transformations according to section 3.2.2 as *type B*.

In addition, we can compare the rotated structures with the standard Fourier modal method including adaptive spatial resolution in the case of specific rotation angles. For instance, a rotation by $45°$ can be described by calculating

a supercell with two elements per unit cell (see figure 3.18e). Hence, the system of rotated squares is ideal for testing the influence of the underlying coordinate system on the convergence behavior.

We have chosen to keep the unit cell size $700\,\text{nm} \times 700\,\text{nm}$ as in the previous examples described in sections 3.5.1 and 3.5.2. The rotated elements are gold squares in vacuum with a side length of $300\,\text{nm}$ and a thickness of $30\,\text{nm}$ (see figure 3.1c). As for the hexagons and the cylinders, we describe the gold by the model provided in reference [114].

Figure 3.19a depicts the corresponding far field spectra obtained by transformation type A with smooth coordinate lines for a truncation order of 25×25 harmonics. The incidence is normal with the incident electric field aligned along the x axis. We observe a resonance around $1300\,\text{meV}$, which is narrower than in the case of the gold cylinders or hexagons.
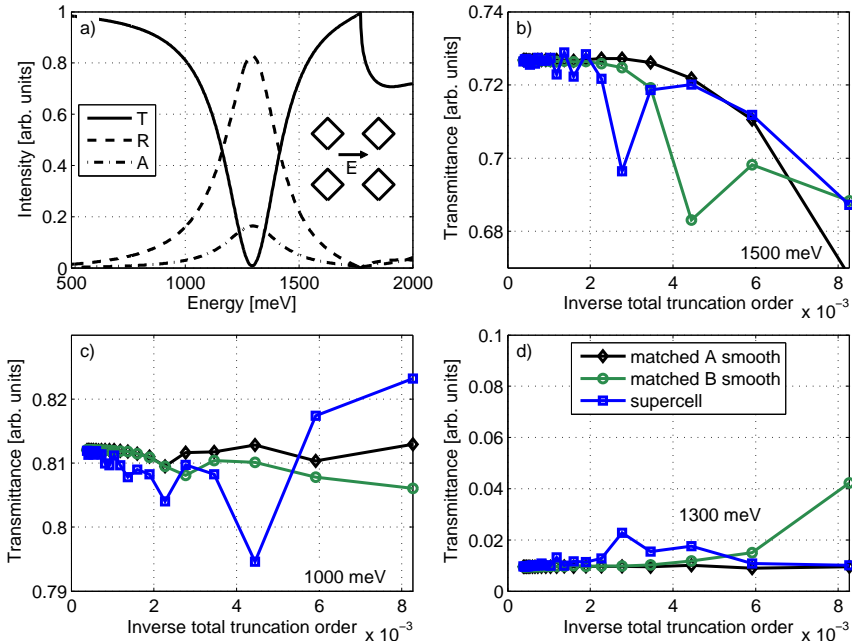
Figure 3.19: Comparison of different approaches for the description of a periodic array of rotated squares as depicted in figure 3.18. Panel (a) shows the far field spectra at normal incidence, with transmittance (solid lines), reflectance (dashed lines), and absorbance (dashed-dotted lines). The convergence behavior of the different approaches is depicted by the transmittance in panels (b-d) at different energies.

The comparison of the convergence behavior between the supercell as well as transformation types A and B with continuous coordinate derivatives at the interfaces is depicted in panels (b-d) of figure 3.19 at three different energies. As it can be seen, all approaches converge to the same values, but transformation type A exhibits the best convergence behavior. Especially at 1500 meV, transformation type B is only slightly better than the supercell. Evidently, the strong deformation of the unit cell in combination with the discontinuous coordinate derivatives at the border of the unit cell is inferior to transformation type A, but the results are still better than those of the supercell.

It is worth mentioning that the general convergence behavior of the rotated squares is similar to the examples of the gold hexagons and the gold cylinders described in the previous sections 3.5.1 and 3.5.2. Note that the scale of the convergence plots in figure 3.19 is much smaller than in figures 3.14 to 3.17.

Now, we want to address the question whether it is superior to have continuous coordinate derivatives at all material interfaces. This question is of great importance, because it is in general more challenging to construct transformations with continuous derivatives $\partial \overline{x}^\alpha / \partial x^\beta$.

In figure 3.20, we compare the transmittance at 1500 meV for both transformation types A and B. In the case of transformation type A, it seems that the system with continuous coordinate derivatives is superior compared to the straight lines. This underlines the intuitive assumption that smooth coordinate transformations are superior.
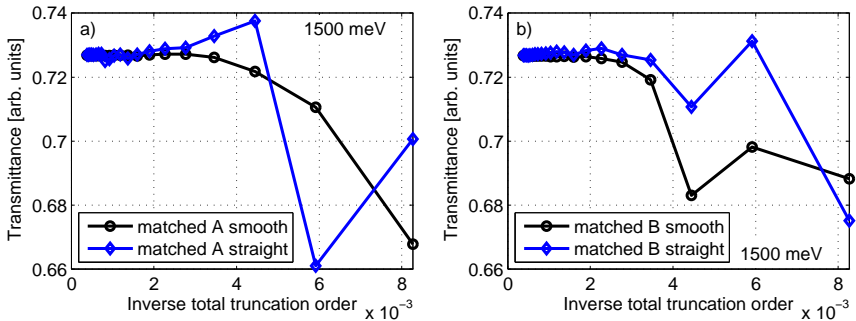
Figure 3.20: Comparison of transmittance between transformations with (black curves) and without (blue curves) continuous coordinate derivatives at the material interfaces. The transmittance has been computed at 1500 meV for normal incidence using the coordinate transformation of type A in panel (a) and type B in panel (b).

For the transformation type B, the difference with and without continuous coordinate derivatives is more or less negligible. We observe only a slight

improvement by the straight coordinates obtained by using function h_1 in equation (3.20), which may be attributed to a reduced deformation of the unit cell.

3.5.4 Magneto-optical waveguide structure

So far, the presented examples contained merely isotropic permittivity and permeability values. Therefore, we provide in this section an example with an anisotropic permittivity tensor $\bar{\bar{\varepsilon}}$.

The example is taken from a paper by Belotelov et al. [54] and consists of a gold film with quadratic air holes and a thickness of 68 nm on top of a magneto-optical waveguide layer of thickness 118 nm. The unit cell size is 750 nm × 750 nm, the hole diameter is 395 nm. The top and the bottom layers of the structure are filled with air.
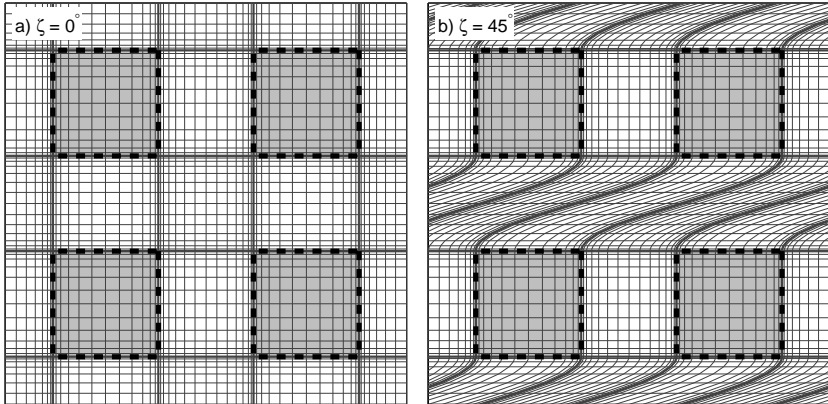
Figure 3.21: (a) Standard adaptive coordinate system for the calculation of quadratic shapes in a square lattice configuration. (b) Inclined coordinate system with an inclination angle of 45° that describes the same system as in (a).

The gold is described by a Drude model (see section 2.7) with $\epsilon_\infty = 7.9$, $\omega_P = 8770$ meV, and $\gamma = 1.13 \times 10^{14}$ rad/s. The magneto-optical waveguide consists of a material with the permittivity tensor

$$\bar{\bar{\varepsilon}} = \begin{pmatrix} \varepsilon_{\mathrm{wg}} & -ig & 0 \\ ig & \varepsilon_{\mathrm{wg}} & 0 \\ 0 & 0 & \varepsilon_{\mathrm{wg}} \end{pmatrix},$$
(3.41)

with $\varepsilon_{\mathrm{wg}} = 5.5 + 0.0025i$, and $g = (1 - 0.15i) \times 10^{-2}$. The parameters are taken from reference [54].
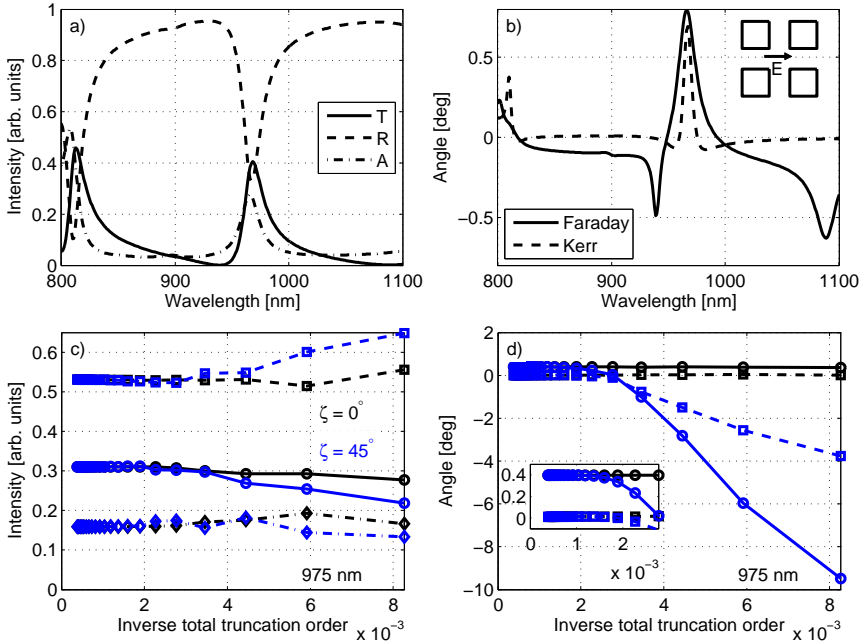
Figure 3.22: Results of a magneto-optical waveguide structure covered with a gold film. The gold film contains quadratic air holes in a square lattice configuration. The upper row depicts far field spectra in panel (a) as well as the Faraday and Kerr rotation angles in panel (b), derived by the standard Fourier modal method with adaptive spatial resolution at normal incidence. Due to the square lattice, we can compare these results with those calculated with matched coordinates in an inclined coordinate system for an inclination angle of $\zeta = 45°$ and $P^2 = \sqrt{2}P^1$ (see figure 3.21b). The corresponding convergences behavior can be seen for the far field spectra in panel (c) and for the rotation angles in panel (d), derived at 975 nm. Note that the legends in panels (a) and (b) are also valid for panels (c) and (d), respectively.

Such a magneto-optical structure exhibits non-vanishing Faraday and Kerr rotations. These properties can be derived from the polarization ellipse [93], which results from the s and p polarized output of the small scattering matrix (see section 2.4.4). In the work of Belotelov, it is shown that the Faraday and Kerr rotation can be enhanced by tuning the interplay of plasmonic resonances and waveguide modes. We are going to reproduce Belotelov's results

using the classical Fourier modal method with adaptive spatial resolution (see figure 3.21a) as well as an inclined coordinate system with inclination angle $\zeta = 45°$ (see figure 3.21b). By choosing the period $P^2 = \sqrt{2}P^1$ with $P^1 = 750$ nm in the case of the inclined coordinate system, we obtain again a square lattice configuration. Of course, nobody will carry out the calculation of a square lattice using the inclined coordinate system, but it is a good test case for the convergence of derived quantities such as the Faraday and Kerr angle in an inclined coordinate system, because we can compare the results with the standard calculation without inclination.

Figure 3.22 depicts the far field spectra of the magneto-optical waveguide in panel (a) at normal incidence. The calculations have been carried out with the standard Fourier modal method and adaptive spatial resolution for a truncation order of 25×25 harmonics. The corresponding Faraday and Kerr angles are shown in panel (b). Both the spectra and the rotation angles exhibit a very good agreement with reference [54].

At a wavelength of 975 nm, we show the convergence behavior of the far field spectra in figure 3.22c; the results for the rotation angles are depicted in figure 3.22d. Black color denotes the standard calculation without inclination and equal periods $P^1 = P^2$; the results with an inclination angle of $45°$ and $P^2 = \sqrt{2}P^1$ are shown by blue color. Evidently, both calculations converge to the same results, but the inclined coordinate system needs at least 25×25 harmonics for a convincingly converged result. For small truncation orders, the deviation is especially large in the case of the rotation angles.

3.5.5 Gold bowties

As it has been mentioned in section 3.2, a periodic array of gold bowties is one of the most challenging structures used in modern nano-optics. As it is difficult to obtain a numerical reference for this system, we are going to compare our results in this section with experimental measurements.

An array of gold bowties on a quartz substrate ($\varepsilon = 2.25$) has been fabricated by electron beam lithography with periods $P^1 = 800$ nm and $P^2 = 500$ nm, in which the bowties consist of equal-sided triangles that exhibit a base length of 150 nm with the base aligned in the direction $\overline{x}^2$ (see figure 3.4d and sketch in figure 3.23a); the height is 180 nm, the thickness is 40 nm.[4] The gap between the tips of the triangles is 20 nm.

The numerical results of transmittance, reflectance, and absorbance spectra with adaptive spatial resolution and matched coordinates are depicted in figure 3.24a at normal incidence. Furthermore, figure 3.24a contains the

---

[4]Fabrication and measurements by M. Hentschel.
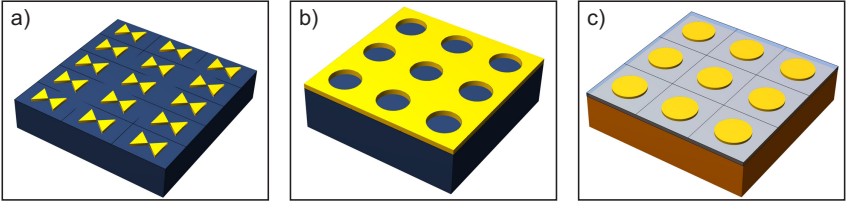
Figure 3.23: Sketches of experimentally fabricated structures for comparison with the Fourier modal method including matched coordinates: (a) gold bowties; (b) gold film; (c) gold dots on thick gold film with spacer layer.

experimental data in transmittance, which exhibit a good agreement in the resonance position with some deviation in the linewidth.

Note that we have described the gold with measured permittivity data according to [115] in order to obtain a slightly better agreement of the resonance position. Regarding the linewidth, it is a general property of experimental data that the resonances are broader (see, e.g., figure 2 in reference [45]). The reason is most likely a broadening due to the inhomogeneities occurring due to the fabrication tolerances. Thus, we observe only an average over a whole class of slightly different structures in the measurements. In summary, the qualitative agreement between the experiment and the calculation with a truncation order of 35×35 harmonics is quite good.

Panels (b-d) of figure 3.24 show the convergence behavior of the far field spectra at three different energies. Although there is a tendency to converge to specific values, it is obvious that the convergence behavior is worse compared to the previous examples. However, the qualitative agreement between experiment and numerical calculations is very convincing, so that the deviation between different truncation orders can be neglected for most practical applications, where the exact numbers are usually not crucial. Whether the convergence is good enough for nonlinear Fourier modal calculations according to references [85, 86] is an interesting question that should be addressed in the future.

3.6 Comparison between experiment and matched coordinates

In this section, we show two examples, where it has been superior to describe the occurring geometries by matched coordinates in order to achieve a good agreement between experimental data and numerical calculations with the
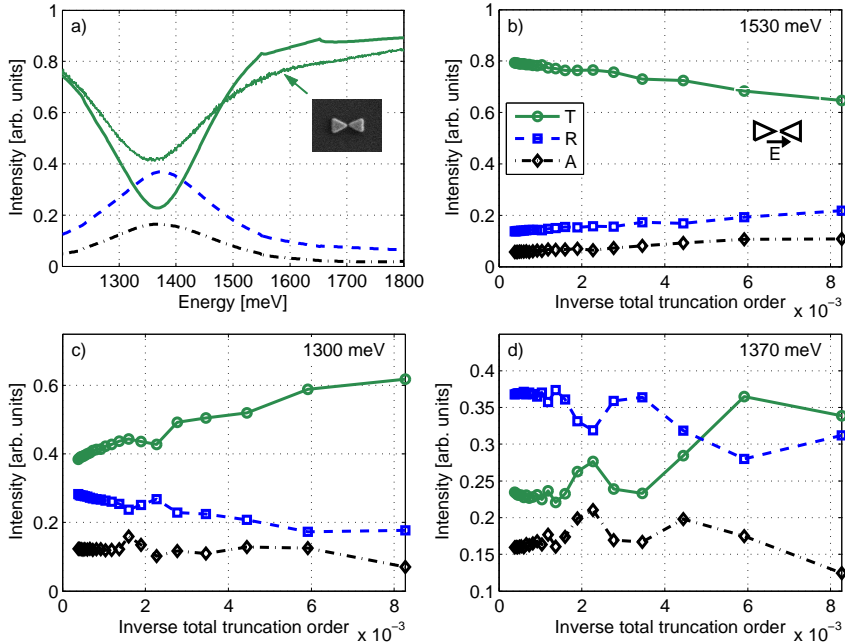
Figure 3.24: Transmittance (solid lines), reflectance (dashed lines), and absorbance (dashed-dotted lines) for a periodic array of gold bowties at normal incidence. Thick lines in panel (a) depict the far field spectra obtained by the Fourier modal method with matched coordinates and adaptive spatial resolution, the thin lines show the experimentally measured transmittance. The convergence behavior of the Fourier modal method is presented in panels (b-d) at different energies.

Fourier modal method. As the structures in both examples can be described by the coordinate transformation of section 3.2.1, which has been studied intensively in the previous sections as regards the convergence behavior, we refrain from additional convergence plots and show just some results at reasonable truncation orders.

3.6.1 Mueller matrix of perforated gold film

In the case of ellipsometry measurements, it is common to derive the Mueller matrix instead of elements of the scattering matrix. As mentioned in section 2.4, we can convert the small scattering matrix into Mueller matrices. In this subsection, we present the comparison of experimentally and numeri-

cally derived Mueller matrix elements for a periodic array of holes in a gold film [116]. The gold layer is 20 nm thick and contains air holes of diameter 225 nm in a square lattice configuration with period 400 nm (see figure 3.23b). The gold is described by tabulated permittivity values [115]; the superstrate consists of air and the substrate is quartz (refractive index 1.5).

Figures 3.25 to 3.27 depict a selection of experimentally and numerically derived Mueller matrix elements in reflection for incidence angles θ (see figure 2.2a) between 20° and 72° (incidence from the superstrate) at 1200 meV.[5] All Mueller matrix elements are normalized to the element M_{11}, which defines the outgoing intensity.
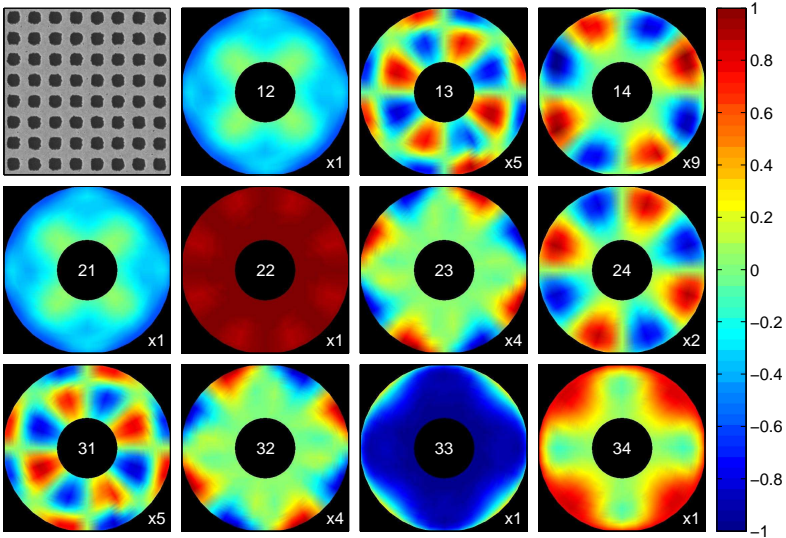
Figure 3.25: Selection of experimentally measured Mueller matrix elements for a periodic array of air holes in a gold film (see figure 3.23b).

The experimentally measured Mueller matrix elements are shown in figure 3.25. As it is not clear from the fabricated structure whether the hole shape is rather quadratic or round (see scanning electron micrograph image in the left upper panel of figure 3.25), we have calculated the Mueller matrix elements for both quadratic and circular holes.

The results for circular holes using the transformation described in section 3.2.1 with a truncation order of 21×21 harmonics are displayed in figure 3.26 and exhibit a good agreement with the experimentally measured

---

[5]Fabrication by U. Hübner; ellipsometry measurement by J. Braun.
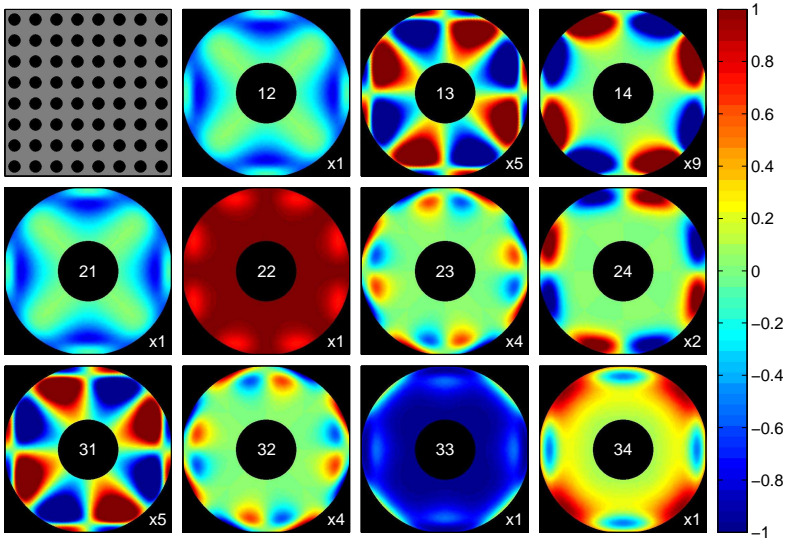
Figure 3.26: Same Mueller matrix elements as in figure 3.25, calculated for round holes by the Fourier modal method with matched coordinates.
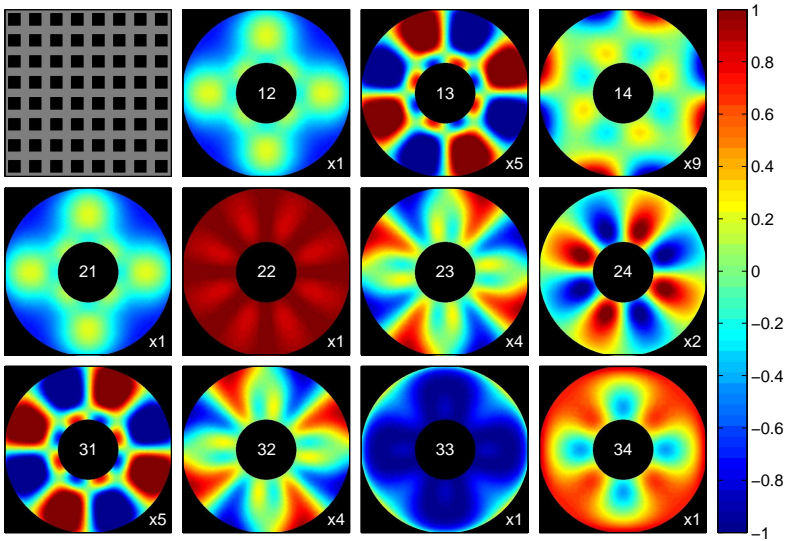

Figure 3.27: Mueller matrix elements as in figure 3.25, calculated for quadratic holes by the standard Fourier modal method with adaptive spatial resolution.

Mueller matrix elements. In contrast, the results obtained for quadratic holes (see figure 3.27) deviate clearly from the experimental measurement. Evidently, the influence of the hole shape cannot be neglected for the example of the periodic hole array.

3.6.2 Perfect absorber

The consideration of the exact shape is not only crucial for hole arrays, but also for the inverse structure with dots. In a recent publication [46], we have shown that we can achieve nearly 100 % absorbance by placing a periodic array of gold dots in an appropriate distance on top of a thick gold layer. In our design, the gold layer has a thickness of 200 nm, which is thick enough so that almost no light is transmitted. The gold dots are located on top of a MgF_2 spacer layer (permittivity value $\varepsilon = 1.9$) with thickness 30 nm and arranged in a square lattice with period 600 nm. The gold dots are round cylinders with thickness 20 nm and diameter 352 nm. We describe the gold permittivity by a Drude model (see section 2.7) with $\epsilon_\infty = 1$, $\omega_P = 1.37 \times 10^{16}$ rad/s, and $\gamma = 1.22 \times 10^{14}$ rad/s. The substrate is quartz (refractive index 2.25); the superstrate is air. A schematic of the structure can be seen in figure 3.23c.

Without the gold dots, the thick gold layer can be considered as a mirror with 100 % reflectance and 0 % transmittance. Owing to the fundamental plasmonic resonance of the gold dots, also the reflectance of the structure is reduced. For the parameters described above, even in the experiment, we achieved a maximum absorbance of ≈ 99 % at normal incidence. The experimental data of reflectance and absorbance can be seen in figure 3.28a.
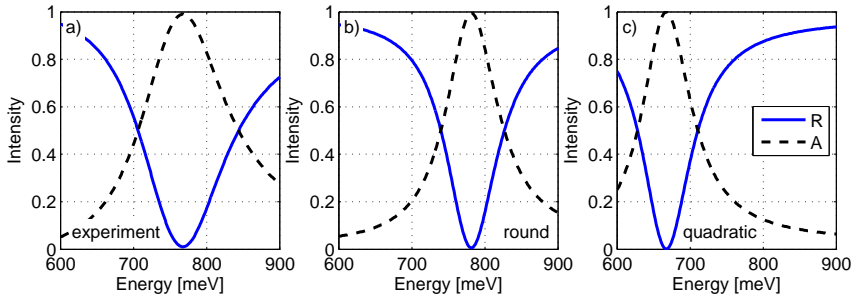

Figure 3.28: Far field spectra of periodic arrays of gold dots on a thick gold layer (see figure 3.23c) with nearly 100 % absorbance (blue curves). Panel (a) depicts experimental measurements. The numerical results in panel (b) have been calculated for round dots, whereas the calculations in panel (c) have been derived for quadratic dots. The black dashed lines denotes reflectance.

If we calculate the gold dots in the Fourier modal method with matched coordinates using the coordinate transformation for circular structures described in section 3.2.1, the agreement between experiment and numerical calculation is very good, as it can be inferred from the numerical results in figure 3.28b, which have been derived for a truncation order of 25×25 harmonics. If we use a quadratic shape instead of the circular dots with the side length equal to the dot diameter (see figure 3.28c), the maximum absorbance is clearly shifted compared to the experimental measurements. We do not claim that it is impossible to achieve a good agreement between numerical calculations and experiment also in the case of the quadratic dots by tuning the side length of the square dots, but the advantage of a correct description of the shape is obvious in the case that we can derive the shape parameters directly from the experiment.

3.7 Notes on coordinate transformations

We have shown in this chapter that the concept of matched coordinates improves the convergence behavior of the Fourier modal method when comparing it with simple zig-zag approximations. Both approaches – the zig-zag and the matched coordinates – evidently converge to the same results. In the case of metals, however, the concept of matched coordinates with adaptive spatial resolution is definitely superior.

Regarding the derivation of appropriate coordinate transformations, we find that smooth transformations with continuous coordinate derivatives may converge better; however, there is a trade-off between smooth transformations and the fact that the change of coordinates should be carried out slowly over the unit cell with a smooth modulation. For achieving the latter, one should consider curvilinear borders of the unit cell, as seen in figure 3.18a.

It should be kept in mind that our findings are not based on any rigorous proofs. They have been derived only in agreement with our experience. Hence, one should not consider them as too strict; it is in any case better to have matched coordinates, independently on the exact shape of the coordinate transformation.

For the future, it is also important to develop methods that allow the application of different coordinate transformations in the different layers of a stacked system. Some work has been devoted to this problem in the case of one-dimensional adaptive spatial resolution [104], but an extension to two-dimensional coordinate transformations has not been achieved yet.

4 Derivation of resonances in the scattering matrix formalism

The examples presented in chapter 3 exhibit optical resonances, which can be clearly seen as distinct features in the far field spectra. In most cases, it is possible to investigate resonances by determining the far field spectra; however, some resonances cannot be exited for specific incidence parameters (see, e.g., comparison between normal and inclined incidence in section 3.5.1), so that it is often much more efficient to determine resonances ab initio either analytically or by some numerical method.

In this chapter, we are going to present an efficient numerical method for the derivation of optical resonances using the scattering matrix formalism. We are showing here several examples with different types of resonances, without going into details on the origin of these resonances. For more information on the physics of the resonances, an interested reader may consult established text books, such as reference [21].

4.1 Mode solver for optical resonances

We have shown in several publications that it is possible to use the scattering matrix theory for obtaining the three-dimensional eigenmodes of a given structure [14, 15, 62, 99, 117]. We follow in this section mostly these references, especially that with the application of adaptive spatial resolution and matched coordinates [14]. In the first place, we address the question how resonances can be expressed in terms of the scattering matrix theory.

An eigenmode is a solution of Maxwell's equation that can oscillate in time with a resonance energy Ω and damping Γ without any external excitation $|I\rangle$. Formally, we would have to derive a non-vanishing output $|O\rangle = \mathbb{S}(E, \mathbf{k})|I\rangle$ [see equation (2.46)] for zero input $|I\rangle$. This means that we are searching for poles of the scattering matrix. In practice, it is more convenient to formulate the inverse problem $\mathbb{S}^{-1}(E, \mathbf{k})|O\rangle = |I\rangle$ [14, 62, 101], which yields in the case of zero input the nonlinear eigenvalue problem

$$\mathbb{S}^{-1}(E, \mathbf{k})|O\rangle = 0, \tag{4.1}$$

where the derivation of resonances is equivalent to finding non-trivial solutions $|O\rangle$ that solve equation (4.1) for specific pairs of resonance energy E_{res} and resonant wave vector $\mathbf{k}_{\mathrm{res}}$.

As E and the absolute value of $\mathbf{k}$ are not independent, we can derive k_3 as a function of E (or vice versa) in the homogeneous top and bottom layer of our stacked system. Furthermore, the in-plane momentum defined by k_1 and k_2 can be fixed as an external quantity, because it is conserved in all layers due to momentum conservation (excluding Umklapp processes). Thus, we have to find specific complex energies $E_{\mathrm{res}} = \Omega - i\Gamma$ so that equation (4.1) is fulfilled. In numerical calculations, the solution has to be derived in an iterative procedure on the complex energy plane.

4.1.1 Iterative mode derivation

Although it is possible to solve equation (4.1) by considering the determinant of the inverse scattering matrix and searching its roots by a simple Newton method, it is much more efficient to derive the solution iteratively by linearization around an energy E_0 [14, 15]:

$$\mathbb{S}^{-1}(E)|O\rangle \approx \left[\mathbb{S}^{-1}(E_0) + \left.\frac{\partial \mathbb{S}^{-1}}{\partial E}\right|_{E_0} \Delta E \right] |O\rangle = 0\,. \tag{4.2}$$

In this case, $\Delta E = E - E_0$ expresses the energy dependence of the linearized form. The non-trivial solutions of vectors $|O\rangle$ for the linearized equation (4.2) can be found by considering the relation on the right hand side of the approximation sign as a linear eigenvalue problem for eigenvalues ΔE. Those vectors that correspond to eigenvalues $\Delta E \to 0$ provide also non-trivial solutions for the original problem defined by equation (4.1), with resonances at $E_{\mathrm{res}} = E_0$. These resonances have to be determined iteratively by linearization around different energies E_0, until at least one eigenvalue obeys $\Delta E \to 0$.

As it is possible to derive from equation (4.2) more than one candidate for the next iteration step, the amount of iterations for finding a resonance can be decreased significantly in dependence on the used strategy for choosing an appropriate energy for the next iteration step. In general, the absolute value of ΔE should not be very large, so that we need to find only a few eigenvalues of equation (4.2) with a small magnitude. In addition, we can analyze the output vectors with respect to symmetry and far field properties in order to specify additional search criteria. Another advantage compared to simply solving $\det(\mathbb{S}^{-1}) = 0$ is that the degeneracy of an eigenvalue ΔE corresponds to the degeneracy of the associated resonance. Furthermore, the approach is rather stable, and we can also save other candidates during the iteration in order to use them as starting points for further iterations.

Figure 4.1 depicts a stability map, where each point of the equidistant grid in the complex energy plane corresponds to a start value for the iterative mode search procedure in the case of the test system described in section 4.2.1. Panel
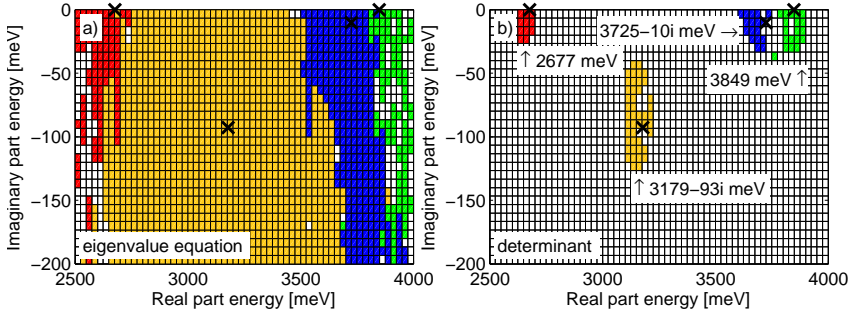
Figure 4.1: Stability map for (a) the eigenvalue method described by equation (4.2) and (b) a Newton method using the determinant of the inverse scattering matrix in the case of the example described in section 4.2.1. Black thin lines depict a grid of starting points, from which both methods should converge to one of the four resonances indicated by the black crosses within maximum ten iteration. No convergence has been achieved when the area around the starting value is displayed in white; otherwise, it is indicated by the different colored areas, to which resonance the method converged [for details on the convergence areas, see colors and labels in panel (b)].

(a) of figure 4.1 has been derived via equation (4.2); for the calculation of panel (b), we used the determinant of the inverse scattering matrix in combination with a simple Newton method. The truncation order for both cases is $N_G = 31$ harmonics and chosen to be sufficiently large in order to reproduce the physical phenomena correctly. In the presented range, we determined four resonances with resonance energies 2676.9 meV, $3179.2 - 92.9i$ meV, $3725.3 - 10.4i$ meV, and 3848.7 meV.

Evidently, almost every starting point in figure 4.1a converged to one of the four resonances in the sense that the smallest eigenvalue of equation (4.2) reached a relative magnitude $|\Delta E/E_0|$ smaller than 10^{-5} within maximum ten iterations. The average number of iterations was 5.1, the average relative magnitude of the smallest eigenvalue has been determined as 4×10^{-7} in the case of convergence. In contrast, we can deduce from figure 4.1b that the determinant method requires good starting values in order to converge to a resonance in maximum ten iterations.

One reason for the poor convergence of the determinant method is a short average iteration distance of 15.9 meV compared to 72.8 meV in the case of the eigenvalue equation (4.2). It seems that the linearized determinant does not reproduce the exact resonance position as good as the eigenvalue method.

Note that the particular convergence map shown in figure 4.1a depends strongly on the strategy used for finding the modes. For instance, the regions converging to the optically inactive modes can be increased by adjusting the strategy such that modes with a small linewidth and a vanishing far field contribution are preferred.

The downside of solving equation (4.2) is that we have to calculate the derivative of the complete scattering matrix. Therefore, using numerical differentiation, we have to warrant the continuity of the scattering matrix on the complex energy plane.

4.1.2 Inverse scattering matrix

It is noteworthy that the scattering matrix becomes close to singular when approaching a resonance. Hence, it is not very stable to invert the scattering matrix numerically. Instead, it is just as correct to invert the order of incoming and outgoing channels in the top and bottom layers. Thus, the scattering matrix $\mathbb{S}$ in equation (2.46) is replaced by a matrix $\tilde{\mathbb{S}}$ of the form

$$
\begin{bmatrix} \vec{\mathbb{A}}_N^- \\ \vec{\mathbb{A}}_1^+ \end{bmatrix} = \underbrace{\begin{pmatrix} \tilde{\mathbb{S}}_{N1}^{--} & \tilde{\mathbb{S}}_{NN}^{-+} \\ \tilde{\mathbb{S}}_{11}^{+-} & \tilde{\mathbb{S}}_{1N}^{++} \end{pmatrix}}_{=\tilde{\mathbb{S}}_{N1}} \begin{bmatrix} \vec{\mathbb{A}}_1^- \\ \vec{\mathbb{A}}_N^+ \end{bmatrix} ,
\tag{4.3}
$$

which resembles basically a permutation of the inverse scattering matrix.

The reordering of incoming and outgoing channels can be carried out easily when considering a redefinition of the material matrix $\mathcal{F}_{||}$ of equation (2.29), which connects expansion coefficients $\vec{\mathbb{A}}^{\pm}$ in one layer with the Fourier representation of the corresponding electric and magnetic fields:

$$
\mathcal{F}_{||} \begin{pmatrix} \vec{\mathbb{A}}^+ \\ \vec{\mathbb{A}}^- \end{pmatrix} = \begin{pmatrix} \vec{\mathcal{E}} \\ \vec{\mathcal{H}} \end{pmatrix} = \tilde{\mathcal{F}}_{||} \begin{pmatrix} \vec{\mathbb{A}}^- \\ \vec{\mathbb{A}}^+ \end{pmatrix} .
\tag{4.4}
$$

In this case, the matrix $\tilde{\mathcal{F}}_{||}$ is constructed from the matrix $\mathcal{F}_{||}$ by reordering the columns. We suggest now to keep the scattering matrix iteration in all internal layers unchanged, but to replace the matrix $\mathcal{F}_{||}$ in the outermost layers by $\tilde{\mathcal{F}}_{||}$ in order to derive the inverse scattering matrix.[1]

It is worth mentioning that this approach involves partially reordered scattering matrix expressions, where the input and output contain either forward

---

[1] For stability reasons, note that the outer layers should be included with zero thickness. Otherwise, $\tilde{\mathbb{S}}$ becomes unbalanced due to the occurring exponentially increasing terms.

or backward solutions. For instance, for the description of layers 1 to n with $n < N$, we compute matrices of the form

$$\begin{bmatrix} \vec{\mathbb{A}}_n^+ \\ \vec{\mathbb{A}}_1^+ \end{bmatrix} = \begin{pmatrix} \mathbb{S}_{n1}^{+-} & \mathbb{S}_{nn}^{+-} \\ \mathbb{S}_{11}^{+-} & \mathbb{S}_{1n}^{+-} \end{pmatrix} \begin{bmatrix} \vec{\mathbb{A}}_1^- \\ \vec{\mathbb{A}}_n^- \end{bmatrix}. \tag{4.5}$$

It is evident that equation (4.5) becomes instable when the reflection drops to zero, as in this case forward and backward solutions are no longer connected. We have experienced such a behavior especially for larger truncation orders, but the principle can be easily understood when trying to exchange the orders at a fictitious interface between identical layers. Then, the construction of the matrix in equation (4.5) requires the inversion of a singular matrix.

In particular, the derivation of the scattering matrix contains the inverse of $\mathbb{S}_{12}\mathbb{Y}_{21} - \mathbb{Y}_{11}$ [see equation (2.53)], where $\mathbb{S}_{12} = 0$ at the top interface, and – according to equation (2.48) – after exchanging the order of input and output in the outermost layers, $\mathbb{Y}_{11} = \mathbb{T}_{21}^{-+}$. Hence, if the element $\mathbb{T}_{21}^{-+}$ of the uppermost interface transfer matrix is close to singular, the construction of the scattering matrix becomes unstable.

Figure 4.2a depicts the convergence of the resonances determined in the case of the example described in section 4.2.1. We have extrapolated the convergence behavior for $1/N_G \to 0$ in order to derive reference energies E^{ext} for an infinite truncation order, with the extrapolated energies $2676.8557\,\text{meV}$, $3179.1749 - 92.9041i\,\text{meV}$, $3725.319 - 10.3878i\,\text{meV}$, and $3848.6674\,\text{meV}$. Note that we excluded in the extrapolation all results for truncation orders beyond $N_G = 31$ harmonics, because these solutions seem to be already unstable.

Evidently, the modes start to converge rather quickly to the extrapolated values for truncation orders between 11 and 31 harmonics, but already around $N_G = 19$, we observe a saturation; truncation orders beyond 31 harmonics provide already questionable results. Figure 4.2b elucidates the origin of the saturated convergence, which is an increasing condition number of the element $\mathbb{T}_{21}^{-+}$ for increasing truncation orders in the case of the top interface transfer matrix. Note that the condition number is defined as the ratio of the largest singular value of a matrix to its smallest singular value. Hence, large condition numbers imply instabilities in the inversion of $\mathbb{T}_{21}^{-+}$, so that the convergence of the mode solver is hampered. Similar problems can be found for the bottom interface transfer matrix.

In order to avoid such problems, it is of course possible to reorder also the inner layers, but then we would have to deal with exponentially growing terms in these layers, which may grow beyond the maximum floating point number available in the numerical calculation.

Despite the stability issue, we believe that the advantages of the inverse order approach outperform the drawbacks, as the method is faster than the
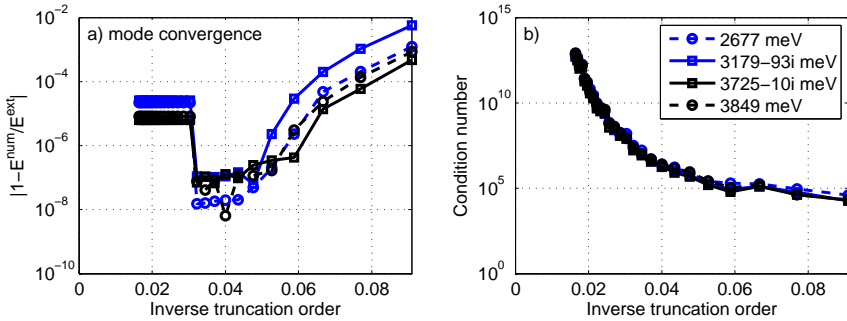
Figure 4.2: Panel (a) depicts the relative convergence behavior of the different resonances determined for the example described in section 4.2.1. The reference values E^{ext} have been extrapolated from the inverse truncation order for $1/N_G \to 0$. Panel (b): Condition number of the matrix element $\mathbb{T}_{21}^{-+}$ [see equation (2.48)] that has to be inverted at the top interface according to equation (2.53) when exchanging the order of input and output in the top layer.

numerical inversion of the scattering matrix. Also, it requires only a minimum amount of changes in order to derive the resonant field distribution inside the structure of interest in the same way as one usually calculates the field distribution in these layers for far field excitation. We only have to use the resonant output vector $|O\rangle$ of equation (4.2) as the input of the partially reordered scattering matrices. More details on the way we use in order to construct fields inside a structure can be found in reference [118].

4.1.3 Continuity of scattering matrix

As mentioned before, using equation (4.2) for finding optical resonances requires that the numerically derived scattering matrix is continuous with respect to energy, because the linearization involves the computation of the matrix derivative. The derivative can be calculated numerically, but care has to be taken that the basis set in the top and bottom layer is chosen properly, including the sorting of incoming and outgoing channels. These requirements can be easily fulfilled in cases where we are able to use the analytical Rayleigh expansion of section 2.3.4. Then, the sorting of the channels can be fixed uniquely, as the basis solution of the homogeneous layers does not depend on the energy.

In the case that the underlying coordinate system is not uniform, it has been discussed in section 3.4 that the solution of homogeneous layers cannot be derived analytically. Hence, care has to be taken, because the numerically

derived eigenvalue matrix $\mathcal{F}_{\parallel\,\text{homo}}$ for homogeneous layers [see equation (2.29)] may be discontinuous with respect to energy. In order to overcome this problem when calculating the derivative of the inverse scattering, we have suggested to use the numerical solution for one homogeneous layer in order to derive the numerical solutions of all other homogeneous layers according to the method described in section 3.4.3 [14]. Thus, we can maintain the basis set as well as the ordering of the channels even in non-uniform coordinate systems.

In addition, we have to warrant the continuity of the propagation constants K_{mn}^3. Note that there exists an ambiguity in its definition according to equation (2.42), because the square root of complex numbers is only fixed up to an artificial cut in the complex energy plane. First of all, we choose $\Re(K_{mn}^3) + \Im(K_{3mn}^3) > 0$. Then, we ensure that the propagation constants K_{mn}^3 remain continuous when calculating the derivative of the inverse scattering matrix at each iteration step, in spite of the artificial cut in the complex plane.

4.2 Numerical examples

In the previous chapter, we have focused on structures which are periodic in two directions. Henceforth, we will consider also one-dimensional periodic structures, because it is easier to acquire a large amount of data for detailed analysis. Figure 4.3 presents some examples of such structures.
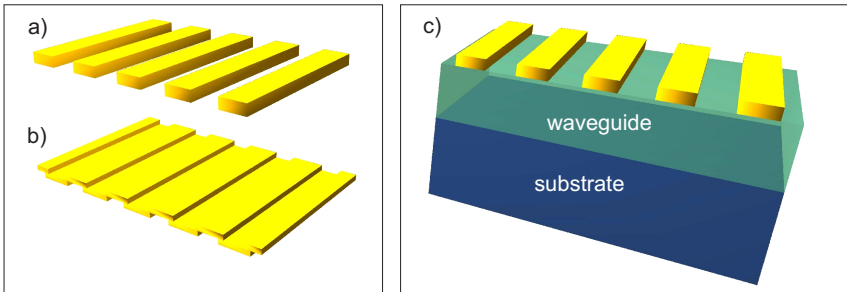
Figure 4.3: Examples of one-dimensional periodic structures with translation invariance in a direction perpendicular to the direction of periodicity: (a) array of wires; (b) meander layer; (c) multilayer system with wires on top of a waveguide.

4.2.1 Dielectric grating

One of the one-dimensional structures that we will discuss in detail is the dielectric grating introduced in our recent publications on resonant mode coupling [14, 15]. The structure consists of a dielectric slab of thickness 50 nm with a refractive index of 2.5 (e.g., ZnO), which contains air slits of width 100 nm that repeat periodically with a period of 300 nm; the surrounding medium is air. Would the slab be homogeneous, it would exhibit TE and TM polarized waveguide resonances, which lie outside the light cone [21]. By cutting periodic slits into the slab, we can excite back-folded branches of these resonances even at normal incidence [62]. In this particular example, we find the back-folded first order branches in the region between 2500 meV and 4000 meV. Figure 4.4 depicts the corresponding far field spectra for TM and TE polarization in panel (a) and (b), respectively.
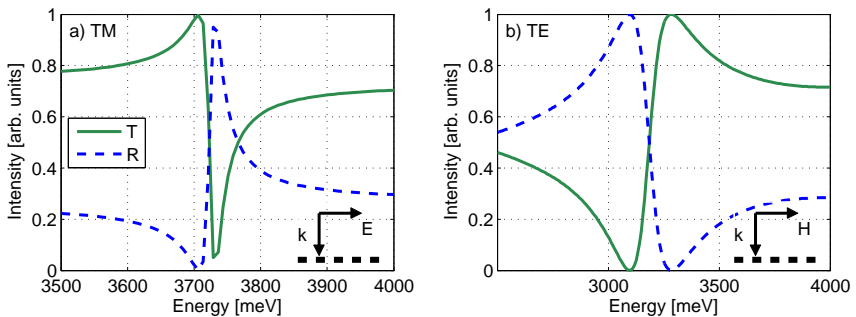
Figure 4.4: Transmittance (solid green line) and reflectance (dashed blue line) for a dielectric waveguide slab with periodic air slits for TM polarization in panel (a) and TE polarization in panel (b).

Note that the back-folded waveguide dispersions exhibit a band gap at $k_1 = k_2 = 0$ [21, 62], where one branch is optically active and the other one is optically inactive. Hence, we observe in the spectra only one resonance per polarization at normal incidence; a sharp TM polarized resonance around 3700 meV (see figure 4.4a), and a broad TE polarized resonance around 3200 meV (see figure 4.4b).

We are now going to present the resonance energies as well as the resonant field distributions obtained by the methods described in section 4.1. Note that section 4.1 contains already results for this particular dielectric grating; figure 4.1 depicts the stability of the iterative mode search procedure in dependence on different starting energies, whereas figure 4.2 contains convergence and stability plots for increasing truncation orders.
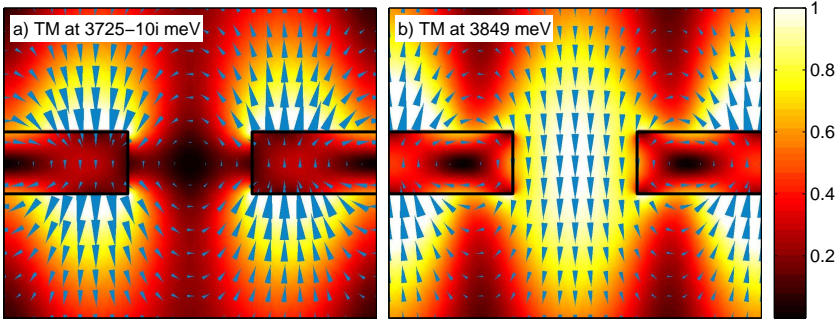
Figure 4.5: Electric field distributions of the TM polarized resonances occurring in the case of a dielectric grating. The calculations have been carried out by the mode solver described in section 4.1 without external excitation. Panel (a) depicts an optically active mode; the mode in panel (b) is optically inactive. The cones indicate the electric field at a typical time step, whereas the background color denotes the energy density of the electric field in a normalized logarithmic scale.

In figure 4.5a, we can see the resonant electric field distribution of the optically active TM polarized resonance obtained by the mode solver without external excitation. We found a resonance energy of $3725 - 10i$ meV for a truncation order of 31 harmonics with adaptive spatial resolution, which resembles perfectly the resonant phenomenon in the far field spectra (see figure 4.4a). Note that the application of adaptive spatial resolution is not really necessary for the dielectric grating, but we included it for the sake of consistency with the following metallic examples, which require the application of adaptive spatial resolution for an efficient calculation [12, 76].

Using the mode solver of section 4.1, we can also derive the symmetry forbidden TM resonance at normal incidence, which is located at 3849 meV. The corresponding electric field distribution is shown in figure 4.5b. At this point, we have to emphasize that the field distributions have been calculated without external incidence using the resonant output vector $|O\rangle$ as the input of the partially reordered scattering matrices [see, e.g., equation (4.5)].

The field distributions of the fundamental optically active and inactive TE modes are depicted in figure 4.6. The calculations have been carried out for the same truncation order of 31 harmonics as we have used for the TM polarization, but we display in figure 4.6 the magnetic field distribution instead of the electric field, because the latter field has a vanishing component in the direction of periodicity for TE polarized modes. We derived resonance energies of 2677 meV and $3179 - 93i$ meV for the optically inactive and active mode,
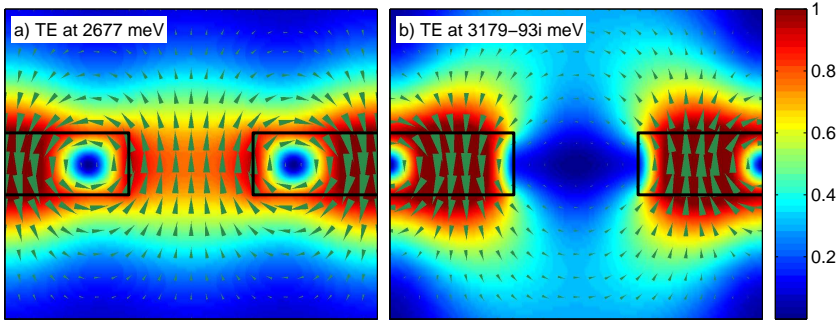
Figure 4.6: Magnetic field distributions of TE polarized resonances derived by our mode solver without external excitation for the same dielectric grating as in figure 4.5. We obtained an optically inactive mode at 2677 meV, which is shown in panel (a). The nearest optically active mode has been derived at $3179 - 93i$ meV and is depicted in panel (b). The cones indicate the magnetic field at a typical time step; the background color denotes the energy density of the magnetic field in a normalized logarithmic scale.

respectively. As in the case of the TM polarized optically active mode, both the resonance position (real part of resonance energy) as well as the linewidth (twice the imaginary part of resonance energy) agree very well with the far field spectra depicted in figure 4.4b.

4.2.2 One-dimensional periodic gold wires

A typical structure in modern nano-optics are periodic arrays of infinite gold wires [53, 68] (see figure 4.3a). We have chosen wires of width 200 nm, height 30 nm, and period 400 nm. The surrounding medium has a scalar permittivity of 2.13 (quartz), the gold is described via the analytic model of reference [114]. Note that the mode solver requires an analytic continuation of any dispersive material parameters on the complex energy plane, which limits the method to either constant material parameters or standard model functions. Figure 4.7a depicts the far field spectra of this type of metallo-dielectric grating at normal incidence, with the incident electric field aligned in x direction (see inset in the upper right corner). We observe a broad plasmonic resonance in the range of 1000 meV to 2200 meV and small features beyond 2000 meV.

When using the linearized equation (4.2) for finding optical resonances iteratively, it should be kept in mind that some candidates at a given iteration energy are only solutions for the linearized inverse scattering matrix and do
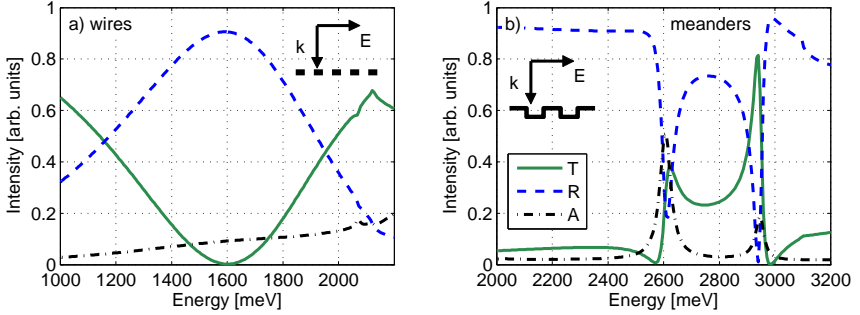
Figure 4.7: Transmittance (solid green line), reflectance (dashed blue line), and absorbance (dashed-dotted black line) for one-dimensional periodic metal structures. Panel (a) depicts the results of a periodic array of gold wires, the structure in panel (b) consists of a single metallic meander layer [105].

not correspond to physical resonances at all, whereas others reflect spurious resonances (see figure 4.8a). Such spurious resonances appear mostly in the case of metallo-dielectric systems and originate from the approximation of the permittivity and permeability distributions by a truncated Fourier expansion.

In particular, the permittivity and permeability of the numerical calculation exhibit an oscillating behavior on a small spatial scale, depending on the truncation order. We have determined that the spurious modes usually reflect these oscillations as if they were small cavities. In order to avoid finding such modes in our implementation, we analyze the resonant output vectors during the iterative mode search and consider all modes as spurious that are dominated by higher harmonics.

Besides the spurious resonance shown in figure 4.8a, we obtained the resonance energy of the broad plasmon resonance at $1683 - 514i$ meV. The corresponding resonant field distribution exhibits the typical form of a fundamental plasmon resonance with a dipolar field pattern, as it can be seen in figure 4.8b.

In addition to the fundamental plasmon resonance, we found a higher order plasmon resonance with one node in the vertical yz plane through the center of the wire at $2034 - 37i$ meV. As it can be deduced from the symmetry properties of the corresponding resonant mode distribution shown in figure 4.8c, this mode is optically inactive at normal incidence, so that it cannot be seen in the far field spectra. The tiny far field feature around 2070 meV corresponds already to an optically active higher order plasmon mode at $2071 - 8i$ meV with a node in the horizontal xy plane through the center of the wire (see figure 4.8d).
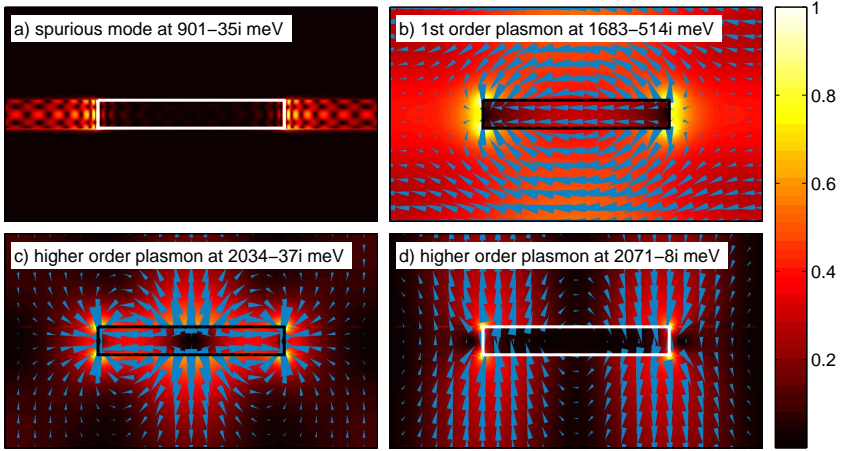
Figure 4.8: Electric resonant field distributions of an array of one-dimensional gold wires in quartz, calculated for a truncation order of 31 harmonics and adaptive spatial resolution; panel (a) depicts a spurious mode at $901 - 35i$ meV, the fundamental plasmon mode at $1683 - 514i$ meV is shown in panel (b), and higher order plasmon modes can be found in panels (c) and (d) at the energies $2034 - 37i$ meV and $2071 - 8i$ meV, respectively. The cones indicate the electric field at a typical time step; the background color denotes the energy density of the electric field in a normalized logarithmic scale.

4.2.3 Metallic meander structure

As another metallic test system, we use a single metallic meander layer in vacuum [105] (see figure 4.3b). It consists of a corrugated film of thickness $d = 30$ nm, which has two equally sized grooves on both sides with a depth of $h = 16$ nm that are shifted laterally by half a period with respect to each other (see sketch in figure 4.7b). As in reference [105], we describe the metal by a Drude model (see section 2.7) with $\varepsilon_\infty = 1$, plasma frequency $\omega_P = 1.37 \times 10^{16}$ rad/s and damping constant $\gamma = 8.5 \times 10^{13}$ rad/s. The period is 400 nm.

We have derived two delocalized surface plasmon polariton modes [6, 21] for the single meander layer in the range of 2000 meV to 3200 meV at $k_1 = k_2 = 0$. Below the opening of the first diffraction order around 3100 meV, a C_2 antisymmetric surface plasmon polariton is located at $2947 - 18i$ meV, and a C_2 symmetric surface plasmon polariton can be found at $2606 - 23i$ meV (see field distributions in figure 4.9). The C_2 rotation center is marked by a white cross in figure 4.9. Both surface plasmon polariton modes can be also
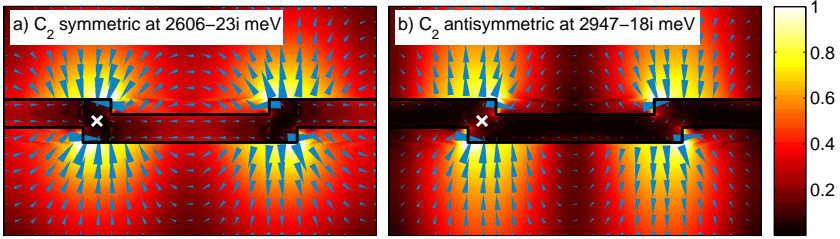
Figure 4.9: Electric field distribution (cones) of a C_2 symmetric surface plasmon polariton mode at $2606 - 23i$ meV in panel (a) and a C_2 antisymmetric surface plasmon polariton mode at $2947 - 18i$ meV in panel (b). The field distributions have been derived for a truncation order of 31 harmonics without external excitation and are depicted in one unit cell. The background color denotes the time averaged energy density of the electric field in a normalized logarithmic scale. The white crosses indicate the C_2 rotation center.

seen very well in the far field spectra in figure 4.7b.

Ideally, delocalized surface plasmon polaritons are surface modes that propagate along a metal-dielectric interface, but decay in the normal directions of the interface. A detailed description of such modes for single interfaces can be found, e.g., in reference [21]. As in the case of the waveguide modes, the surface plasmon polariton modes are outside the light cone for homogeneous slabs. Only due to the corrugation do they become visible at normal incidence. If the structure consists of a thin enough metal film with a thickness in the order of the skin depth of the metal, we furthermore observe as in the present example a mode splitting due to the coupling of modes that propagate on the opposing interfaces.

4.2.4 Magneto-optical waveguide coupled to gold wires

In section 3.5.4, we have briefly introduced a magneto-optical waveguide system, which is located below a thin gold layer that is periodic in two directions. In contrast, we present in this chapter a system that consists of a one-dimensional periodic array of gold wires on top of a magneto-optical waveguide with thickness 200 nm, which is described by the same permittivity tensor as the waveguide in section 3.5.4. The superstrate is air, the substrate is quartz with a permittivity value $\varepsilon = 2.13$. The wire width is 100 nm, the height is 30 nm. As in the previous section, we describe the gold by the analytic model of reference [114]. A schematic of the structure is depicted in figure 4.3c.

We have chosen a one-dimensional wire system, because we have gained

a lot of experience in our group with similar structures containing dielectric waveguide slabs [53, 119, 120]. In addition, the calculation time for one-dimensional periodic structures is orders of magnitudes smaller than that for two-dimensional systems, so that we can generate systematic parameter studies efficiently. The downside of these one-dimensional structures is a reduced lateral symmetry, which means that even at normal incidence any determined effects are strongly polarization dependent.
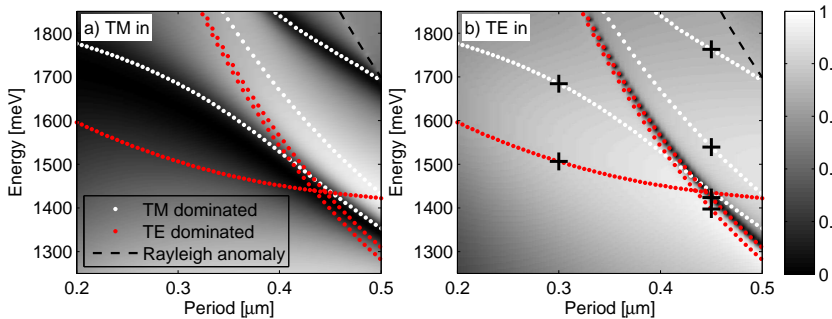

Figure 4.10: Period dispersion of spectra and modes for a one-dimensional array of gold wires on top of a magneto-optical waveguide. The background color denotes transmittance at normal incidence for TM polarized incidence in panel (a) and TE polarized incidence in panel (b); the dispersion of the occurring resonances is shown by dots. White dots indicate a predominantly TM polarized mode, red dots are modes with dominating TE contribution. The black dashed line denotes the opening of the first additional diffraction order in the substrate (Rayleigh anomaly); crosses in panel (b) mark the position of the field distributions shown in figures 4.12 and 4.13.

As mentioned in section 4.2.1, a planar homogeneous slab exhibits waveguide modes, which become optically active by introducing a periodicity in the system. Depending on the chosen period, the spectral position of the waveguide modes changes. In addition, the gold wires on top of the magneto-optical waveguide provide plasmon resonances, which are more or less independent on the period and interact with the waveguide modes. Figure 4.10 depicts as background color the period dependence of the transmittance at normal incidence ($k_1 = k_2 = 0$), with the incident electric field aligned long x and y direction, respectively. Although the magneto-optical waveguide couples x and y polarized fields, we refer to x polarized incidence as TM polarization and y polarized incidence as TE polarization,[2] because the coupling of the or-

---

[2]The terms TE and TM polarization refer to the xz plane, in which we obtain the additional

thogonal x and y polarizations is rather weak. Hence, we can also distinguish the waveguide modes as predominantly TE or TM polarized.

In addition to the transmittance, we plot also the period dispersions of the occurring resonances in figure 4.10, which have been calculated by our mode solver. We observe an anticrossing behavior between the TM dominated optically active waveguide mode and the plasmon mode in the region between 1600 meV and 1800 meV. The coupling between TE dominated waveguide modes (modes close to the minimum in transmittance for TE input) and the plasmon resonance of the wires seems to be negligible. However, the optically active TE and TM dominated branches do interact, as we can infer from the period dispersion of the Faraday rotation angle (see figure 4.11).
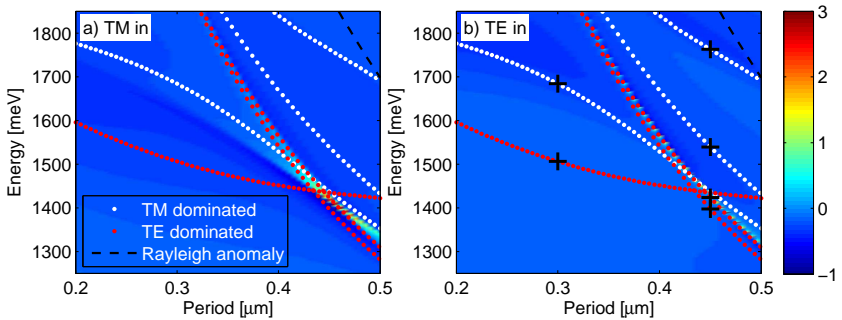

Figure 4.11: Period dispersion for the same structure as in figure 4.10, but with the Faraday rotation angle as background. All other lines and symbols are as in figure 4.10.

The maximum Faraday rotation of $2.87°$ is reached close to the crossing of the optically active TE and TM dominated branches around 450 nm period at an energy of 1400 meV. Hence, the crucial mechanism for the large Faraday rotation (3 times larger than in the case of reference [54]) is the weak coupling between the TM and the TE dominated resonances, which allows to transfer light from one to the other polarization.

Note that the maximum rotation is not observed at the exact position of the crossing between the optically active TE and TM dominated branches, but slightly shifted, because a specific incidence in TM or TE polarization can excite only the TM or TE dominated mode efficiently. The respective other mode can then be regarded as a driven oscillator with a maximum amplitude that occurs slightly off the resonance.

in-plane wave vector contributions for the excitation of the waveguide modes.
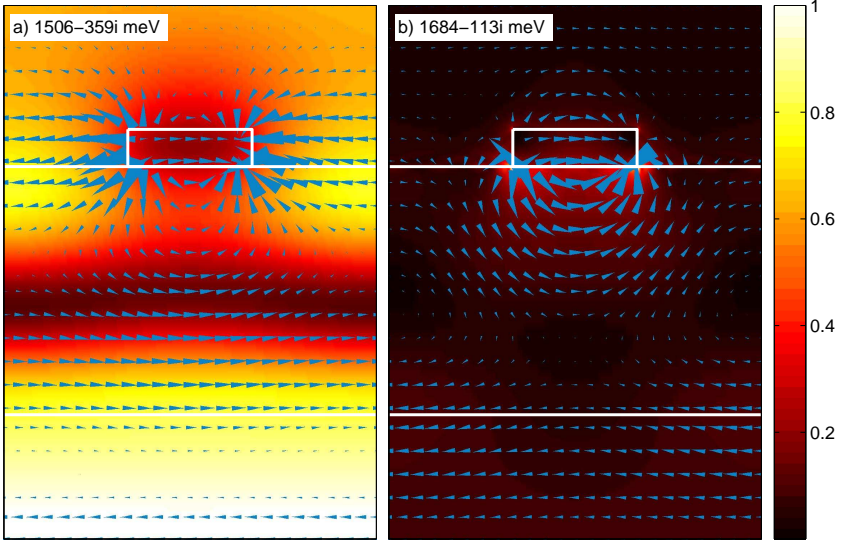
Figure 4.12: Resonant electric field distribution of a TE dominated Fabry-Perot mode in panel (a) and a TM dominated waveguide-plasmon mode in (b) at 300 nm period. Cones indicate the projection of the electric field on the xz plane; background color denotes the energy density of the electric field in a normalized logarithmic scale.

In the current design, the maximum Faraday rotation is located in a minimum of transmittance. However, it should be possible to increase the transmittance by carefully designing the wire-waveguide system, similar to the work by Belotelov et al. [54].

In order to illustrate our findings, we show also resonant electric field distributions in figures 4.12 and 4.13. Both figures depict the projection of the electric field to the xz plane as cones; the background color denotes the energy density of the electric field.

In the case of figure 4.12, the period is 300 nm, for which we find in figure 4.10 only one TM and one TE dominated branch. The TE dominated branch corresponds to a Fabry-Perot mode of the slab layer, which has – in contrast to the waveguide modes – a broad linewidth. We determined a resonance energy of $1506 - 359i$ meV at 300 nm period. The corresponding electric field distribution is depicted in figure 4.12a. Owing to the large linewidth of this branch, we can neglect its contribution to the enhanced Faraday rotation, as the change of the Faraday rotation with the energy is too quick.

Figure 4.12b shows the resonant field distribution of a TM dominated branch
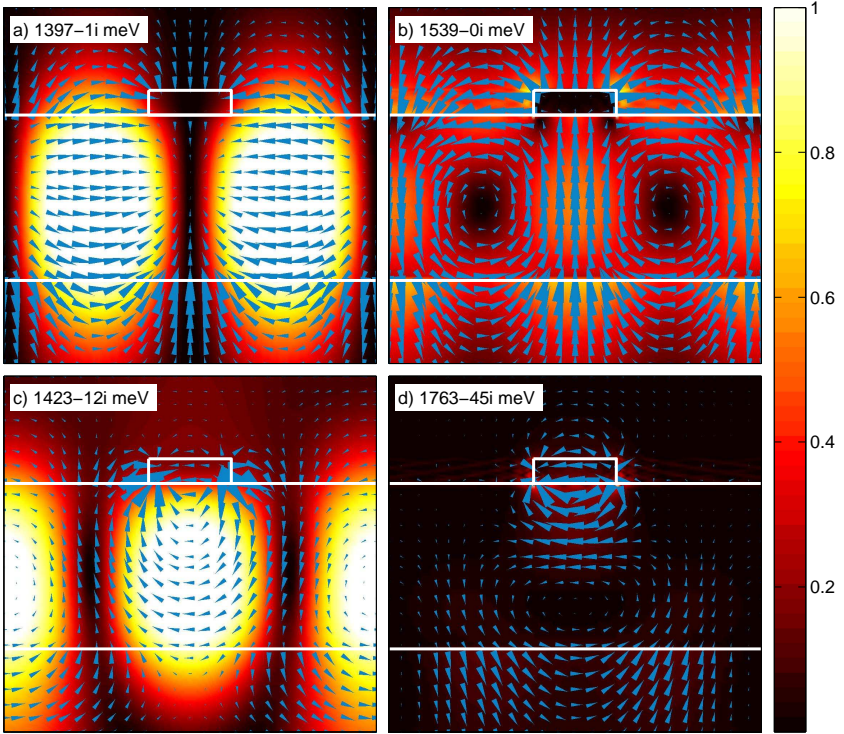
Figure 4.13: Field distribution of TE (left column) and TM (right column) dominated modes at normal incidence without external excitation for a period of 450 nm. Cones and colors are as in figure 4.12. The modes in the upper row are optically inactive, the lower row shows field distributions of optically active resonances.

with a resonance energy of $1684-113i$ meV at 300 nm period. This branch originates from the strong coupling of the optically active TM dominated waveguide mode and the plasmon mode of the gold wire.

The allowed interaction of TE and TM dominated resonances can be seen from the fact that the projection of the electric field distribution on the xz plane differs from zero also in the case of the TE dominated modes. Figure 4.13 displays a set of TE and TM dominated modes at 450 nm period as columns, where the upper row is optically inactive at normal incidence with resonance energies of $1397-1i$ meV and 1539 meV, respectively. The optically active resonances have been determined at $1423-12i$ meV and $1763-45i$ meV; the corresponding resonant field distributions are shown in the lower row of

figure 4.13.

4.2.5 Gold cylinders

In section 3.5.1, we have introduced a periodic array of gold cylinders with parameters taken from reference [14]. Figure 4.14 depicts a selection of resonant field distributions for this test system at $k_1 = k_2 = 0$ without external excitation.
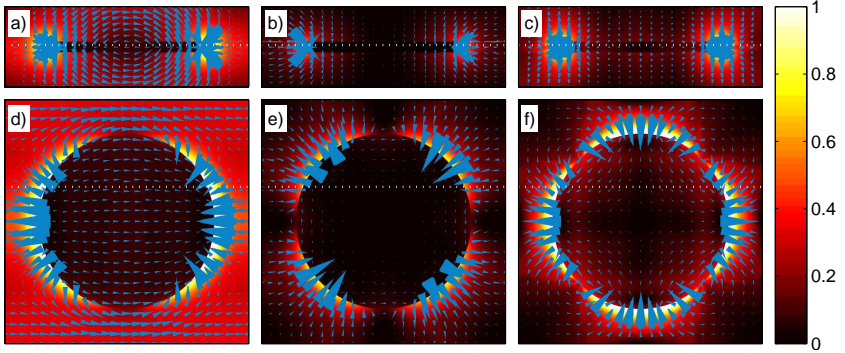

Figure 4.14: Resonant electric field distributions of a periodic array of gold cylinders (see section 3.5.1) calculated for a truncation order of $N_G = 17 \times 17$ harmonics without external excitation [14]. Columns depict from left to right: the fundamental plasmon resonance at $1263 - 446i$ meV, an optically inactive higher order mode at $1373 - 10i$ meV, and an optically inactive resonance at $1564 - 12i$ meV. The lower row shows a top view of one unit cell in the xy-plane, 10 nm below the upper interface of the cylinders. The upper row contains side views of planes normal to the y-axis and shifted by 100 nm with respect to the center of the unit cell. The locations of the slices are indicated by white dashed lines. Cones show the typical electric field pattern, the background color denotes the energy density of the time-averaged electric field in a normalized logarithmic scale.

The calculations have been carried out with matched coordinates for a truncation order of $N_G = 17 \times 17$ harmonics. The truncation order is sufficiently large for a convincing convergence of the results (see figure 3.14), but yet small enough in order to avoid problems with the stability of the partially reordered scattering matrices (see discussion in section 4.1.2). For the broad optically active resonance seen in figure 3.14a, we have derived a resonance energy of $1263 - 446i$ meV. The resonance is twice degenerate and exhibits a dipolar field distribution. An example of the corresponding resonant field distributions is depicted in panels (a) and (d) of figure 4.14 in side and top view, respectively.

The optically inactive modes expected from figure 3.15 have been found at $1373 - 10i$ meV and $1564 - 12i$ meV and possess a quadrupolar field pattern (see right two columns in figure 4.14). Both mode patterns correspond very well to our expectations of the physical behavior.

4.2.6 Gold hexagons

Similar to the array of gold cylinders, the example of gold hexagons described in section 3.5.2 exhibits plasmon resonances with a dipolar character. In contrast to the cylinders, these resonances are not degenerate due to the missing C_4 symmetry of the unit cell. For $k_1 = k_2 = 0$ and a truncation order of 21×21 harmonics, we determined two close resonances at $1263 - 320i$ meV and $1264 - 322i$ meV, where the first one is oriented in y direction, and the second one is oriented in x direction (see first two columns of figure 4.15). These findings agree very well with our observations made for the far field spectra shown in figures 3.16a and 3.17a.
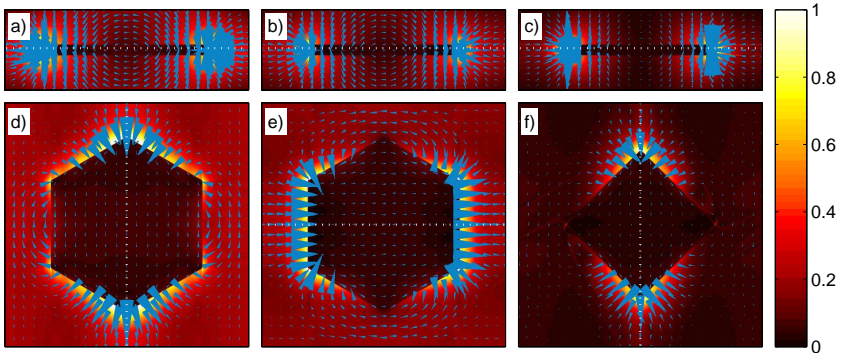

Figure 4.15: Resonant electric field distributions of a periodic array of hexagons in the first two columns and a periodic array of rotated squares in the last column. Cones show the typical electric field pattern, the background color denotes the energy density of the time-averaged electric field in a normalized logarithmic scale. We determined the following resonance energies (from left to right): $1263 - 320i$ meV, $1264 - 322i$ meV, and $1300 - 144i$ meV. The upper row shows side views through the center of the structures; the lower row depicts the top view of one unit cell. White lines indicate in each column the slices of the respective other row. The examples correspond to those described in sections 3.5.2 and 3.5.3.

4.2.7 Rotated gold squares

In addition to the previous two-dimensional periodic systems, we also derived the resonance energies of the rotated gold squares described in section 3.5.3 by our mode solver. We found a twice degenerate resonance at $1300 - 144i$ meV for $k_1 = k_2 = 0$ and a truncation order of 17×17 harmonics. Note that we used the coordinate transformation depicted in figure 3.18a, which seems to converge best when calculating the far field spectra. The resonant field distribution of this test system is depicted in the right column of figure 4.15.

5 Coupling model for stacked grating structures

In the field of optics, a lot of work is devoted to the understanding of the electromagnetic coupling between individual nanostructures [9, 32, 41, 50, 66, 68, 121, 122]. In addition to rigorous experimental and numerical studies, some simplified models have been developed for the description of the mutual coupling [9, 50, 66, 121–123], but these models either are restricted to the near-field by using a quasi-static approximation or include fitting parameters or both.

In this chapter, we present our approach of the resonant mode coupling for the approximation of the coupled resonances in a vertical stack of two gratings that is based on the derivation of the resonances in the case of isolated gratings [15, 16]. Our approach follows directly from Maxwell's equations without any fitting parameters by using the so-called resonant mode approximation of the scattering matrix [15, 99, 117]. The master equation of the resonant mode coupling is a linear eigenvalue problem with dimensions equal to the total number of relevant resonances from both layers.

Owing to the consideration of optical near fields, this method is even valid for the strong coupling regime in the case of closely stacked gratings. In addition, we extended the approach so that it is capable of describing the strong coupling regime between the individual grating resonances and the Fabry-Perot (FP) modes, which are formed between the grating layers in the far field regime [16].

5.1 Resonant mode coupling

5.1.1 Resonant mode approximation

Similar to the Breit-Wigner formula known in quantum mechanical scattering theory (see, e.g., [124]), the scattering matrix can be approximated by the resonant mode approximation, in which we express the resonances of the scattering matrix as follows [99]:

$$\mathbb{S}(E) \approx \tilde{\mathbb{S}}(E) + \sum_n \frac{|O_n\rangle\langle I_n|}{E - E_n} \,. \tag{5.1}$$

Here, we sum up over resonances with energies E_n and resonant output vectors $|O_n\rangle$ [see equation (4.1)]; the functional dependence of the resonances is that

of poles of order one. From the vector $\langle I_n|$ associated with each resonance, we can furthermore derive the contribution of a resonance for a given incidence vector $|I\rangle$ by evaluating the overlap term $\langle I_n|I\rangle$. Mathematically speaking, $|O_n\rangle\langle I_n|$ can be considered as a residue operator, which can be obtained by integration on a closed loop around the pole [125].

In principle, the sum in equation (5.1) can be extended over all resonances of the structure for the same incidence parameters k_1 and k_2. However, it is questionable, whether the functional dependence of the poles is correctly reproduced far away from the resonances, and it is practically impossible to find all modes of a given structure. Thus, the background term $\tilde{\mathbb{S}}(E)$ takes into account all resonances that have a vanishing contribution in the region of interest. Usually, $\tilde{\mathbb{S}}(E)$ changes only slowly with the energy compared to the explicit resonance contributions in equation (5.1).

Figure 5.1 illustrates the principle of the resonant mode approximation by depicting the Frobenius norm[1] of the exact scattering matrix as well as the resonant contributions and the background term of equation (5.1) in the case of the dielectric grating described in section 4.2.1. Evidently, the resonant contributions can describe the poles very well, whereas the background term is more or less constant.
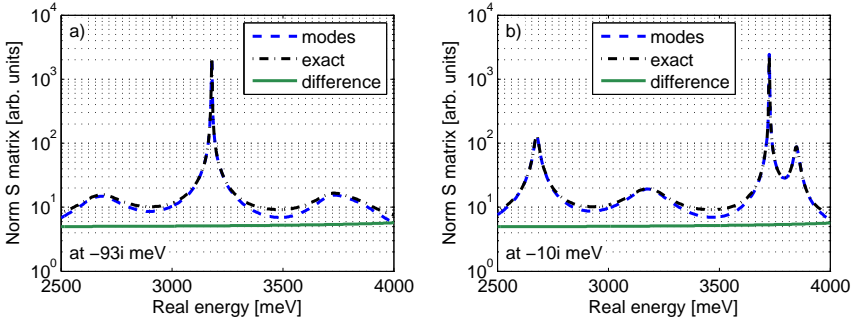

Figure 5.1: Frobenius norm of the exact scattering matrix (dashed-dotted black line) as well as the resonant contributions (dashed blue line) and the background term (solid green line) of equation (5.1) in the case of the dielectric grating described in section 4.2.1. The calculations have been carried out for a truncation order of 31 harmonics for varying energies with an imaginary part of $-93i$ meV in panel (a) and $-10i$ meV in panel (b), which equal the imaginary part of optically active resonances.

Note that other authors prefer to describe the resonant mode approximation of the scattering matrix in terms of a complex in-plane wave vector compo-

---

[1]The Frobenius norm of a square matrix M is defined as $||M|| = (\sum_{ij} |M_{ij}|^2)^{1/2}$.

nent for a fixed real energy [101, 125], but the functional dependence of their approximation is similar to the one described in this work. In the description of poles in dependence on a complex in-plane wave vector component, the imaginary part of the wave vector component provides the lateral propagation length of resonant fields that originate from the local excitation of specific modes. In contrast, our formulation with real in-plane wave vector components but complex energy is well-suited for plane wave incidence and gives access to the linewidth and the life time of the modes. Hence, it depends on the investigated problem, which description is preferable. We have mainly encountered situations with – at least approximatively – a plane wave incidence, so that we focus in this work on the description of the scattering matrix in terms of a complex energy.

We can construct the resonant mode approximation of the scattering matrix directly from the solution for the linearized equation (4.2), whenever there are only resonances very close to the linearization energy E_0. Summarizing all eigenvectors $|O_n\rangle$ of equation (4.2) as columns in a matrix $\mathbb{X}$, and constructing a diagonal matrix Δ with diagonal elements ΔE_n as the eigenvalues corresponding to the vectors $|O_n\rangle$, it is straight-forward to show that

$$\mathbb{S}^{-1}(E_0) = - \left.\frac{\partial \mathbb{S}^{-1}}{\partial E}\right|_{E_0} \mathbb{X}\Delta\mathbb{X}^{-1} . \tag{5.2}$$

By substituting equation (5.2) for $\mathbb{S}^{-1}(E_0)$ in equation (4.2), we obtain [15]:

$$\mathbb{S} \approx \mathbb{X}[(E - E_0)\mathbb{I} - \Delta]^{-1}\mathbb{Y} = \sum_n \frac{|O_n\rangle\langle I_n|}{E - E_n} . \tag{5.3}$$

In this case, $E_n = E_0 + \Delta E_n$, with ΔE_n as eigenvalues of equation (4.2) corresponding to eigenvectors $|O_n\rangle$. Furthermore, $\mathbb{Y}$ denotes a matrix consisting of row vectors $\langle I_n|$, with

$$\mathbb{Y} = \left(\left.\frac{\partial \mathbb{S}^{-1}}{\partial E}\right|_{E_0} \mathbb{X}\right)^{-1} = \begin{pmatrix} \langle I_1| \\ \langle I_2| \\ \vdots \end{pmatrix} . \tag{5.4}$$

As mentioned in chapter 4, only those eigenvectors of equation (4.2) can be considered as resonant output vectors of the scattering matrix that correspond to eigenvalues ΔE_n with a small magnitude. Hence, the corresponding resonance energy E_n is close to E_0.

Let us denote all vectors $|O_n\rangle$ and $\langle I_n|$ as well as the energies E_n with a diacritic tilde that define no resonant contribution due to $|\Delta E_n| \gg 0$. Thus, we

can split the sum on the right side of equation (5.3) into a resonant contribution and the background term $\tilde{\mathbb{S}}$:

$$\mathbb{S} \approx \underbrace{\sum_n \frac{|\tilde{O}_n\rangle\langle\tilde{I}_n|}{E - \tilde{E}_n}}_{\equiv \tilde{\mathbb{S}}} + \sum_n \frac{|O_n\rangle\langle I_n|}{E - E_n} = \tilde{\mathbb{S}}(E) + \sum_n \frac{|O_n\rangle\langle I_n|}{E - E_n} . \qquad (5.5)$$

Whenever $\tilde{E}_n \gg E$ for all n, we can neglect the energy dependence of $\tilde{\mathbb{S}}$ and evaluate it at an energy close to the resonance energies E_n.

It should be mentioned that the eigenvectors $|O_n\rangle$ in $\mathbb{X}$ are generally not orthogonal, which means that the vector $\langle O_n|$ is not defined as the Hermitean conjugate of vector $|O_n\rangle$, but as a row vector of $\mathbb{X}^{-1}$ with $\langle O_n|O_n\rangle = 1$. Similarly, $|I_n\rangle$ can be constructed as a column vector of $\mathbb{Y}^{-1}$. Note that by construction, $\tilde{\mathbb{S}}|O_n\rangle = \langle I_n|\tilde{\mathbb{S}} = 0$, whenever $|O_n\rangle$ and $\langle I_n|$ correspond to a resonant contribution of equation (5.5), because $\langle \tilde{O}_n|O_m\rangle = \langle I_n|\tilde{I}_m\rangle = 0$. Furthermore, $\langle O_m|O_n\rangle = \langle I_m|I_n\rangle = \delta_{mn}$.

In many cases, a good approximation of the scattering matrix by equation (5.1) requires that we take into account several resonances that cannot be found by a linearization around the same energy E_0. Hence, we derive in most cases only the resonant contributions from equation (5.5), whereas the background term $\tilde{\mathbb{S}}$ can be constructed by subtracting the resonance terms from an exact result of the scattering matrix, which has usually been calculated at a real energy value in the region of the relevant resonances.

5.1.2 Ansatz for resonant mode coupling

Let us assume that we have a stacked grating system with top layer 1 and bottom layer N, which contains an internal homogeneous layer that we denote by the subscript M. Then, we can separate the total system into two subsystems A and B adjacent to the internal homogeneous layer, which include the interface to layer M. The top system A and the bottom system B can be described by scattering matrices $\mathbb{S}_A = \mathbb{S}_{a1}$ and $\mathbb{S}_B = \mathbb{S}_{Nb}$, respectively. The subscript a indicates in this case the top interface of layer M, the subscript b denotes the bottom of layer M. For each of these scattering matrices, we can furthermore construct the resonant mode approximation in an energy region

of interest:

$$\mathbb{S}_A(E) \approx \underbrace{\begin{pmatrix} \tilde{\mathbb{S}}_{a1}^{++} & \tilde{\mathbb{S}}_{aa}^{+-} \\ \tilde{\mathbb{S}}_{11}^{-+} & \tilde{\mathbb{S}}_{1a}^{--} \end{pmatrix}}_{=\tilde{\mathbb{S}}_A} + \sum_n \frac{|O_n^A\rangle\langle I_n^A|}{E - E_n^A}, \tag{5.6}$$

$$\mathbb{S}_B(E) \approx \underbrace{\begin{pmatrix} \tilde{\mathbb{S}}_{Nb}^{++} & \tilde{\mathbb{S}}_{NN}^{+-} \\ \tilde{\mathbb{S}}_{bb}^{-+} & \tilde{\mathbb{S}}_{bN}^{--} \end{pmatrix}}_{=\tilde{\mathbb{S}}_B} + \sum_n \frac{|O_n^B\rangle\langle I_n^B|}{E - E_n^B}. \tag{5.7}$$

Henceforth, it is convenient to split the vectors $|O_n^A\rangle$, $|O_n^B\rangle$, $\langle I_n^A|$, and $\langle I_n^B|$ into the individual contributions of the corresponding top and bottom layers:

$$|O_n^A\rangle = \begin{pmatrix} |O_n^{a+}\rangle \\ |O_n^{1-}\rangle \end{pmatrix}, \qquad\qquad |O_n^B\rangle = \begin{pmatrix} |O_n^{N+}\rangle \\ |O_n^{b-}\rangle \end{pmatrix}. \tag{5.8}$$

$$\langle I_n^A| = \left(\langle I_n^{1+}|, \langle I_n^{a-}|\right), \qquad\qquad \langle I_n^B| = \left(\langle I_n^{b+}|, \langle I_n^{N-}|\right). \tag{5.9}$$

As in chapter 2, the $+$ and $-$ sign denote forward and backward propagation or decay, respectively.

Figure 5.2 depicts examples of stacked grating structures and provides a sketch with the orientations of the resonant output and input vectors.

Let us define the amplitude vectors for forward propagating and decaying waves at the bottom interface as $|b^+\rangle$ and denote its counterpart for backward propagating and decaying waves at the top interface as $|a^-\rangle$ in agreement with the notations of the resonant output and input vectors (see figure 5.2c). Now, we want to derive resonances of a stacked system with subsystem A on top, a homogeneous layer M with thickness L in the middle, and subsystem B at the bottom of the structure. Owing to the resonance condition of vanishing input, we can reduce equations (5.6) and (5.7) [15, 16] to

$$|b^+\rangle = \mathbb{P}_M^+ \left(\tilde{\mathbb{S}}_{aa}^{+-} + \sum_n \frac{|O_n^{a+}\rangle\langle I_n^{a-}|}{E - E_n^A} \right) |a^-\rangle, \tag{5.10}$$

$$|a^-\rangle = \mathbb{P}_M^- \left(\tilde{\mathbb{S}}_{bb}^{-+} + \sum_n \frac{|O_n^{b-}\rangle\langle I_n^{b+}|}{E - E_n^B} \right) |b^+\rangle, \tag{5.11}$$

where the matrices $\mathbb{P}_M^\pm = \exp(\pm i\Lambda_M^\pm L)$ denote the forward and backward propagation and decay inside the homogeneous layer M over a distance L, with $\Lambda_M^\pm$ being the corresponding eigenvalue matrices as defined in section 2.3.4.

Substituting the definitions

$$c_n^a \equiv \frac{1}{E - E_n^A}\langle I_n^{a-}|a^-\rangle, \qquad\qquad c_n^b \equiv \frac{1}{E - E_n^B}\langle I_n^{b+}|b^+\rangle, \tag{5.12}$$
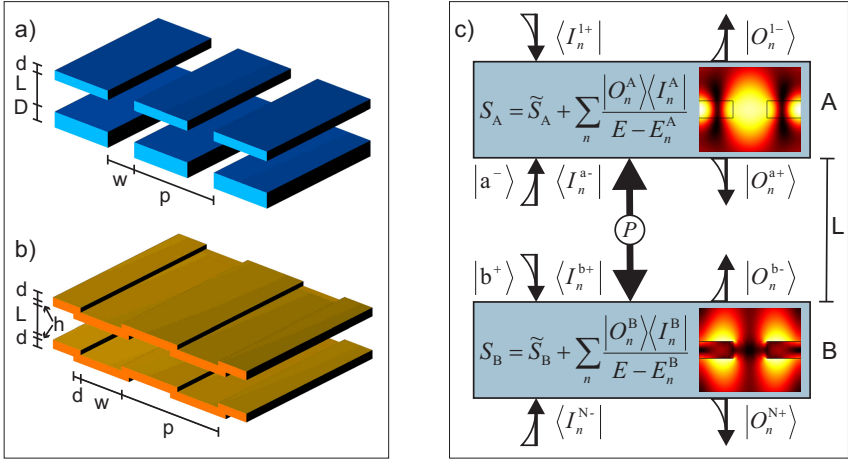
Figure 5.2: Examples of stacked grating systems; panel (a) depicts a stack of two single layer gratings, the structure in panel (b) is a stack of meanders, where each meander has to be described by at least three layers in the scattering matrix algorithm. Panel (c) displays a sketch of the resonant mode approximation for the stacked gratings.

we can formulate equations (5.10) and (5.11) as

$$\mathbb{M}\left(\begin{array}{c} |b^+\rangle \\ |a^-\rangle \end{array} \right) = \sum_n \left(\begin{array}{c} c_n^a \mathbb{P}_M^+ |O_n^{a+}\rangle \\ c_n^b \mathbb{P}_M^- |O_n^{b-}\rangle \end{array} \right), \tag{5.13}$$

with the Fabry-Perot matrix

$$\mathbb{M} = \left(\begin{array}{cc} \mathbb{I} & -\mathbb{P}_M^+ \tilde{\mathbb{S}}_{aa}^{+-} \\ -\mathbb{P}_M^- \tilde{\mathbb{S}}_{bb}^{-+} & \mathbb{I} \end{array} \right). \tag{5.14}$$

Note that $\mathbb{I}$ denotes the identity matrix.

5.1.3 Fabry-Perot matrix

In our first paper on the resonant mode coupling [15], the energy dependence of $\mathbb{M}$ has been neglected completely. Both the background terms $\tilde{\mathbb{S}}_{aa}^{+-}$ and $\tilde{\mathbb{S}}_{bb}^{-+}$ as well as the matrices $\Lambda_M^\pm$ were evaluated at a specific energy E_0 close to the resonances and kept constant. In this work, we follow reference [16], where we took the energy dependence of $\mathbb{M}$ explicitly into account.

For treating equation (5.13) further, we have to invert $\mathbb{M}$. This operation has to be carried out carefully close to Fabry-Perot resonances, as $\mathbb{M}$ becomes singular, whenever

$$\det(\mathbb{I} - \mathbb{P}_M^- \tilde{\mathbb{S}}_{bb}^{-+} \mathbb{P}_M^+ \tilde{\mathbb{S}}_{aa}^{+-}) = 0 \, . \tag{5.15}$$

This is a standard condition for Fabry-Perot resonances. Hence, Fabry-Perot resonances fulfill

$$\mathbb{M}|O^{\mathrm{FP}}\rangle = 0 \, . \tag{5.16}$$

Owing to this peculiarity, it seems to be appropriate to derive the inverse of $\mathbb{M}$ in the same way as we approximate the scattering matrix [see equation (5.1)]:

$$\mathbb{M}^{-1} \approx \tilde{\mathbb{M}} + \sum_n \frac{|O_n^{\mathrm{FP}}\rangle\langle I_n^{\mathrm{FP}}|}{E - E_n^{\mathrm{FP}}} \, . \tag{5.17}$$

Here, only a few Fabry-Perot resonances close to $E_n^{a/b}$ are taken into account explicitly. The rest is assumed to have a vanishing influence and is put into the background term $\tilde{\mathbb{M}}$. Of course, this is only a rough approximation, as we replace the periodic repetition of the Fabry-Perot resonances by a sum over only a few resonance terms.

Let us consider a stacked system with homogeneous slabs A and B, so that the different Fourier harmonics and polarizations do not interact, and we can split $\mathbb{M}$ into independent sub-blocks $\mathbb{M}_{mn}$ for each Fourier harmonic and polarization, which yield in a Cartesian coordinate system $Oxyz$:

$$\mathbb{M}_{mn} = \begin{pmatrix} 1 & r_{mn}^a \mathrm{e}^{iK_{3mn}^+ L} \\ r_{mn}^b \mathrm{e}^{iK_{3mn}^+ L} & 1 \end{pmatrix} \, . \tag{5.18}$$

By r_{mn}^a and r_{mn}^b, we denote the reflection coefficients at the top and bottom interface of layer M for internal reflections between systems A and B. Note that we find for the propagation constants K_{3mn}^+ and K_{3mn}^- of layer M due to the Cartesian coordinate system the relation $K_{3mn}^+ = -K_{3mn}^-$. Furthermore, we can reformulate equation (5.18) as follows:

$$\mathbb{M}_{mn} = \sum_{s=\pm 1} |s,m,n\rangle \left(1 + s\sqrt{r_{mn}^a r_{mn}^b}\,\mathrm{e}^{iK_{3mn}^+ L} \right) \langle s,m,n| \, . \tag{5.19}$$

In this case, the two-dimensional vectors $|s,m,n\rangle$ and $\langle s,m,n|$ obey

$$|s,m,n\rangle = \frac{1}{2\sqrt{r_{mn}^a r_{mn}^b}} \begin{pmatrix} \sqrt{r_{mn}^a} \\ s\sqrt{r_{mn}^b} \end{pmatrix} , \qquad \langle s,m,n| = \begin{pmatrix} \sqrt{r_{mn}^b}, & s\sqrt{r_{mn}^a} \end{pmatrix} \, . \tag{5.20}$$

Thus, the inverse of $\mathbb{M}_{mn}$ consists of independent 2×2 blocks

$$\mathbb{M}_{mn}^{-1} = \sum_{s=\pm 1} \frac{|s, m, n\rangle\langle s, m, n|}{1 + s\sqrt{r_{mn}^a r_{mn}^b}\, e^{iK_{3mn}^+ L}}\,. \tag{5.21}$$

We can therefore deduce that the background term $\tilde{\mathbb{M}}$ in equation (5.17) equals zero in the limit of independent propagation channels inside the two subsystems if we take into account the correct functional dependence $(1 \pm \sqrt{r_{mn}^a r_{mn}^b}\, e^{iK_{3mn}^+ L})^{-1}$ with an infinite amount of poles, which is defined for $p \in \mathbb{Z}$ by the conditions

$$\arg(r_{mn}^a) + \arg(r_{mn}^b) + 2\Re(K_{3mn}^+)L = 2\pi p\,, \qquad |r_{mn}^a||r_{mn}^b| = e^{-2\Im(K_{3mn}^+)L}\,. \tag{5.22}$$

Hence, we infer that equation (5.17) is only a good approximation close to a Fabry-Perot resonance so that we can neglect the influence of the other Fabry-Perot modes in the same subspace. On the other hand, this approximation allows us the construction of a simplified system of equations that reproduces the resonances of stacked systems correctly up to some extent.

5.1.4 Effective eigenvalue equation

Explicit inclusion of Fabry-Perot resonances

Let us assume that we can decompose the vectors $|a^-\rangle$ and $|b^+\rangle$ into Fabry-Perot contributions and background terms $|\tilde{a}^-\rangle$ and $|\tilde{b}^+\rangle$ that are linear independent:

$$|a^-\rangle = \sum_n |O_n^{\mathrm{FP}-}\rangle c_n^{\mathrm{FP}} + |\tilde{a}^-\rangle\,, \qquad |b^+\rangle = \sum_n |O_n^{\mathrm{FP}+}\rangle c_n^{\mathrm{FP}} + |\tilde{b}^+\rangle\,. \tag{5.23}$$

This ansatz has to be substituted in equation (5.12) in order to set up the desired system of equations. Furthermore, using equations (5.17) and (5.23), the inversion of $\mathbb{M}$ in equation (5.13) yields

$$\sum_n |O_n^{\mathrm{FP}}\rangle c_n^{\mathrm{FP}} + \begin{pmatrix} |\tilde{b}^+\rangle \\ |\tilde{a}^-\rangle \end{pmatrix} = \left(\tilde{\mathbb{M}} + \sum_m \frac{|O_m^{\mathrm{FP}}\rangle\langle I_m^{\mathrm{FP}}|}{E - E_m^{\mathrm{FP}}}\right) \sum_n \begin{pmatrix} c_n^a \mathbb{P}_M^+ |O_n^{a+}\rangle \\ c_n^b \mathbb{P}_M^- |O_n^{b-}\rangle \end{pmatrix}\,. \tag{5.24}$$

When constructing $\tilde{\mathbb{M}}$ in the same way as $\tilde{\mathbb{S}}$ in equation (5.5), it is evident that we can find vectors $\langle O_m^{\mathrm{FP}}|$ such that $\langle O_m^{\mathrm{FP}}|O_n^{\mathrm{FP}}\rangle = \delta_{mn}$ and $\langle O_m^{\mathrm{FP}}|\tilde{\mathbb{M}} = 0$. Considering the correct functional behavior of $\mathbb{M}^{-1}$, we can deduce from the limit of independent Fourier harmonics that this conclusion becomes incorrect, because equation (5.21) contains a periodic repetition of poles in the same

subspaces. Hence, $\langle O_m^{\mathrm{FP}}|\tilde{\mathbb{M}} \neq 0$, but it seems to be reasonable to assume that we can neglect $\langle O_m^{\mathrm{FP}}|\tilde{\mathbb{M}}$ when we are close enough to one specific resonance energy E_n^{FP}.

Using this hypothesis, we can identify c_n^{FP} in equation (5.24) by comparison of coefficients. Similarly, we can derive $|\tilde{a}^-\rangle$ and $|\tilde{b}^+\rangle$ and substitute the results in equation (5.12). Finally, we obtain:

$$(E - E_m^{\mathrm{FP}})c_m^{\mathrm{FP}} = \sum_n \langle I_m^{\mathrm{FP}+}|\mathbb{P}_M^+|O_n^{a+}\rangle c_n^a + \sum_n \langle I_n^{\mathrm{FP}-}|\mathbb{P}_M^-|O_n^{b-}\rangle c_n^b \,, \qquad (5.25)$$

$$(E - E_m^A)c_m^a = \sum_n \langle I_m^{a-}|O_n^{\mathrm{FP}-}\rangle c_n^{\mathrm{FP}} + \sum_n \langle I_m^{a-}|\tilde{\mathbb{M}}^{-+}\mathbb{P}_M^+|O_n^{a+}\rangle c_n^a$$
$$+ \sum_n \langle I_m^{a-}|\tilde{\mathbb{M}}^{--}\mathbb{P}_M^-|O_n^{b-}\rangle c_n^b \,, \qquad (5.26)$$

$$(E - E_m^B)c_m^b = \sum_n \langle I_m^{b+}|O_n^{\mathrm{FP}+}\rangle c_n^{\mathrm{FP}} + \sum_n \langle I_m^{b+}|\tilde{\mathbb{M}}^{++}\mathbb{P}_M^+|O_n^{a+}\rangle c_n^a$$
$$+ \sum_n \langle I_m^{b+}|\tilde{\mathbb{M}}^{+-}\mathbb{P}_M^-|O_n^{b-}\rangle c_n^b \,. \qquad (5.27)$$

Equations (5.25) to (5.27) define a linear eigenvalue problem with an effective non-Hermitian Hamiltonian H_{eff} [15, 16]:

$$E \begin{pmatrix} \vec{c}^{\,\mathrm{a}} \\ \vec{c}^{\,\mathrm{b}} \\ \vec{c}^{\,\mathrm{FP}} \end{pmatrix} = H_{\mathrm{eff}} \begin{pmatrix} \vec{c}^{\,\mathrm{a}} \\ \vec{c}^{\,\mathrm{b}} \\ \vec{c}^{\,\mathrm{FP}} \end{pmatrix} . \qquad (5.28)$$

The eigenvalues of H_{eff} are the approximated resonance positions of the coupled system. Note that the vector arrows indicate that we summarize all coefficients of one kind into a vector.

Schematically, we can separate the effective Hamiltonian H_{eff} into the following block matrices:

$$H_{\mathrm{eff}} = \begin{pmatrix} \Omega^a + \Delta^a & \mathrm{V}^{a,b} & \mathrm{V}^{a,\mathrm{FP}} \\ \mathrm{V}^{b,a} & \Omega^b + \Delta^b & \mathrm{V}^{b,\mathrm{FP}} \\ \mathrm{V}^{\mathrm{FP},a} & \mathrm{V}^{\mathrm{FP},b} & \Omega^{\mathrm{FP}} \end{pmatrix} . \qquad (5.29)$$

Here, Ω^ν denotes a diagonal matrix with the decoupled resonance energies of each contribution. The matrices Δ^ν can be understood as a shift of the resonance energies of subsystem A or B due to the presence of the non-resonant background of the respective other subsystem, whereas $\mathrm{V}^{\nu,\nu'}$ indicates coupling terms as the modified overlap integrals of the resonant input and output vectors.

It should be mentioned that equation (5.28) is usually of a small dimensionality that equals the total number of relevant resonances. Therefore, we can

find the solution of the eigenvalue problem very fast. In addition, we need to compute the resonances of the subsystems only once in order to approximate the coupled resonances for various inter-grating distances, because the dependence of $\mathbb{P}_M^{\pm}$ on the distance is trivial and the Fabry-Perot modes can be found rather quickly.

Weak coupling to Fabry-Perot resonances

As mentioned above, the accuracy of the resonant mode coupling depends on the appropriate formulation of the inverse of the Fabry-Perot matrix $\mathbb{M}$. In some cases, it is sufficient to evaluate $\mathbb{M}$ at a specific energy and invert it directly without considering explicit Fabry-Perot terms [15] in order to obtain the simplified effective Hamiltonian

$$H_{\text{eff}}^{\text{weak}} = \begin{pmatrix} \Omega^a + \Delta^a & V^{\text{a,b}} \\ V^{\text{b,a}} & \Omega^b + \Delta^b \end{pmatrix} . \tag{5.30}$$

A necessary condition for the validity of $H_{\text{eff}}^{\text{weak}}$ is a merely weak coupling between Fabry-Perot resonances and the grating resonances, as it is shown in the following numerical examples.

5.2 Numerical examples

We present in this section a variety of numerical examples, where each subsystem A and B corresponds to one of the one-dimensional examples of chapter 4. It should be mentioned that the method is not limited to one-dimensional structures, but can handle also structures that are periodic in two directions. However, in that case, the derivation of the exact results is rather time-consuming, so that we focus here on simpler examples.

5.2.1 Optically inactive resonances

In the first place, let us focus on optically inactive resonances. We know that these resonances do not interact with the far field, and we can neglect the Fabry-Perot resonances in the resonant mode coupling. Hence, we discuss only results derived by equation (5.30).

Planar waveguide slab

As mentioned earlier in section 4.2.1, a homogeneous planar waveguide slab exhibits optically inactive resonances, which lie outside the light cone. We have chosen a system, where each waveguide is surrounded by air and consists of a

dielectric medium with a refractive index of $n = 2.5$ and a thickness of $50\,\mathrm{nm}$, similar to the dielectric grating of section 4.2.1. The bare waveguide resonance of a single waveguide is located for an in-plane wavenumber of $k_{||} = 28\,\mu\mathrm{m}^{-1}$ in TM polarization at $4301\,\mathrm{meV}$. The results of the coupling equation (5.30) are shown in figure 5.3a for a varying spacer thickness from $10\,\mathrm{nm}$ to $200\,\mathrm{nm}$ and agree very well with the analytical results available for these systems.
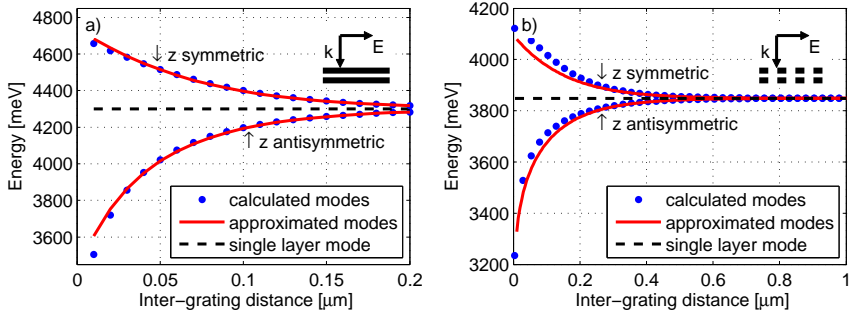
Figure 5.3: Comparison between exact results of optically inactive modes and the resonant mode coupling for a stack of planar waveguide slabs in panel (a) and a dielectric grating in panel (b).

We see a large mode splitting for small inter-grating distances, where the lower branch exhibits an antisymmetric electric field distribution with respect to the stacking direction, the upper branch is symmetric. For larger distances, both branches approach the resonance energy of the single layer.

Dielectric grating

When considering the dielectric grating of section 4.2.1 instead of a homogeneous slab, we have found an optically inactive TM polarized mode, which is located at $3849\,\mathrm{meV}$ for $k_1 = k_2 = 0$ (see figure 4.5b). If we place the same grating with a certain horizontal distance but no lateral shift below the first layer, we do not break the general symmetry, so that the coupled modes remain optically inactive. Hence, the distance dispersion is very similar to the case of the stacked homogeneous waveguide slabs, and we can approximate the exact mode behavior very well by the resonant mode coupling from small to large inter-grating distances (see figure 5.3b).

5.2.2 Symmetric dielectric grating stack

TM polarization

Let us now consider the optically active TM resonance of the dielectric grating discussed in section 5.2.1. The single layer exhibits an optically active resonance at $3725 - 10i$ meV, which leads in contrast to the optically inactive modes to an oscillating behavior in the distance dispersion at larger inter-grating distances (see blue dots in figure 5.4).
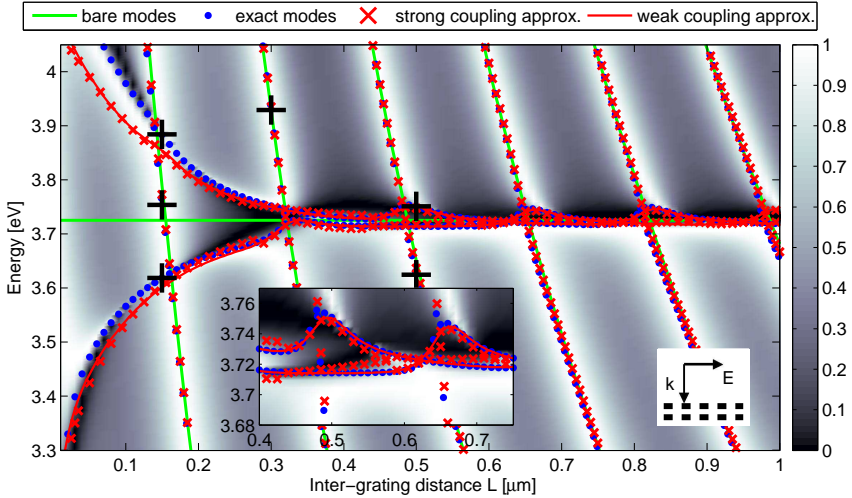

Figure 5.4: Distance dispersion of coupled resonances in a stack of identical dielectric gratings. The background denotes transmittance spectra in TM polarization. Solid green lines depict the position of the resonances of each subsystem as well as the Fabry-Perot modes. The exact mode position of the coupled system is shown by blue dots. We observe an oscillating behavior for larger distances, which is caused by a weak coupling between grating and Fabry-Perot resonances, and is better reproduced in the resonant mode coupling without Fabry-Perot terms in equation (5.17) denoted by thin red solid lines. However, the explicit inclusion of the Fabry-Perot resonances in the resonant mode coupling (red crosses) provides also a good estimation of the exact resonance position. Black crosses mark positions of the field distributions shown in figures 5.5 and 5.6.

The reason for the oscillating behavior is a weak coupling to the occurring Fabry-Perot resonances that are formed by the multiple reflections between the top and the bottom grating. Both the resonant mode coupling with [equation (5.28)] and without [equation (5.30)] explicit Fabry-Perot resonances can

reproduce the exact behavior qualitatively. However, the results without the explicit Fabry-Perot terms exhibit a better agreement with the exact results.

Figure 5.5 provides three examples of typical resonant field distributions of Fabry-Perot modes, which can be clearly distinguished by the number of nodes between the two gratings. As it can be seen in panels (a) and (d) of figure 5.5, Fabry-Perot modes with an even number of nodes are symmetric with respect to the horizontal symmetry plane of the structure (see white dashed line in figure 5.5), whereas Fabry-Perot modes with an odd number of nodes are antisymmetric (see figure 5.5b).
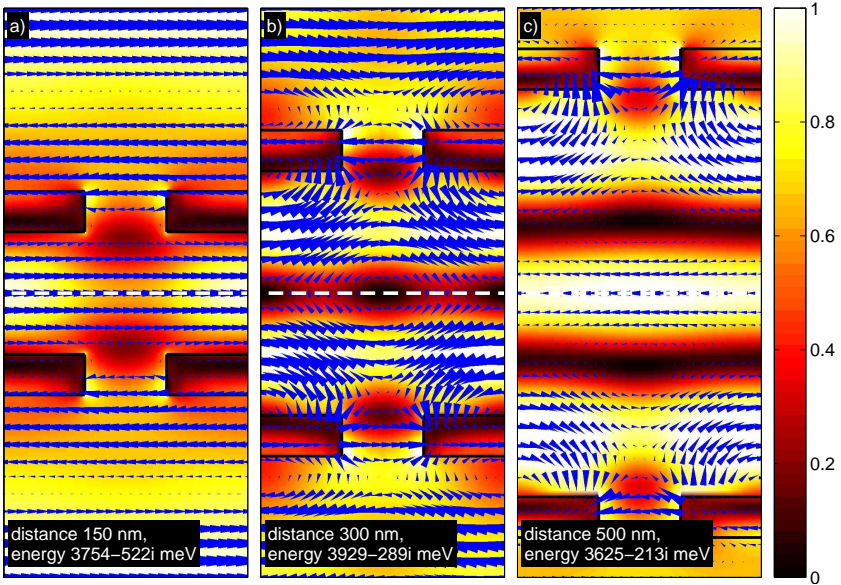
Figure 5.5: Electric field distribution of Fabry-Perot modes for a stack of identical dielectric gratings, calculated without external excitation. The background color denotes the time averaged energy density of the electric field in a normalized logarithmic scale. White dashed lines depict the symmetry plane of the stacked system.

The resonant field distributions of waveguide modes can be seen in figure 5.6. Similarly to the Fabry-Perot modes, the occurring waveguide resonances are either symmetric or antisymmetric with respect to the horizontal symmetry plane of the structure. In particular, the field distributions in panel (a) and (b) can be clearly identified as the antisymmetric and symmetric combination of the single waveguide modes depicted in figure 4.5a, respectively.

Even the field distribution in panel (c) exhibits more or less a linear com-
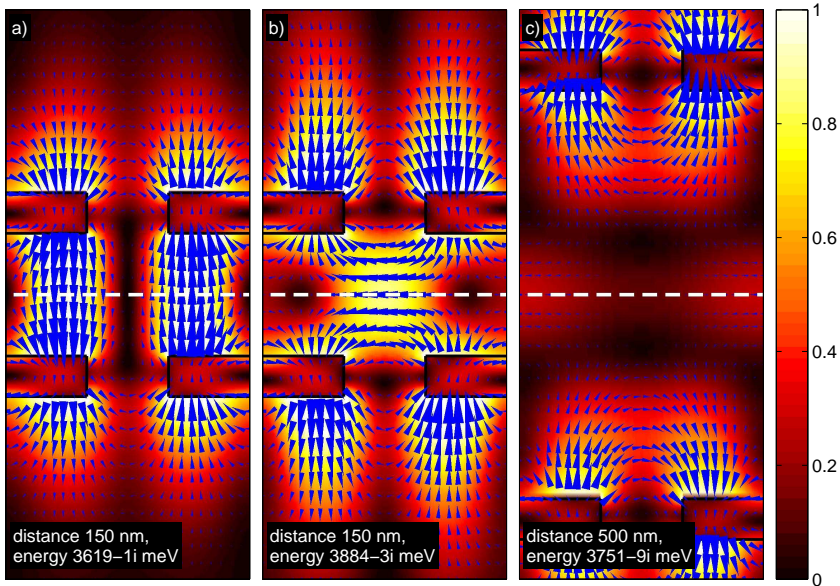
Figure 5.6: Electric field distribution of coupled waveguide modes occurring in a stack of identical dielectric gratings. Colors and symbols are as in figure 5.5.

bination of the resonances occurring in each single layer, although the field distribution has been derived at a position with maximum deviation from the resonance energy of a single layer. The deviation from the single layer resonance position can be attributed to the weak coupling to the nearest Fabry-Perot branch (see figure 5.4), which exhibits the same symmetry behavior as the combined waveguide mode (compare figure 5.5c and figure 5.6c).

TE polarization

When we focus on TE polarization for the stack of the dielectric gratings discussed in the previous section, we observe no longer a weak coupling between Fabry-Perot and optically active waveguide resonances, but the coupling becomes strong, manifested in an anticrossing behavior of the respective branches (see figure 5.7).

For small distances, the behavior is dominated by the waveguide modes originating from the single subsystems A and B. We observe two branches that exhibit a large splitting which decreases with increasing inter-grating distance. Around 100 nm distance, the situation changes, as the modes approach the

first Fabry-Perot resonance. We can clearly see an anticrossing behavior in the case of the lower branch that has an antisymmetric magnetic mode profile in stacking direction (see figure 5.8a). The upper branch with a symmetric profile (see figure 5.8c) is not affected by the first Fabry-Perot mode, but strongly interacts with the next one. This alternation between crossing and anticrossing repeats periodically with increasing inter-grating distance.
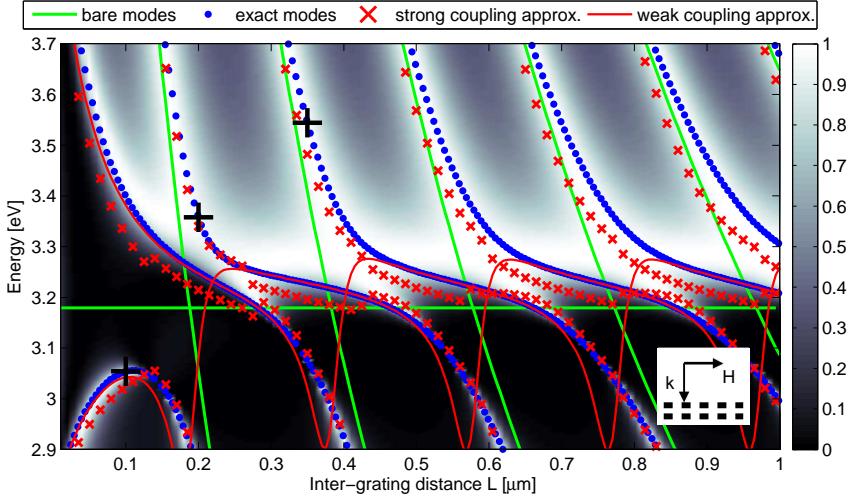

Figure 5.7: Coupled resonances in a stack of identical dielectric gratings for varying inter-grating distance. The background denotes transmittance spectra in TE polarization. Lines and symbols are as in figure 5.4. The comparison between resonant mode coupling with (red crosses) and without (thin red solid lines) Fabry-Perot terms in equation (5.17) reveals a clearly improved agreement with the exact modes (blue dots) when including the Fabry-Perot resonances explicitly. Black crosses mark the positions of the field distributions shown in figure 5.8.

The reason for the strong coupling of Fabry-Perot and waveguide modes in TE polarization is a large coupling term $V^{\nu,\nu'}$ in equation (5.29) with a magnitude that is at least comparable to the distance $|E^\nu - E^{\nu'}|$ of the involved resonance energies. First of all, the Fabry-Perot resonances are governed mostly by the fundamental harmonic of the plane wave expansion in the intermediate layer. Second, the TE mode can couple much more efficiently to the far field, and, thus, to the fundamental harmonic than the TM mode. In addition, the bare TM waveguide mode is located at $3725 - 10i$ meV with a much smaller linewidth than in TE polarization, whereas the linewidth of the

Fabry-Perot modes is in the same order of magnitude for both polarizations. Hence, the coupling between TE waveguide modes and Fabry-Perot modes is much stronger.[2]

When we try to approximate the position of the coupled modes by neglecting the Fabry-Perot terms of equation (5.17), we cannot reproduce correctly the behavior at the crossing of the Fabry-Perot modes and the position of the bare waveguide mode (compare blue dots as exact mode positions and the thin solid line as the resonant mode coupling in figure 5.7). In contrast, the formulation of the resonant mode coupling with explicit Fabry-Perot terms (red crosses) exhibits a good agreement with the exact mode positions.
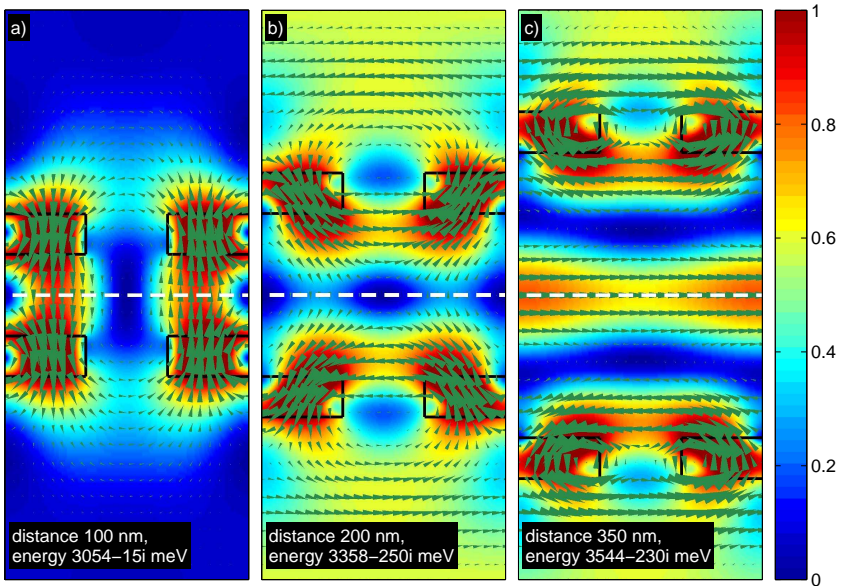

Figure 5.8: Magnetic field distributions of combined modes for a stack of identical dielectric gratings, calculated without external excitation. The background color denotes the time averaged energy density of the magnetic field in a normalized logarithmic scale. White dashed lines depict the symmetry plane of the stacked system.

Note that we consider for each distance in the resonant mode coupling with Fabry-Perot terms only up to two Fabry-Perot resonances, which are close to the bare grating modes. Hence, the inter-grating dispersion of the resonant

---

[2] For larger distances around $2\,\mu$m, we observe also strong coupling in TM polarization, because the linewidth of the Fabry-Perot modes approaches the linewidth of the TM modes, as it roughly scales with the inverse of the inter-grating distance L.

mode coupling exhibits discontinuities, whenever we exchange the involved Fabry-Perot terms. These discontinuities arise from the assumed energy dependence of the inverse Fabry-Perot matrix in equation (5.17), which neglects completely the periodic repetition of the Fabry-Perot modes [see equation (5.21)] and becomes less accurate far away from the Fabry-Perot resonances.

Another limitation of the resonant mode coupling is the resonant mode approximation of the involved scattering matrices, which fails when passing the opening of the first diffraction order around $4133\,\text{meV}$ (not shown in figure 5.7). Hence, we can trace the Fabry-Perot modes only up to that limit. However, a detailed discussion on this problem is beyond the scope of this work.
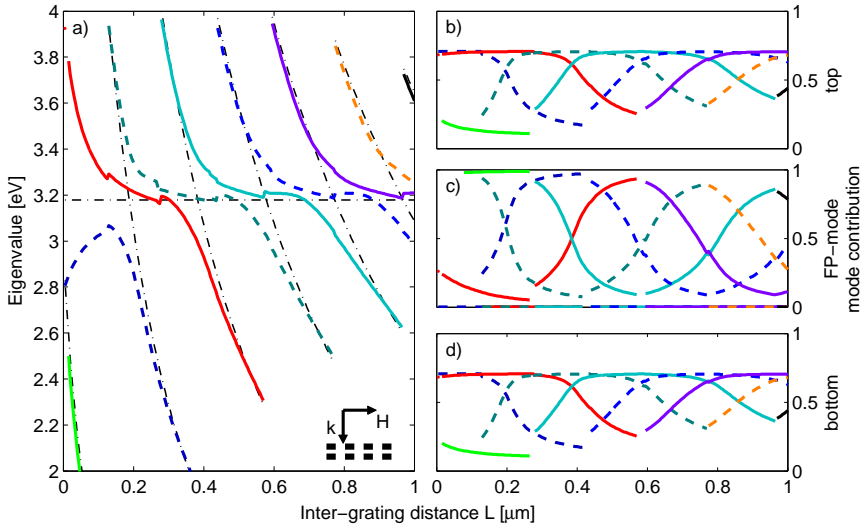

Figure 5.9: Real part of the eigenvalues (see also red crosses in figure 5.7) and composition of the eigenvectors from equation (5.28) for the different coupled modes in the case of a stack of identical dielectric gratings, indicated by the absolute value. Values close to one mean a dominating influence of the individual waveguide or FP modes. Thin black dashed-dotted lines indicate the uncoupled resonances.

It should be mentioned that the resonant mode coupling not only allows us to predict the resonance positions effectively, but also to gain additional insight into the coupling of the involved resonances, because we can analyze the individual contributions in equation (5.29). Furthermore, we can decompose the eigenvectors of equation (5.28) into their individual contributions, as shown in figure 5.9 by depicting the absolute values of the eigenvector components in panels (b-d). Closer to the energy of the single grating mode and for distances

below 200 nm, the resulting coupled modes can be considered more or less as a linear combination of the single grating modes. For larger or smaller energies, the coupled modes have predominantly the character of a Fabry-Perot mode.

Note the branch in the lower left corner of figure 5.9 that exhibits a dispersion similar to the other Fabry-Perot branches, except that it seems to approach a finite energy instead of growing to infinity at zero distance. It is definitely an interesting task for the future to study the mode dispersion for vanishing inter-grating distances in detail, which may require including non-locality [92].

5.2.3 Asymmetric dielectric grating stack

In the previous section, the two grating layers had an identical thickness. Thus, the system exhibited a mirror symmetry in stacking direction, which led to the peculiar alternation of crossing and anticrossing between grating and Fabry-Perot modes. Let us now consider an asymmetric configuration by decreasing the thickness of the upper waveguide to $d = 30$ nm (see figure 5.2). All other parameters are chosen as in section 5.2.2. The bare TE resonance of the thinner grating is located at $3503 - 100i$ meV.
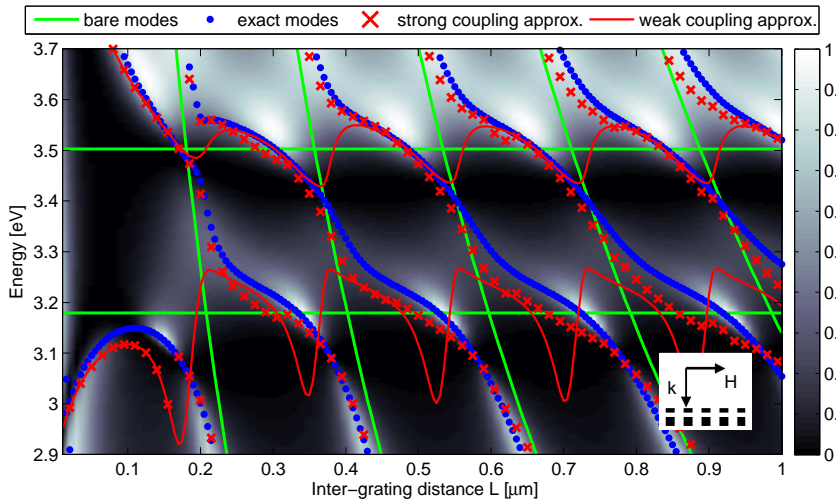

Figure 5.10: Distance dispersion of coupled resonances in an asymmetric stack consisting of a thin and a thick dielectric grating layer. The background denotes transmittance spectra in TE polarization. Lines and symbols are as in figure 5.4.

Due to the symmetry breaking, we observe a distinct difference in the behavior of the coupled modes. As seen in figure 5.10, every branch exhibits a strong coupling to the Fabry-Perot resonances. Again, this behavior is very well reproduced by the extended resonant mode coupling with explicit Fabry-Perot terms [see equation (5.28)].

As in the case of the symmetric grating stack, we can analyze the different mode contributions in detail. However, the situation is more complicated in the case of the asymmetric configuration (see figure 5.11).

When looking at the contribution of the single waveguide modes originating from the top or bottom grating, we can find an antipodal behavior in each coupled resonance. When the coupled resonance is close to the resonance energy of the bare top or bottom grating, the dominating contribution is of course from the respective mode.
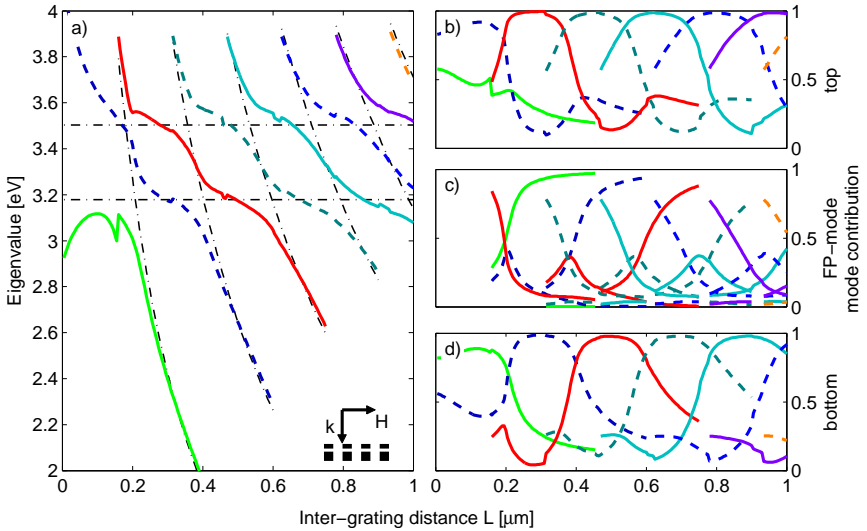

Figure 5.11: Real part of the eigenvalues (see also red crosses in figure 5.10) and composition of the eigenvectors from equation (5.28) for the different coupled modes in the case of a stack of two dielectric gratings with different thickness, indicated by the absolute value. Thin black dashed-dotted lines depict the uncoupled resonances.

In the case of the Fabry-Perot contribution, let us start with a coupled branch in the upper left corner of figure 5.11a. At a distance of 200 nm and an energy of 3800 meV, one particular Fabry-Perot mode is dominating the physical phenomena (see figure 5.11c). Approaching the resonance energy of the

thinner top grating, its influence vanishes. Between the two waveguide modes, another Fabry-Perot branch becomes important, but immediately vanishes when approaching the resonance position of the bottom grating. For smaller energies, the contribution of the subsequent Fabry-Perot branch increases.

5.2.4 Coupling of stacked metallic meander layers

Let us consider the example of a metallic meander layer as described in section 4.2.3 in order to show the validity of the resonant mode coupling in the case of metals. For the sake of simplicity, we choose the top system A and the bottom system B to be completely identical, with parameters as in section 4.2.3.
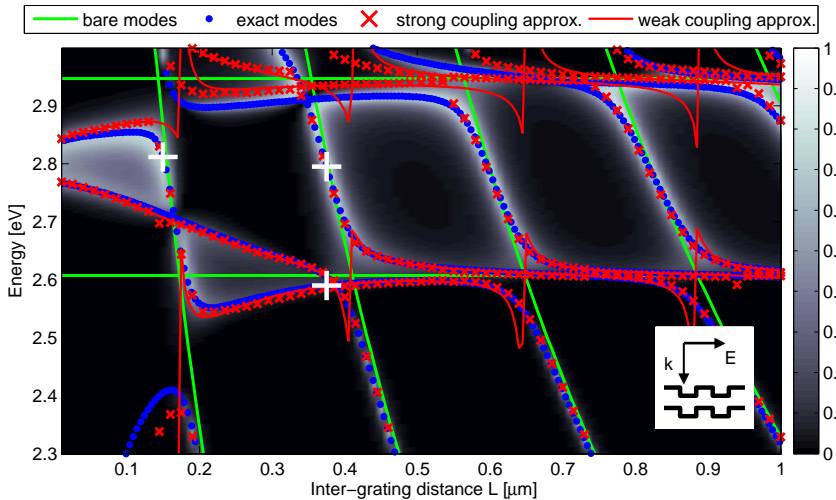

Figure 5.12: Exact and approximated mode dispersion for a stack of identical metallic meanders in TM polarization. Colors and lines are as in figure 5.4. White crosses mark the positions of the field distributions shown in figure 5.13.

In the case of the stacked meander system, we can see for small inter-grating distances and energies below 2800 meV two largely split branches in figure 5.12 that originate predominantly from the C_2 symmetric surface plasmon polariton at $2607 - 23i$ meV (see figure 4.9a) with a negligible contribution from the C_2 antisymmetric surface plasmon polariton (see figure 4.9b). Another branch around 2850 meV comes mainly from the C_2 antisymmetric surface plasmon polariton of the single meander layer, for which we determined a resonance

energy of $2947 - 18i$ meV. The uppermost C_2 antisymmetric surface plasmon polariton branch is beyond the opening of the first diffraction order, so that we cannot approximate its behavior by the resonant mode coupling properly. The splitting between the branches decreases when increasing the inter-grating distance until we reach the first Fabry-Perot branch.

As in the case of the symmetric waveguide, we observe either a crossing or anticrossing behavior when following each branch to larger distances. In contrast to the mirror symmetry of the symmetric dielectric grating stack described in section 5.2.2, the avoided crossing is attributed to a C_2 symmetry with a center of rotation in the middle of the grating (see field distributions in figure 5.13). The electric field distributions of the Fabry-Perot branches with an odd number of nodes between the meander layers are symmetric under rotation by $180°$, whereas even Fabry-Perot modes exhibit an antisymmetry. Depending on the C_2 symmetry of the combined surface plasmon polariton branches (see figure 5.13), we observe either crossing or anticrossing.
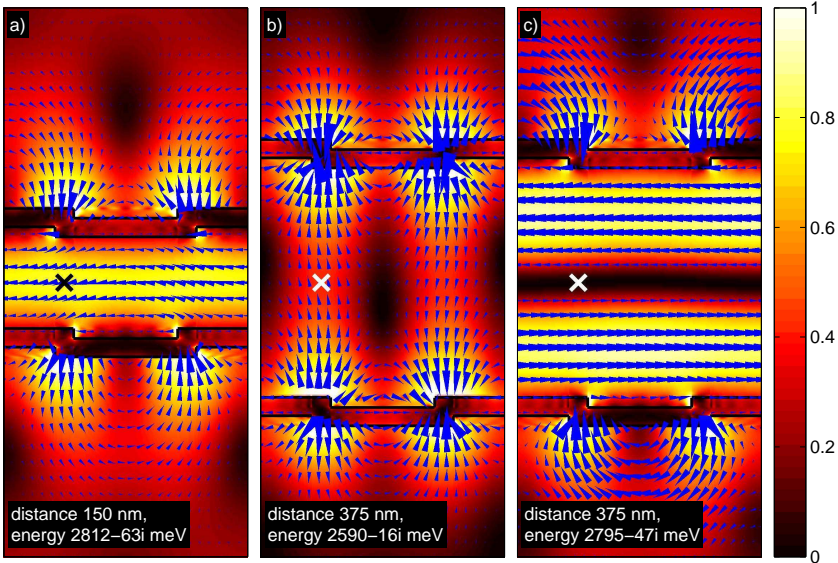

Figure 5.13: Electric field distribution of combined modes for a meander stack, calculated without external excitation. The background color denotes the time averaged energy density of the electric field in a normalized logarithmic scale. The C_2 rotation center is indicated by crosses.

Following one branch, it can be seen from figure 5.13 that the characteristic

of the branches changes in dependence on the inter-grating distance between strong surface plasmon polariton contribution in panel (b) and strong Fabry-Perot contribution in panel (c).

As in the dielectric examples, the extended resonant mode coupling can reproduce the qualitative behavior correctly, including the alternation of crossing and anticrossing due to the C_2 symmetry. Note that the simpler method without explicit Fabry-Perot terms (see thin solid lines in figure 5.12) fails at the crossing of Fabry-Perot and surface plasmon polariton modes of single meander layers.

6 Conclusion and outlook

In this work, we have shown that it is possible to include curvilinear coordinate systems easily in the Fourier modal method when we formulate Maxwell's equations in a covariant form [37]. Moreover, if we choose the coordinate transformation such that all interfaces can be described in the curvilinear coordinate system by surfaces of constant coordinates, we can apply the correct Fourier factorization rules in combination with adaptive spatial resolution for an optimized convergence behavior. Through this concept of matched coordinates, even in the case of metallo-dielectric structures, we are able to calculate the scattering matrix of a given geometry with a high accuracy at low computational cost. The scheme has been validated for numerous examples such as circular and hexagonal cylinders as well as rotated elements and bowties.

In the future, we should also benefit from the symmetry properties of the investigated structures and implement the group theoretic approach of Bai and Li in order to reduce the calculation time for the involved eigenvalue problems [87–91]. Furthermore, it is of general interest to extend the Fourier modal method with matched coordinates to aperiodic structures [82–84] and nonlinear material response [85, 86].

One of the most challenging problems will be the usage of different coordinate transformations in different layers. According to our experience, the simple ansatz of Vallius and Honkanen [104] with a projection of basis functions of one Fourier space on the Fourier basis of the other coordinate system is not very stable. A promising alternative may be an extension of the Legendre expansion method by Khavasi et al. [126]. Thus, we would be able to overcome the restriction of translation invariance inside each layer, so that we could change the coordinate system for the description of Maxwell's equations smoothly from one layer to the other in cases when there is a homogeneous spacer layer in between. In addition, we can develop a kind of three dimensional system of matched coordinates in order to calculate the optical properties of complex systems such as spheres or spirals, which cannot be derived with the standard Fourier modal method.

In any case, once the scattering matrix has been derived for a specific structure, we have shown in this work how to efficiently derive the optical resonances of a system directly from the scattering matrix [14]. The presented linearization of the inverse scattering matrix is very stable and easy to implement. We have described the method in general and shown in particular, how to warrant the continuity of the inverse scattering matrix when expanding it into its Taylor series up to the linear order. In addition, we have presented var-

ious examples, including the resonant field distributions of optically inactive resonances.

The only problem with the mode solver is an instability occurring for larger truncation orders due to the inversion of a nearly singular matrix. In order to avoid this problem, we have started to alternatively search the optical resonances by a separation of a complete system into two subsystem. From the exact scattering matrices of both subsystems, we can then construct a matrix similar to that in the determinant of equation (5.15), from which we can derive the resonances in the same way as from the inverse scattering matrix. First results are quite promising, but the downside of this approach is that it may be necessary to introduce in some cases an artificial homogeneous layer of vanishing thickness in order to warrant the continuity of the occurring matrices with respect to energy.

Knowing the resonances of a system, it is well-known that we can approximate the scattering matrix by its resonant mode approximation [99, 101, 125], where the resonances are described as poles of order one. We have used this approximation as a starting point for the derivation of coupling equations that allow us to estimate the resonances in a stacked two-layer system when knowing the relevant resonances of both subsystems in the stack [15, 16]. We have shown in this work that the method provides a good approximation of the exact resonance positions from the near to the far field regime. With some extensions, we can even describe the strong coupling of the single layer resonances to Fabry-Perot resonances, which are formed between the two subsystems in the far field region.

So far, the so-called resonant mode coupling works very efficient, whenever the coupling between Fabry-Perot resonances and single layer resonances remains weak. Some more work should be devoted in the future to a better approximation of the Fabry-Perot contribution in order to improve the agreement to the exact resonance positions, but already the current method provides a good estimation of the coupled resonances for many practical systems.

Bibliography

[1] T. F. Krauss, R. M. DeLaRue, and S. Brand, "Two-dimensional photonic-bandgap structures operating at near-infrared wavelengths," Nature **383**, 699–702 (1996).

[2] W. L. Barnes, S. C. Kitson, T. W. Preist, and J. R. Sambles, "Photonic surfaces for surface-plasmon polaritons," J. Opt. Soc. Am. A **14**, 1654–1661 (1997).

[3] W. L. Barnes, A. Dereux, and T. W. Ebbesen, "Surface plasmon subwavelength optics," Nature **424**, 824–830 (2003).

[4] E. Popov, S. Enoch, G. Tayeb, M. Neviere, B. Gralak, and N. Bonod, "Enhanced transmission due to nonplasmon resonances in one- and two-dimensional gratings," Applied Optics **43**, 999–1008 (2004).

[5] D. N. Chigrin, A. V. Lavrinenko, and C. M. . S. Torres, "Nanopillars photonic crystal waveguides," Opt. Express **12**, 617–622 (2004).

[6] W. L. Barnes, "Surface plasmon-polariton length scales: A route to subwavelength optics," J. Opt. A: Pure Appl. Opt. **8**, S87–S93 (2006).

[7] C. Rockstuhl, T. Zentgraf, H. Guo, N. Liu, C. Etrich, I. Loa, K. Syassen, J. Kuhl, F. Lederer, and H. Giessen, "Resonances of split-ring resonator metamaterials in the near infrared," Appl. Phys. B **84**, 219–227 (2006).

[8] M. Husnik, M. W. Klein, N. Feth, M. König, J. Niegemann, K. Busch, S. Linden, and M. Wegener, "Absolute extinction cross-section of individual magnetic split-ring resonators," Nature Photonics **2**(10), 614–617 (2008).

[9] N. Liu, H. Liu, S. Zhu, and H. Giessen, "Stereometamaterials," Nature Photonics **3**, 157–162 (2009).

[10] L. Li, "Fourier modal method for crossed anisotropic gratings with arbitrary permittivity and permeability tensors," J. Opt. A: Pure Appl. Opt. **5**, 345–355 (2003).

[11] T. Weiss, G. Granet, N. A. Gippius, S. G. Tikhodeev, and H. Giessen, "Matched coordinates and adaptive spatial resolution in the Fourier modal method," Opt. Express **17**, 8051–8061 (2009).

[12] G. Granet, "Reformulation of the lamellar grating problem through the concept of adaptive spatial resolution," J. Opt. Soc. Am. A **16**, 2510–2516 (1999).

[13] G. Granet and J. P. Plumey, "Parametric formulation of the Fourier modal method for crossed surface-relief gratings," J. Opt. A: Pure Appl. Opt. **4**, S145–S149 (2002).

[14] T. Weiss, N. A. Gippius, S. G. Tikhodeev, G. Granet, and H. Giessen, "Derivation of plasmonic resonances in the Fourier modal method with adaptive spatial resolution and matched coordinates," J. Opt. Soc. Am. A **28**, 238–244 (2011).

[15] N. A. Gippius, T. Weiss, S. G. Tikhodeev, and H. Giessen, "Resonant mode coupling of optical resonances in stacked nanostructures," Opt. Express **18**, 7569–7574 (2010).

[16] T. Weiss, N. A. Gippius, G. Granet, S. G. Tikhodeev, R. Taubert, L. Fu, H. Schweizer, and H. Giessen, "Strong resonant mode coupling of Fabry-Perot and grating resonances in stacked two-layer systems," Photonics and Nanostructures **published online** (2011).

[17] J. C. Maxwell, "A dynamical theory of the electromagnetic field," Philosophical Transactions of the Royal Society of London **155**, 459–512 (1865).

[18] S. John, "Strong localization of photons in certain disordered dielectric superlattices," Phys. Rev. Lett. **58**, 2486–2489 (1987).

[19] E. Yablonovitch, "Inhibited spontaneous emission in solid-state physics and electronics," Phys. Rev. Lett. **58**, 2059–2062 (1987).

[20] E. Yablonovitch, T. J. Gmitter, and K. Leung, "Photonic band structure: The face-centered-cubic case employing nonspherical atoms," Phys. Rev. Lett. **67**, 2295–2298 (1991).

[21] K. Sakoda, *Optical properties of photonic crystals*, 1st ed. (Springer, 2005).

[22] C. Kittel, *Introduction to solid state physics*, seventh ed. (John Wiley & Sons, New York, 1995).

[23] A. Mekis, J. C. Chen, I. Kurland, S. Fan, P. R. Villeneuve, and J. D. Joannopoulos, "High transmission through sharp bends in photonic crystal waveguides," Phys. Rev. Lett. **77**, 3787–3790 (1996).

[24] P. S. J. Russell, "Photonic crystal fibers," Science **299**, 358–362 (2003).

[25] O. Painter, R. K. Lee, A. Scherer, A. Yariv, J. D. O'Brien, P. D. Dapkus, and I. Kim, "Two-dimensional photonic band-gap defect mode laser," Science **284**, 1819–1824 (1999).

[26] J. B. Pendry, "Negative refraction makes a perfect lens," Phys. Rev. Lett. **85**, 3966–3969 (2000).

[27] J. B. Pendry, D. Schurig, and D. R. Smith, "Controlling electromagnetic fields," Science **312**, 1780–1782 (2006).

[28] D. Schurig, J. J. Mock, B. J. Justice, S. A. Cummer, J. B. Pendry, A. F. Starr, and D. R. Smith, "Metamaterial electromagnetic cloak at microwave frequencies," Science **314**, 977–979 (2006).

[29] A. Sihvola, "Metamaterials in electromagnetics," Metamaterials **1**, 2–11 (2007).

[30] C. Rockstuhl, C. Menzel, T. Paul, and F. Lederer, "Optical activity in chiral media composed of three-dimensional metallic meta-atoms," Phys. Rev. B **79**, 035,321–1–5 (2009).

[31] V. G. Veselago, "The electrodynamics of substances with simultaneously negative values of ε and μ," Sov. Phys. Usp. **10**, 509–514 (1968).

[32] V. Podolskiy, A. Sarychev, and V. Shalaev, "Plasmon modes and negative refraction in metal nanowire composites," Opt. Express **11**, 735–745 (2003).

[33] G. Dolling, M. Wegener, C. M. Soukoulis, and S. Linden, "Design-related losses of double-fishnet negative-index photonic metamaterials," Optics Express **15**, 11,536–11,541 (2007).

[34] J. Valentine, S. Zhang, T. Zentgraf, E. Ulin-Avila, D. A. Genov, G. Bartal, and X. Zhang, "Three-dimensional optical metamaterial with a negative refractive index," Nature **455**, 376–379 (2008).

[35] J. Valentine, J. Li, T. Zentgraf, G. Bartal, and X. Zhang, "An optical cloak made of dielectrics," Nature Materials **8**, 568–571 (2009).

[36] U. Leonhardt and T. G. Philbin, "Transformation optics and the geometry of light," vol. 53 of *Progress in Optics*, chap. 2, pp. 69 – 152 (Elsevier, 2009).

[37] E. J. Post, *Formal structure of electromagnetism* (North Holland, Amsterdam, 1962).

[38] N. Liu, H. Guo, L. Fu, H. Schweizer, S. Kaiser, and H. Giessen, "Electromagnetic resonances in single and double split-ring resonator metamaterials in the near infrared spectral region," Phys. stat. sol. (b) **244**, 1251–1255 (2007).

[39] N. Liu, H. Guo, L. Fu, S. Kaiser, H. Schweizer, and H. Giessen, "Plasmon hybridization in stacked cut-wire metamaterials," Advanced Materials **19**, 3628–3632 (2007).

[40] N. Liu, H. Guo, L. Fu, S. Kaiser, H. Schweizer, and H. Giessen, "Realization of three-dimensional photonic metamaterials at optical frequencies," Nature Materials **7**, 31–37 (2008).

[41] N. Liu and H. Giessen, "Three-dimensional optical metamaterials as model systems for longitudinal and transverse magnetic coupling," Opt. Express **16**, 21,233–21,238 (2008).

[42] J. K. Gansel, M. Thiel, M. S. Rill., M. Decker, K. Bade, V. Saile, G. von Freymann, S. Linden, and M. Wegener, "Gold helix photonic metamaterial as broadband circular polarizer," Science **325**, 1513–1515 (2009).

[43] M. Decker, R. Zhao, C. M. Soukoulis, S. Linden, and M. Wegener, "Twisted split-ring-resonator photonic metamaterial with huge optical activity," Optics Letters **35**, 1593–1595 (2010).

[44] N. Papasimakis, V. A. Fedotov, N. I. Zheludev, and S. L. Prosvirnin, "Metamaterial analog of electromagnetically induced transparency," Phys. Rev. Lett. **101**, 253,903–1–4 (2008).

[45] N. Liu, T. Weiss, M. Mesch, L. Langguth, U. Eigenthaler, M. Hirscher, C. Sönnichsen, and H. Giessen, "Planar metamaterial analogue of electromagnetically induced transparency for plasmonic sensing," Nano Letters **10**, 1103–1107 (2010).

[46] N. Liu, M. Mesch, T. Weiss, M. Hentschel, and H. Giessen, "Infrared perfect absorber and its application as plasmonic sensor," Nano Letters **10**, 2342–2348 (2010).

[47] N. Liu, M. Hentschel, T. Weiss, A. P. Alivisatos, and H. Giessen, "Three-dimensional plasmon rulers," Science **332**, 1407–1410 (2010).

[48] A. B. Akimov, A. S. Vengurlekar, T. Weiss, N. A. Gippius, and S. G. Tikhodeev, "Surface plasmon polaritons in metallo-dielectric meander-type gratings," Pisma ZhETF **90**, 398–401 (2009).

[49] M. I. Stockman, S. V. Faleev, and D. J. Bergman, "Localization versus delocalization of surface plasmons in nanosystems: Can one state have both characteristics?" Phys. Rev. Lett. **87**, 167,401–1–14 (2001a).

[50] E. Prodan, C. Radloff, N. J. Halas, and P. Nordlander, "A hybridization model for the plasmon response of complex nanostructures," Science **302**, 419–422 (2003).

[51] D. Dregely, R. Taubert, J. Dorfmüller, R. Vogelgesang, K. Kern, and H. Giessen, "3D optical Yagi-Uda nanoantenna-array," Nat. Commun. **2**, 267–1–7 (2011).

[52] A. G. Curto, G. Volpe, T. H. Taminiau, M. P. Kreuzer, R. Quidant, and N. F. van Hulst, "Unidirectional emission of a quantum dot coupled to a nanoantenna," Science **329**, 930–933 (2010).

[53] A. Christ, S. G. Tikhodeev, N. A. Gippius, and H. Giessen, "Waveguide-plasmon polaritons: Strong coupling of photonic and electronic resonances in a metallic photonic crystal slab," Phys. Rev. Lett. **91**, 183,901–1–4 (2003).

[54] V. I. Belotelov, L. L. Doskolovich, and A. K. Zvezdin, "Extraordinary magneto-optical effects and transmission through metal-dielectric plasmonic systems," Phys. Rev. Lett. **98**, 077,401–1–4 (2007).

[55] G. Mie, "Beiträge zur Optik trüber Medien, speziell kolloidaler Metallösungen," Ann. Phys. **25**, 377–445 (1908).

[56] J. A. Buck, *Fundamentals of optical fibers* (John Wiley & Sons, New Jersey, 2004).

[57] http://www.cst.com.

[58] J. Niegemann, W. Pernice, and K. Busch, "Simulation of optical resonators using DGTD and FDTD," J. Opt. A: Pure Appl. Opt. **11**, 114,015–1–10 (2009).

[59] http://www.jcmwave.com.

[60] http://www.comsol.com.

[61] T. Tamir, H. C. Wang, and A. A. Oliner, "Wave propagation in sinusoidally statified dielectric media," IEEE Trans. Microwave Theory Tech. **12**, 323–335 (1964).

[62] S. G. Tikhodeev, A. L. Yablonskii, E. A. Muljarov, N. A. Gippius, and T. Ishihara, "Quasiguided modes and optical properties of photonic crystal slabs," Phys. Rev. B **66**, 045,102–1–17 (2002).

[63] C. Menzel, C.Rockstuhl, T. Paul, and F. Lederer, "Retrieving effective parameters for quasiplanar chiral metamaterials," Appl. Phys. Lett. **93**, 233,106–1–3 (2008).

[64] C. Rockstuhl, T. Paul, F. Lederer, T. Pertsch, T. Zentgraf, T. P. Meyrath, and H. Giessen, "Transition from thin-film to bulk properties of metamaterials," Phys. Rev. B **77**, 035,126–1–9 (2008).

[65] C. Rockstuhl, T. Zentgraf, T. P. Meyrath, H. Giessen, and F. Lederer, "Resonances in complementary metamaterials and nanoapertures," Opt. Express **16**, 2080–2090 (2008).

[66] N. Liu, L. Langguth, T. Weiss, J. Kästel, M. Fleischhauer, T. Pfau, and H. Giessen, "Plasmonic electromagnetically induced transparency at the Drude damping limit," Nature Materials **8**, 758–762 (2009).

[67] L. H. Shao, M. Ruther, S. Linden, S. Essig, K. Busch, J. Weissmüller, and M. Wegener, "Electrochemical modulation of photonic metamaterials," Advanced Materials **22**, 5173–5177 (2010).

[68] A. Christ, O. J. F. Martin, Y. Ekinci, N. A. Gippius, and S. G. Tikhodeev, "Symmetry breaking in a plasmonic metamaterial at optical wavelength," Nano Letters **8**, 2171–2175 (2008).

[69] L. Li, "Mathematical reflections on the Fourier modal method in grating theory," in *Mathematical modeling in optical science*, G. Bao, L. Cowsar, and W. Masters, eds., Frontiers in Applied Mathematics, chap. 4, pp. 111 – 139 (SIAM, 2001).

[70] D. M. Whittaker and I. S. Culshaw, "Scattering matrix treatment of patterned multilayer photonic structures," Phys. Rev. B **60**, 2610–2618 (1999).

[71] L. Li, "Note on the S-matrix propagation algorithm," J. Opt. Soc. Am. A **20**, 655–660 (2003).

[72] P. Lalanne and G. M. Morris, "Highly improved convergence of the coupled-wave method for TM polarization," J. Opt. Soc. Am. A **13**, 779–784 (1996).

[73] G. Granet and B. Guizal, "Efficient implementation of the coupled-waved method for metallic lamellar gratings in TM polarization," J. Opt. Soc. Am. A **13**, 1019–1023 (1996).

[74] L. Li, "Use of Fourier series in the analysis of discontinuous periodic structures," J. Opt. Soc. Am. A **13**, 1870–1876 (1996).

[75] L. Li, "New formulation of the Fourier modal method for crossed surface-relief gratings," J. Opt. Soc. Am. A **14**, 2758–2767 (1997).

[76] T. Weiss, N. A. Gippius, S. G. Tikhodeev, G. Granet, and H. Giessen, "Efficient calculation of the optical properties of stacked metamaterials with a Fourier modal method," J. Opt. A: Pure Appl. Opt. **11**, 114,019–1–5 (2009).

[77] E. Popov and M. Nevière, "Maxwell equations in Fourier space: Fast-converging formulation for diffraction by arbitrary shaped, periodic, anisotropic media," J. Opt. Soc. Am. A **18**, 2886–2894 (2001).

[78] T. Schuster, J. Ruoff, N. Kerwien, S. Rafler, and W. Osten, "Normal vector method for convergence improvement using the RCWA for crossed gratings," J. Opt. Soc. Am. A **24**, 2880–2890 (2007).

[79] P. Götz, T. Schuster, K. Frenner, S. Rafler, and W. Osten, "Normal vector method for the RCWA with automated vector field generation," Opt. Express **16**, 17,295–17,301 (2008).

[80] R. Antos, "Fourier factorization with complex polarization bases in modeling optics of discontinuous bi-periodic structures," Opt. Express **17**, 7269–7274 (2009).

[81] S. Essig and K. Busch, "Generation of adaptive coordinates and their use in the Fourier modal method," Opt. Express **18**, 23,258–23,274 (2010).

[82] P. Lalanne and E. Silberstein, "Fourier-modal methods applied to waveguide computational problems," Opt. Lett. **25**, 1092–1094 (2000).

[83] J. P. Hugonin and P. Lalanne, "Perfectly matched layers as nonlinear coordinate transforms: A generalized formalization," J. Opt. Soc. Am. A **22**, 1844–1849 (2005).

[84] M. Pisarenco, J. Maubach, I. Setija, and R. Mattheij, "Modified S-matrix algorithm for the aperiodic Fourier modal method in contrast-field formulation," J. Opt. Soc. Am. A **28**, 1364–1371 (2011).

[85] B. Bai and J. Turunen, "Fourier modal method for the analysis of second-harmonic generation in two-dimensionally periodic structures containing anisotropic materials," J. Opt. Soc. Am. B **24**, 1105–1112 (2007).

[86] T. Paul, C. Rockstuhl, and F. Lederer, "A numerical approach for analyzing higher harmonic generation in multilayer nanostructures," J. Opt. Soc. Am. B **27**, 1118–1130 (2010).

[87] B. Bai and L. Li, "Group-theoretic approach to enhancing the Fourier modal method for crossed gratings of plane group p3," Journal of Modern Optics **52**, 1619–1634 (2005).

[88] B. Bai and L. Li, "Group-theoretic approach to the enhancement of the Fourier modal method for crossed gratings: C2 symmetry case," J. Opt. Soc. Am. A **22**, 654–661 (2005).

[89] B. Bai and L. Li, "Group-theoretic approach to enhancing the Fourier modal method for crossed gratings with one or two reflection symmetries," J. Opt. A: Pure Appl. Opt. **7**, 271–278 (2005).

[90] B. Bai and L. Li, "Group-theoretic approach to enhancing the Fourier modal method for crossed gratings with C4 symmetry," J. Opt. A: Pure Appl. Opt. **7**, 783–789 (2005).

[91] B. Bai and L. Li, "Group-theoretic approach to enhancing the Fourier modal method for crossed gratings with hexagonal symmetry," Journal of Modern Optics **53**, 1459–1483 (2006).

[92] J. D. Jackson, *Classical electrodynamics*, 3rd ed. (John Wiley & Sons, 1999).

[93] M. Born and E. Wolf, *Principles of optics*, 7th ed. (Cambridge University Press, Cambridge, 1999).

[94] R. G. Newton, *Scattering theory of waves and particles* (McGraw-Hill, New York, 1966).

[95] G. Chew, *S-matrix theory of strong interaction* (Benjamin, New York, 1961).

[96] A. A. Abrikosov, L. P. Gorkov, and I. E. Dzyaloshinski, *Methods of quantum field theory in statistical physics* (Prentice-Hall, Englewood Cliffs, 1963).

[97] L. Li, "Formulation and comparison of two recursive matrix algorithms for modeling layered diffraction gratings," J. Opt. Soc. Am. A **13**, 1024–1035 (1996).

[98] R. Carminati, J. J. Sáenz, J. J. Greffet, and M. Nieto-Vesperinas, "Reciprocity, unitarity, and time-reversal symmetry of the S matrix of fields containing evanescent components," Phys. Rev. A **62**, 012,712–1–7 (2000).

[99] N. A. Gippius, S. G. Tikhodeev, and T. Ishihara, "Optical properties of photonic crystal slabs with an asymmetrical unit cell," Phys. Rev. B **72**, 45,138–1–7 (2005).

[100] C. Hunte, "The Jones-Mueller transformation," Fizika (Zagreb) **17**, 51–58 (2008).

[101] M. Nevière, E. Popov, and R.Reinisch, "Electromagnetic resonances in linear and nonlinear optics: Phenomenological study of grating behavior through the poles and zeros of the scattering operator," J. Opt. Soc. Am. A **12**, 513–523 (1995).

[102] H. G. Tompkins and E. A. Irene, *Handbook of ellipsometry* (William Andrew Publishing, Norwich, 2005).

[103] A. Kufner and J. Kadlec, *Fourier series*, 1st ed. (Iliffe Books London, 1971).

[104] T. Vallius and M. Honkanen, "Reformulation of the Fourier modal method with adaptive spatial resolution: Application to multilevel profiles," Opt. Express **10**, 24–34 (2002).

[105] L. Fu, H. Schweizer, T. Weiss, and H. Giessen, "Optical properties of metallic meanders," J. Opt. Soc. Am. B **26**, 111–119 (2009).

[106] S. Kim, J. Jin, Y.-J. Kim, I.-Y. Park, Y. Kim, and S.-W. Kim, "High-harmonic generation by resonant plasmon field enhancement," Nature **453**, 757–760 (2008).

[107] E. Popov, M. Nevière, B. Gralak, and G. Tayeb, "Staircase approximation validity for arbitrary-shaped gratings," J. Opt. Soc. Am. A **19**, 33–42 (2002).

[108] J. H. Heinbockel, "Introduction to tensor calculus and continuum mechanics," (1996).

[109] G. J. Pearce, T. D. Hedley, and D. M. Bird, "Adaptive curvilinear coordinates in a plane-wave solution of Maxwell's equations in photonic crystals," Phys. Rev. B **71**, 195,108–1–10 (2005).

[110] F. Gygi, "Electronic-structure calculations in adaptive coordinates," Phys. Rev. B **48**, 11,692–11,700 (1993).

[111] B. Guizal, H. Yala, and D. Felbacq, "Reformulation of the eigenvalue problem in the Fourier modal method with spatial adaptive resolution," Opt. Lett. **34**, 2790–2792 (2009).

[112] H. Yala, B. Guizal, and D. Felbacq, "Fourier modal method with spatial adaptive resolution for structures comprising homogeneous layers," J. Opt. Soc. Am. A **26**, 2567–2570 (2009).

[113] A. Khavasi and K. Mehrany, "Adaptive spatial resolution in fast, efficient, and stable analysis of metallic lamellar gratings at microwave frequencies," IEEE transactions on antennas and propagation **57**, 1115–1121 (2009).

[114] P. G. Etchegoin, E. C. Le Ru, and M. Meyer, "An analytic model for the optical properties of gold," J. Chem. Phys. **125**, 164,705–1–3 (2006).

[115] P. B. Johnson and R. W. Christy, "Optical constants of the noble metals," Phys. Rev. B **6**, 4370–4379 (1972).

[116] B. Gompf, J. Braun, T. Weiss, H. Giessen, M. Dressel, and U. Hübner, "Periodic nanostructures: Spatial dispersion mimics chirality," Phys. Rev. Lett. **106**, 185,501–1–4 (2011).

[117] N. A. Gippius and S. G. Tikhodeev, "Application of the scattering matrix method for calculating the optical properties of metamaterials," Phys.-Usp. **52**, 967–971 (2009).

[118] T. Weiss, "Adaptive spatial resolution and factorization rules in an optical S-matrix approach: Improved convergence for 1D and 2D metallic photonic crystals and metamaterials," Master's thesis, University of Stuttgart (2008).

[119] A. Christ, T. Zentgraf, J. Kuhl, S. G. Tikhodeev, N. A. Gippius, and H. Giessen, "Optical properties of planar metallic photonic crystal structures: Experiment and theory," Phys. Rev. B **70**, 125,113–1–15 (2004).

[120] T. Zentgraf, A. Christ, J. Kuhl, N. A. Gippius, S. G. Tikhodev, D. Nau, and H. Giessen, "Metallodielectric photonic crystal superlattices: Influence of periodic defects on transmission properties," Phys. Rev. B **73**, 115,103–1–9 (2006).

[121] P. Nordlander, C. Oubre, E. Prodan, K. Li, and M. I. Stockman, "Plasmon hybridization in nanoparticle dimers," Nano Letters **4**, 899–903 (2004).

[122] D. E. Gómez, K. C. Vernon, and T. J. Davis, "Symmetry effects on the optical coupling between plasmonic nanoparticles with applications to hierarchical structures," Phys. Rev. B **81**, 075,414–1–10 (2010).

[123] J. Petschulat, C. Menzel, A. Chipouline, C. Rockstuhl, A. Tünnermann, F. Lederer, and T. Pertsch, "Multipole approach to metamaterials," Phys. Rev. A **78**, 043,811–1–9 (2008).

[124] L. Landau and E. M. Lifshitz, *Quantum mechanics. Non-relativistic theory* (Pergamon, 1966).

[125] E. Centeno and D. Felbacq, "Optical bistability in finite-size nonlinear bidimensional photonic crystals doped by a microcavity," Phys. Rev. B **62**, R7683–R7686 (2000).

[126] A. Khavasi, A. K. Jahromi, and K. Mehrany, "Longitudinal Legendre polynomial expansion of electromagnetic fields for analysis of arbitrary-shaped gratings," J. Opt. Soc. Am. A **25**, 1564–1573 (2008).

Curriculum vitae Thomas Weiss

Since October 2008

Ph. D. student in Stuttgart (Germany) and Clermont-Ferrand (France).

Topic: "Advanced numerical and semi-analytical scattering matrix calculations for modern nano-optics."

25$^{\text{th}}$ September 2008

Diploma of physics with overall grade "sehr gut" (excellent).

2007 to 2008

Diploma thesis:

"Adaptive spatial resolution and factorization rules in an optical S-matrix approach: Improved convergence for 1D and 2D metallic photonic crystals and metamaterials."

Grade: "sehr gut" (excellent)

2002 to 2007

Study at University of Stuttgart:

- Main diploma exams in 2007, overall grade "sehr gut" (excellent). Elective subjects: Astrophysics and semiconductor physics.
- Internship at 4$^{\text{th}}$ Physics Institute in 2007. Topic: "Simulation of nonlinear pulse propagation in optical fibers by the split-step Fourier method."
- Pre-diploma in physics in 2005, overall grade "sehr gut" (excellent).

2000 to 2002

Practical and social years in Kulmbach and Bayreuth (Germany).

1987 to 2000

- Secondary school: Caspar Vischer Gymnasium in Kulmbach, overall grade: 1.7 (good).
- Primary school: Max-Hundt-Schule Kulmbach and Volksschule Gößmannsreuth.

27$^{\text{th}}$ April 1981

Date of birth; birthplace Amberg, Germany.

Acknowledgment

At this place, I would like to thank all the people who supported this work directly or indirectly.

I am particularly grateful to my advisors, Prof. Dr. Harald Giessen, Prof. Dr. Gérard Granet, and Prof. Dr. Nikolay. A. Gippius for their helpful advice and the fruitful discussions. They have made it also possible for me to carry out my Ph. D. in a so-called cotutelle between the 4th Physics Institute in Stuttgart, Germany, and the LASMEA in Clermont-Ferrand, France.

In addition, I would like to mention that I appreciated the hours of scientific and private discussions with colleagues from all over the world. Especially, I enjoyed the scientific exchange with Prof. Dr. Sergei G. Tikhodeev and his student M. Sc. Sergey V. Lobanov from Moscow, Russia, as well as Prof. Dr. Lifeng Li from Beijing, China. Moreover, I acknowledge that Prof. Tikhodeev and Prof. Li have agreed to approve my thesis for the cotutelle. I appreciated their thorough reading of my thesis and the helpful comments.

Furthermore, special thanks to my wife Christiane Reinert-Weiss, my brother Andreas Weiss, my sister Stephanie Weiss, and my colleague Rémi Polles, who proofread my thesis. I also want to thank Dipl. Phys. Martin Schäferling from the 4th Physics Institute in Stuttgart, who helped me to debug my code.

Among my other colleagues, I would like to mention the support from Dipl. Phys Mario Hentschel, who fabricated and measured the structures discussed in chapters 2 and 3. I am also very grateful to Dr. Na Liu, who provided me with the possibility to advertise the methods of adaptive spatial resolution and matched coordinates in many publications. Thank you also to Dipl. Phys. Martin Mesch for supporting me with respect to the network connections, making it possible for me to access the powerful computers in Stuttgart from Clermont-Ferrand and all over the world. In this context, special thanks to the secretary of the 4th Physics Institute – Dr. Christine von Rekowski – who managed all my travel expenses and fundings for my frequent journeys between Clermont-Ferrand and Stuttgart.

Additionally, I would like to thank Dr. Julia Braun, Dr. Bruno Gompf, and Prof. Dr. Martin Dressel from the 1st Physics Institute of the University of Stuttgart for the collaboration on ellipsometry measurements and Mueller matrix calculations.

I acknowledge also the support from BMBF (13N 9155, 13N 10146), DFG (FOR 557, FOR 730, GI 269/11-1), and DFH/UFA.

Finally, thanks to all the people who supported my work indirectly, such as my parents, my grandparents, and all my colleagues from the 4th Physics Institute in Stuttgart and the LASMEA in Clermont-Ferrand.